A Complementary Study of Perovskites: Combining Diffraction, Solid-State NMR and First-Principles DFT Calculations

University
of
St Andrews

A thesis presented for the degree of

Doctor of Philosophy

in the Faculty of Science of the University of St Andrews

by Karen Elizabeth Johnston, BSc (Hons), AMRSC

July 2010

Declaration

I, Karen Elizabeth Johnston, herby certify that this thesis, which is approximately 63,000 words in length, has been written by me, that it is the record of work carried out by me and that it has not been submitted in any previous application for a higher degree.

I was submitted as a research student in September, 2006 and as a candidate for the degree of PhD in September, 2007; the higher study for which this is a record was carried out in the University of St Andrews between 2006 and 2010.

Date ……………… Signature of Candidate ………………………………

I hereby certify that the candidate has fulfilled the conditions of the Resolution and Regulations appropriate for the degree of PhD in the University of St Andrews and that the candidate is qualified to submit this thesis in application for that degree.

Date ……………… Signature of Supervisor ………………………………

Signature of Supervisor ………………………………

In submitting this thesis to the University of St Andrews I understand that I am giving permission for it to be made available for use in accordance with the regulations of the University Library for the time being in force, subject to any copyright vested in the work not being affected thereby. I also understand that the title and the abstract will be published, and that a copy of the work may be made and supplied to any bona fide library or research worker, that my thesis will be electronically accessible for personal or research use unless exempt by award of an embargo as requested below, and that the library has the right to migrate my thesis into new electronic forms as required to ensure continued access to the thesis. I have obtained any third-party copyright permissions that may be required in order to allow such access and migration, or have requested the appropriate embargo below.

The following is an agreed request by candidate and supervisor regarding the electronic publication of this thesis:

Embargo on both printed copy and electronic copy for the same fixed period of two years on the following ground: publication would preclude future publication.

Date ……………… Signature of Candidate ………………………………

Signature of Supervisor …………………………………….

Signature of Supervisor …………………………………….

Abstract

Perovskites, ABX_3, and their associated solid-solutions are a particularly important and attractive area of research within materials chemistry. Owing to their structural and compositional flexibility and potential physical properties they are one of the largest classes of materials currently under investigation. This thesis is concerned with the synthesis and structural characterisation of several perovskite-based materials using a combined approach of high-resolution synchrotron X-ray and neutron powder diffraction (NPD), solid-state Nuclear Magnetic Resonance (NMR) and first-principles Density Functional Theory (DFT) calculations.

Initial investigations concentrated on room temperature $NaNbO_3$, a perovskite widely debated in the literatue. Published crystallographic data indicate $NaNbO_3$ possesses two crystallographically distinct Na sites in space group Pbcm. Whilst some of our materials appear in agreement with this (notably a commercially purchased sample) many of our laboratory-synthesised samples of $NaNbO_3$ routinely comprise of two phases, which we show to be the antiferroelectric Pbcm and polar $P2_1ma$ polymorphs. Several different synthetic methods were utilised during this investigation and the quantity of each phase present was found to vary as a function of preparative method. ^{23}Na, ^{93}Nb and ^{17}O DFT calculations were used in conjunction with experiment to aid in spectral analysis, assignment and interpretation. In addition, *ab initio* random structure searching (AIRSS) was utilised in an attempt to predict the most stable phases of $NaNbO_3$. This proved to be both successful and highly informative.

A series of $NaNbO_3$-related solid-solutions, namely $K_xNa_{1-x}NbO_3$ (KNN), $Li_xNa_{1-x}NbO_3$ (LNN) and $Na_{1-x}Sr_{x/2}\square_{x/2}NbO_3$ (SNN) have also been synthesised and characterised. The substitution of K^+, Li^+ and Sr^{2+} cations onto the A site appears to produce the same polar $P2_1ma$ phase initially identified in the room temperature $NaNbO_3$ investigation. The abrupt change in cation size in the KNN and LNN series, and the introduction of vacancies in the SNN series, is thought to result in a structural distortion which, in turn, causes the formation of the $P2_1ma$ phase.

A low temperature synchrotron X-ray powder diffraction study ($12 < T < 295$ K) was completed for a sample of $NaNbO_3$ composed of the $P2_1ma$ polymorph (~90%) and a small quantity of the Pbcm phase (~10%). A region of phase coexistence was identified between the $P2_1ma$, R3c and Pbcm phases over a relatively large temperature range. Full conversion of the $P2_1ma$ phase to the low temperature R3c phase was not possible and, consistently, the $P2_1ma$ phase was the most abundant phase present. Factors such as structural, strain, crystallite size and morphology are thought to be crucial in determining the exact phases of $NaNbO_3$ produced, both at low and room temperature.

The solid-solution $La_{1-x}Y_xScO_3$ was also investigated. Compositions x = 0, 0.2, 0.4, 0.6, 0.8 and 1 were successfully synthesised and characterised. Refined high-resolution NPD data indicates that an orthorhombic structure, in space group Pbnm, was retained throughout the solid-solution. Using ^{45}Sc and ^{89}Y MAS NMR each sample was found to exhibit disorder, believed to result from both a distribution of quadrupole and chemical shifts. NMR parameters were calculated for several model Sc and Y compounds using DFT methods to determine the feasibility and accuracy of ^{45}Sc and ^{89}Y DFT calculations. These proved successful and subsequent calculations were completed for the end members $LaScO_3$ and $YScO_3$. DFT calculations were also utilised to gain insight into the disorder exhibited in the $La_{1-x}Y_xScO_3$ solid-solution.

Acknowledgements

Firstly, and most importantly, I would like to thank my supervisors, Professor Philip Lightfoot and Dr Sharon Ashbrook, for giving me the opportunity to complete this research. To Phil, thank you for the many interesting and thought-provoking discussions over the last few years! To Sharon, thank you for being not only an excellent supervisor but also a friend and mentor. Your constant support, guidance and enthusiasm towards this research has been a significant factor towards the overall success of this project.

Much of the work completed within this thesis would not have been possible without the excellent assistance and guidance of various beamline scientists and facility managers. Special thanks to Professor Kevin Knight at HRPD for experimental assistance and useful discussion regarding the work completed on $NaNbO_3$. Many thanks also to Dr Ron Smith at POLARIS, Dr Chiu Tang, Dr Julia Parker and Dr Alistair Lennie at beamline I11, Diamond and Dr Dinu Igua at the 850 MHz Solid-State NMR Facility, Warwick. A special thank you to Professor Stephen Wimperis at the University of Glasgow for use of his spectrometer. Thank you to Dr Herbert Fruchtl, Dr Manfred Buck and Mr Ross Blackley for computational and experimental assistance at the University of St Andrews.

Several areas of this research were completed in collaboration with external researchers. Therefore, I would like to thank Professor Chris Pickard and Dr Maria Baias for their structure searching work using AIRSS. I would also like to thank Professor Clare Grey and Dr Frédéric Blanc for their experimental assistance with isotopic enrichment of several of our samples. Each of their contributions to this project are greatly appreciated. I would also like to thank Pierre-Yves Calvez and Charlotte Cree for their contributions to this work.

Many thanks go to both the past and present Lightfoot and Ashbrook group members for making each day in the lab more enjoyable; in particular to Dr John Griffin for his excellent experimental advice and constant supply of funny moments, to Dr Thushitha Mahenthirarajah, Alexandra Gibbs and Sandra Reisinger thank you for experimental assistance during data collection and, most importantly, the supply of gingerbread men during the writing of this thesis, to Martin Mitchell and Stephanie Moore thank you for the many entertaining moments that have kept me going over the last few months! Very special thanks to Dr Dave Aldous for his invaluable help and advice in all things solid-state over the last five years. I would also like to thank my friends both in and out of the chemistry department, in particular Emma Whitelaw, Jason Gillespie and Andy Young for their support.

An unreserved thank you goes to my parents, Robert and Hilda. You have supported me through the many high and low points over the last few years and for that I am indebted to you both. Thank you for your constant belief and encouragement. To my sister Pamela, thank you for keeping 'morale' high and bringing a smile to my face even through the toughest of times. Finally, to Charlie, your constant encouragement has helped to keep me going during the most difficult stages of this work. Thank you for the many happy and funny moments we have shared over the last few years!

Contents

2 Experimental Techniques

5 A Low Temperature s-PXRD Study of $NaNbO_3$ 295

6 The Synthesis and Characterisation of $La_{1-x}Y_xScO_3$ 325

Appendices (see attached CD)

I

II

III

IV

V

List of Symbols and Abbreviations

□	Vacancy
2θ	Angle between X-ray source and detector
Å	Angstrom, 1×10^{-10} m
B_0	Magnetic field strength
B_1	Strength of applied pulse
B_0^{eff}	Effective static magnetic field
C_Q	Quadrupolar coupling constant
d	Parameter describing the distortion of the octahedra in a rhombohedral perovskite
d_{hkl}	Interplanar d-spacing
eV	Electron volts
E_C	Coercive field
E_{cut}	Cut-off energy
f	Scattering factor or form factor of an atom
f.u.	Formula units
$\hat{H}$	Hamiltonian
$\mathbf{I}$	Intrinsic spin angular momentum
I	Spin quantum number
J	Isotropic J-coupling or scalar coupling
m_I	Magnetic spin quantum number
$\mathbf{M_0}$	Bulk magnetization vector
M	Metal cation
n_A	Number of electrons in the outer electron shells of the A atom
N_A	Principal quantum number of the A atom
ppm	Parts per million
P	Polarisation
P_R	Remnant polarisation
P_S	Saturation polarisation
P_Q	Quadrupolar product
r	Ionic radius
r_C	Core radius

R_p	R-profile
Ry	Rygbergs
s	Orthorhombic strain
sc	Parameter describing the displacement of the A-site cation from its ideal position
S_y	Structural refinement residual
t	Goldschmidt tolerance factor
tc	Parameter describing the displacement of the B-site cation from its ideal position
T_1	Longitudinal or spin-lattice relaxation
T_2	Transverse of spin-spin relaxation
T_C	Curie temperature
$\mathbf{V}$	EFG tensor
wR_p	R-weighted profile
y_{oi}	Observed intensity
y_{ci}	Calculated intensity
γ	Gyromagnetic ratio
δ	Deshielding parameter
δ_{iso}	Isotropic chemical shift
δ_Q	Isotropic quadrupolar shift
$\Delta\alpha$	Difference in polarisabilities of the B and B′ cations
$\Delta\sigma_{cs}$	Shielding anisotropy
$\Delta\nu_{1/2}$	Difference in linewidth
$d^{1}_{mm'}(\alpha)$	Wigner induced rotation matrix element
η_{CS}	Asymmetry parameter of the shielding interaction
η_Q	Asymmetry parameter of the quadrupolar interaction
λ	Wavelength
$\boldsymbol{\sigma}$	Shielding second-rank tensor
σ	Stress
σ_{iso}	Isotropic shielding
$\sigma(t)$	Density operator
$\sigma_{i,j}(t)$	Elements of the density matrix
χ^2	Parameter measuring the goodness of fit

$\Psi(t)$	Wavefunction
ω	Oxygen octahedral rotation angle
ω_0	Larmor frequency (in rad s^{-1})
ω_D^{PAS}	Dipolar splitting parameter in the PAS
ω_Q^{PAS}	Quadrupolar splitting parameter in the PAS
Ω	Offset frequency
ABX_3	General formula for a ternary perovskite where A is the larger cation occupying the 12-coordinate site, B is the smaller cation occupying the 6-fold coordinate site and X is the anion, commonly oxygen
$A_2BB'X_6$	General formula for a double perovskite where B and B′ are the 6-fold coordinate site
$A_3B_2B'X_{12}$	General formula for a 2:1 ordered perovskite
$A_4B_3B'X_{12}$	General formula for 3:1 ordered perovskite
AIRSS	*Ab Initio* Random Structure Searching
$[A_{n-1}BnO_{3n+1}]^{2-}$	General formula for Aurivillius phases
$A'[A_{n-1}B_nO_{3n+1}]$	General formula for Dion-Jacobson phases
APS	Argonne Advanced Photon Source
CMR	Colossal magnetoresistance
CSA	Chemical Shift Anisotropy
CW	Continous wave
$dist_{CS}$	Distribution of chemical shift environments
$dist_Q$	Distribution of quadrupolar contributions
DAS	Dynamic-Angle Spinning
DFT	Density Functionl Theory
DOR	Double rotation
EDX	Energy Dispersive X-ray Spectroscopy
EFG	Electric Field Gradient
ESRF	European Synchrotron Radiation Faciltity
FAM	Fast Amplitude Modulation
FID	Free Induction Decay
FT	Fourier transform
GIPAW	Gauge-Including Projector Augmented Wave

GGA	General Gradient Approximation
GSAS	General Structure Analysis System
hkl	Miller indices
HRPD	High Resolution Powder Diffractometer
ICSD	Inorganic Crystal Structure Database
ILL	Institute Laue-Langevin
KNN	Potassium sodium niobate ($K_xNa_{1-x}NbO_3$)
l-PXRD	Laboratory Powder X-ray Diffraction
LDA	Local Density Approximation
LNN	Lithium sodium niobate ($Li_xNa_{1-x}NbO_3$)
$M_2[A_{n-1}B_nO_{3n+1}]$	General formual for Ruddlesden-Popper phases
MACs	Multi-analysing crystal detectors
MAS	Magic-Angle Spinning
MPB	Morphotropic Phase Boundary
MQMAS	Multiple-Quantum Magic-Angle Spinning
NLO	Nonlinear optic
NMR	Nuclear Magnetic Resonance
NPD	Neutron Powder Diffraction
PAS	Principle Axis System
PAW	Projector Augmented Wave
PBE	Perdew-Burke-Ernzerhof
PFM	Piezoelectric Force Microscopy
POTATO	Program Originated To Analyse Tilted Octahedra
PZT	Lead zirconium titanate
rf	Radiofrequency radiation
s-PXRD	Synchrotron Powder X-ray Diffraction
SEM	Scanning Electron Microscopy
SHG	Second Harmonic Generation
SNN	Strontium sodium niobate ($Na_{1-x}Sr_{x/2}\square_{x/2}NbO_3$)
SOLA	Solids Line Shapes Analysis program
SPAM	Soft Pulse Added Mixing
SSZ	Scandia-stabilised zirconia
TEM	Transmission Electron Microscopy
TOF	Time-of-Flight

TPPM	Two Pulse Phase Modulation decoupling
TTB	Tetragonal Tungsten Bronze
XRD	X-ray diffraction

Publications

K. E. Johnston, C. C. Tang, J. E. Parker, K. S. Knight, P. Lightfoot and S. E. Ashbrook, *J. Am. Chem. Soc.*, 2010, **132**, 8732.

S. W. Reader, M. R. Mitchell, K. E. Johnston, C. J. Pickard, K. R. Whittle and S. E. Ashbrook, *J. Phys. Chem. C*, 2009, **113**, 18874.

P. S. Berdonosov, D. O. Charkin, K. S. Knight, K. E. Johnston, R. J. Goff, V. A. Dolgikh and P. Lightfoot, *J. Solid State Chem.*, 2006, **179**, 3437.

Chapter 1

Background and Introduction

1.1 Perovskites

Perovskite, $CaTiO_3$, was initially discovered in the Ural Mountains of Russia by Gustav Rose in 1839 and named after the Russian mineralogist L. A. Perovski (1792 – 1865).[1] Since its discovery the name perovskite has been utilised to describe hundreds of materials with stoichiometry ABX_3. Perovskites are three-dimensional framework structures, constructed of corner-sharing BX_6 octahedra. The A-site cation, conventionally the larger of the two metal ions, is commonly either a rare earth or alkali earth metal. The smaller B-site cation, typically a transition metal, is surrounded by the anions X, usually O^{2-}, forming BO_6 octahedra. 'Ideal' perovskite is cubic, as shown in Figure 1.1. The A-site cations (green) are located on each corner of the cube, whilst the B-site cations (blue) are placed in the centre of the cube with the anions (red) positioned at the centre of each of the cube faces. Ideal coordination geometries for the A- and B-site cations are 12 and 6 fold respectively. A cubic close packed array is conventionally formed between the A-site cations and anions, whilst the B-site cation is positioned in 1/4 of the octahedral holes formed between the two. The size of A is vital in enabling such a close packed arrangement to occur.

1.2 Perovskite Distortions

In reality, compounds adopting the perovskite structure are often of lower symmetry owing to distortion or, more commonly, tilting of the octahedra. As a direct consequence there are considerably more distorted perovskites known than there are cubic.[2] Octahedral tilting is considered an intrinsic property of perovkites and is a direct consequence of the relative sizes and charge of both the A- and B-site cations situated within the structure. The mechanism and degree of such tilting plays a

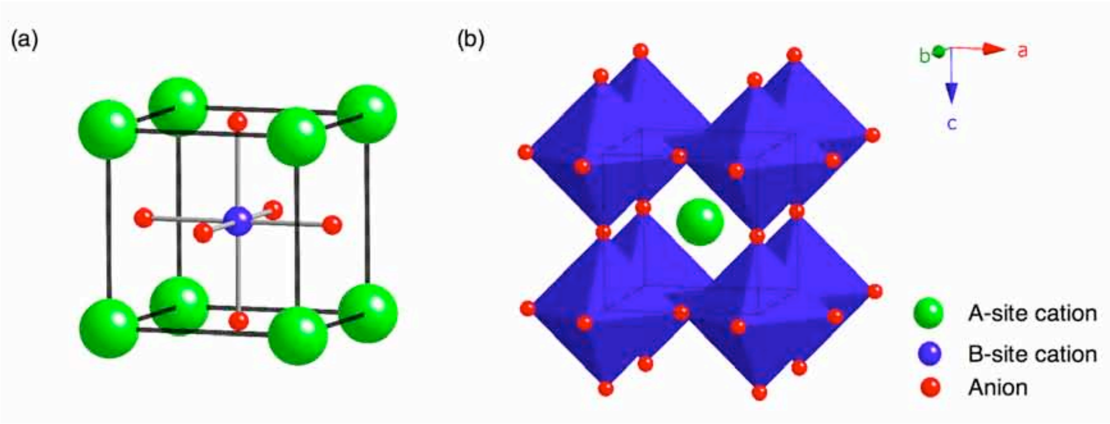

Figure 1.1: Cubic perovskite, $CaTiO_3$, with the origin centred on (a) the B-site cation and (b) the A-site cation.

significant role in the symmetry adopted by a structure. The level of distortion or strain imposed upon a structure is commonly measured using a parameter known as the tolerance factor, t, first introduced by Goldschmidt,[3]

$$t = \frac{r_A + r_X}{\sqrt{2}(r_B + r_X)}, \tag{1.1}$$

where r_A, r_B and r_X are the ionic radii of A, B and X respectively.[4,5] When t is close to unity the degree of distortion observed is low. Large deviations from unity however result in increasing levels of strain upon the perovskite structure, commonly imposed by inappropriately sized ions for their allocated site, i.e., either too large or too small. In order to relieve such strain from the structure the BX_6 octahedra undergo some degree of rotation, accompanied by a corresponding shift of the A-site cation. When $0.85 < t < 1.06$ a perovskite structure, or suitably distorted version, will be adopted. In addition, when using the Shannon and Prewitt radii[K5] for $0.9 < t < 1.0$ the structure is often cubic and therefore more like an ideal structure. Values outside this range indicate the perovskite structure cannot meet the coordination requirements of the two chosen cations, hence a different structural arrangement is required. This is often the case when A and B cations of similar size are used.

The perovskite structure is routinely modified, either by cation displacements, tilting or distortion of the octahedra or, more commonly, a

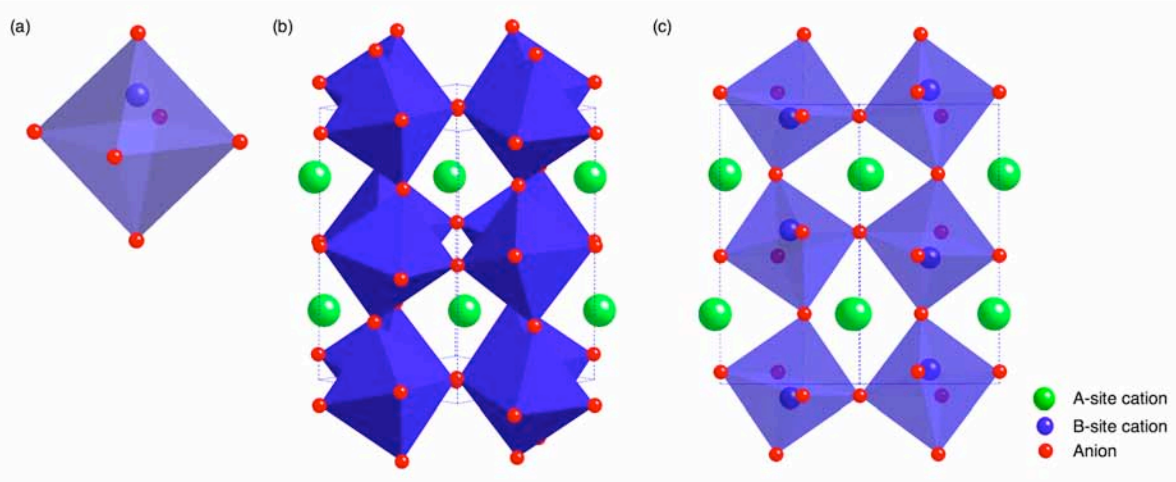

Figure 1.2: (a) A schematic representation of an exaggerated B-site cation displacement, (b) an example of octahderal tilting in perovskites and (c) a perovskite exhibiting both a B-site cation displacement and octahedral tilting.

combination of the two, as illustrated in Figure 1.2. Cation displacements are small shifts of the A- and/or B-site cations from their ideal positions. B site displacements are more common and are often directly related to the physical properties exhibited by a material, for example the ferroelectric displacement of the Ti^{4+} cation in $BaTiO_3$.[6,7] A schematic representation of an exaggerated B-site cation displacement is shown in Figure 1.2(a). Such displacements commonly give rise only to very slight distortions of the octahedra, hence they are relatively simple to deal with and have very little effect on the lattice parameters of a structure. Tilting of the octahedra (Figure 1.2(b)) have a considerably greater effect on the lattice parameters and are, in effect, more difficult to accurately describe. Numerous papers within the literature have attempted to depict methods for describing and illustrating how the various tilting mechanisms operate and, in turn, how they may be classified. Extensive work has been completed in this area by Megaw,[8] Darlington,[8] O'Keeffe and Hyde,[9] Thomas,[10-12] Zhou and Goodenough,[13] Howard and Stokes.[14,15] To date, however, Glazer[16] has provided the most exhaustive and comprehensive study of octahedral tilting mechanisms and, in turn, developed an accurate and detailed notation for describing the most commonly encountered tilts. The notation established by Glazer is by far the most influential and has, in turn, become the standard notation adopted within

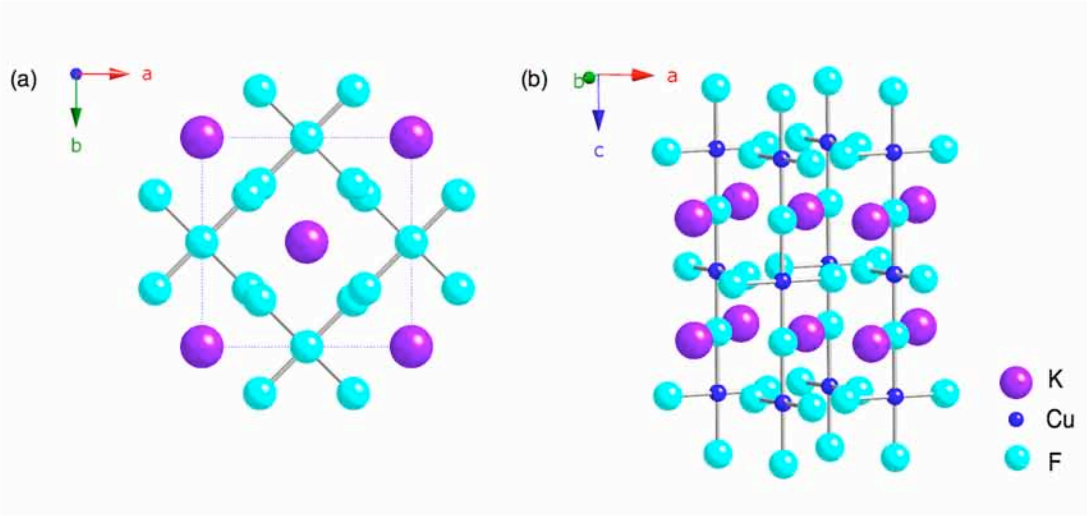

Figure 1.3: The crystal structure of $KCuF_3$ viewed (a) along c and (b) across the ab plane.

the perovskite literature. Octahedral distortions are commonly caused by electronic instabilities of the enclosed metal ion.[17] In particular, perovskites containing Jahn-Teller ions such as Cu^{2+} and Mn^{3+} routinely exhibit cooperative Jahn-Teller distortions, for example $KCuF_3$[17] shown in Figure 1.3. As a result they also commonly display many interesting physical properties such as charge and spin ordering.[18]

1.3 Glazer Notation

Octahedral tilting is commonly observed when the A-site cation is too small to fully occupy the 12 coordinate site. Under such circumstances the BO_6 octahedra are forced to tilt or rotate in order to accommodate its size. An associated effect of such tilting is greater flexibility in the coordination of the A-site cation (8 – 12) whilst leaving the B site environment essentially unchanged. Glazer[16] recognised that cooperative rotations give rise to as many as 23 different tilting mechanisms. The work presented within his original paper concentrated solely on the tilting systems adopted, with no discussion regarding cation displacements and/or octahedral distortions. The tilting mechanism adopted within a structure is extremely important as the overall symmetry follows that of the tilts.

Table 1.1: Glazer notation and initial space group allocation by Glazer. The two possible space group ambiguities, for tilts $a^+a^+c^-$ and $a^+a^+a^-$, are denoted by *.

	Tilt System Number	Tilt System Symbol	Space Group
Three-tilt systems	1	$a^+b^+c^+$	Immm
	2	$a^+b^+b^+$	Immm
	3	$a^+a^+a^+$	$Im\bar{3}$
	4	$a^+b^+c^-$	Pmmn*
	5	$a^+a^+c^-$	Pmmn
	6	$a^+b^+b^-$	Pmmn
	7	$a^+a^+a^-$	Pmmn*
	8	$a^+b^-c^-$	$A2_1/m11$
	9	$a^+a^-c^-$	$A2_1/m11$
	10	$a^+b^-b^-$	Pnma
	11	$a^+a^-a^-$	Pnma
	12	$a^-b^-c^-$	$F\bar{1}$
	13	$a^-b^-b^-$	I2/a
	14	$a^-a^-a^-$	$R\bar{3}c$
Two-tilt systems	15	$a^0b^+c^+$	Immm
	16	$a^0b^+b^+$	I4/m
	17	$a^0b^+c^-$	Bmmb
	18	$a^0b^+b^-$	Bmmb
	19	$a^0b^-c^-$	F2/m11
	20	$a^0b^-b^-$	Imcm
One-tilt systems	21	$a^0a^0c^+$	C4/mmb
	22	$a^0a^0c^-$	F4/mmc
Zero-tilt systems	23	$a^0a^0a^0$	$Pm\bar{3}m$

Fundamentally Glazer's work was based on the sole assumption that octahedra are rigid and regular and, when tilted, they produce a considerable effect on neighbouring octahedra. Glazer realised the complexity in trying to visualise and describe the effects on successive octahedra and therefore his initial work concentrated on understanding feasible tilting modes for individual octahedra. Glazer's notation provides an accurate and effective method for comparing the various tilts exhibited by different structures. The notation, $a^{\pm}b^{\pm}c^{\pm}$, describes a tilting mechanism by specifying rotations of the octahedra about the three Cartesian axes. Each rotation is described by two parameters, a letter and a superscript. The letter indicates the magnitude of the rotation about that axis relative to the magnitude of all other rotations about the other Cartesian axes whilst the superscript denotes whether rotations in adjacent layers are in or out-of-phase. A positive superscript indicates adjacent octahedra tilt in the same direction, negative values indicate they rotate in opposite directions. Repetition of a letter represents equal tilts along different rotation axes. A simple example is 'ideal' perovskite (cubic) in which no tilts are observed, resulting in the notation $a^0a^0a^0$. The tilt $a^+b^-b^-$ indicates the rotation about the x axis to be different to that about the y and z axes. Similarly, the superscript indicates that rotations of two neighbouring octahedra along the x axis are in the same direction, whilst neighbouring octahedra along the y and z axes rotate in opposite directions. All 23 Glazer systems are listed in Table 1.1 and classified according to the number of tilts exhibited.

In addition to the notation Glazer also assigned space groups (see Chapter 2, section 2.1.2) to each tilt system identified. All space group allocations can also be found in Table 1.1. Interestingly, however, in recent years it has been suggested that Glazer was incorrect in his initial space group assignment for certain tilt systems, in particular $a^+a^+c^-$ and $a^+a^+a^-$.[19] Leinenweber and Parise completed an extensive structural investigation for the perovskite $CaFeTi_2O_6$ and within this study they concluded that the tilt exhibited, $a^+a^+c^-$, was incorrectly assigned by Glazer to space group Pmmn. Their findings suggested space group $P4_2/nmc$ to be a more accurate description of the observed tilt.

The two one-tilt systems $a^0a^0c^+$ and $a^0a^0c^-$ are shown in Figures 1.4(a) and (b) respectively. When two neighbouring octahedra rotate in the same direction they are in-phase with one another resulting in the tilt $a^0a^0c^+$ (Figure 1.4(a)). If, however, the two rotate in opposite directions they become out-of-phase, resulting in the tilt illustrated in Figure 1.4(b). When viewed along the c-axis these simple one-tilt systems provide a

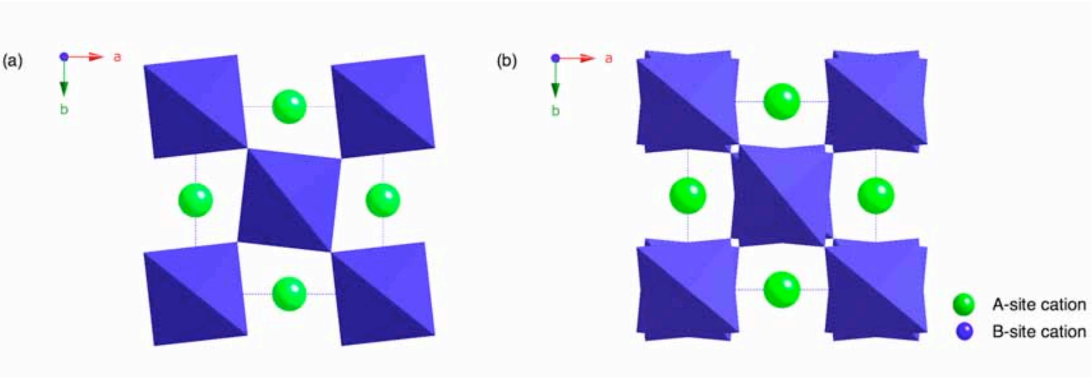

Figure 1.4: Examples of the one-tilt Glazer systems (a) $a^0a^0a^+$ and (b) $a^0a^0c^-$.

convenient way of visualising Glazer notation. In reality, however, systems routinely adopt more than one tilt hence visualisation becomes increasingly difficult. The most commonly encountered tilt system is $a^-a^-b^+$, displaying three different tilts resulting in an orthorhombic distortion, commonly associated with $GdFeO_3$ (Figure 1.5). Interestingly, this mechanism is also adopted by naturally occurring perovskite, $CaTiO_3$, thereby making it orthorhombic as opposed to the ideal 'cubic' structure.

By careful consideration of the interatomic distances between the octahedra centres Glazer's work extended to include a relation between the tilting mechanism observed and the symmetry adopted within a particular system, details of which can be found in his original publication.[16] Unfortunately, Glazer did not expand this information into detailed structural models complete with atomic coordinates for each of the systems described. In 1997 Woodward[20,21] completed an extensive review of Glazer's work and attempted to translate his original classifications into complete structural models by developing a FORTRAN program known as POTATO (Program Originated To Analyse Tilted Octahedra). Using the Glazer symbol, rotation angle about each of the Cartesian axes and the metal to oxygen bond lengths as input POTATO was capable of outputting a unit cell description of the compound, complete with atomic coordinates. This was successfully undertaken for many of the tilt systems originally proposed by Glazer.

Woodward's investigation did, however, highlight several areas of discrepancy. Using POTATO, six tilt systems posed considerable problems when calculating appropriate space groups and structural

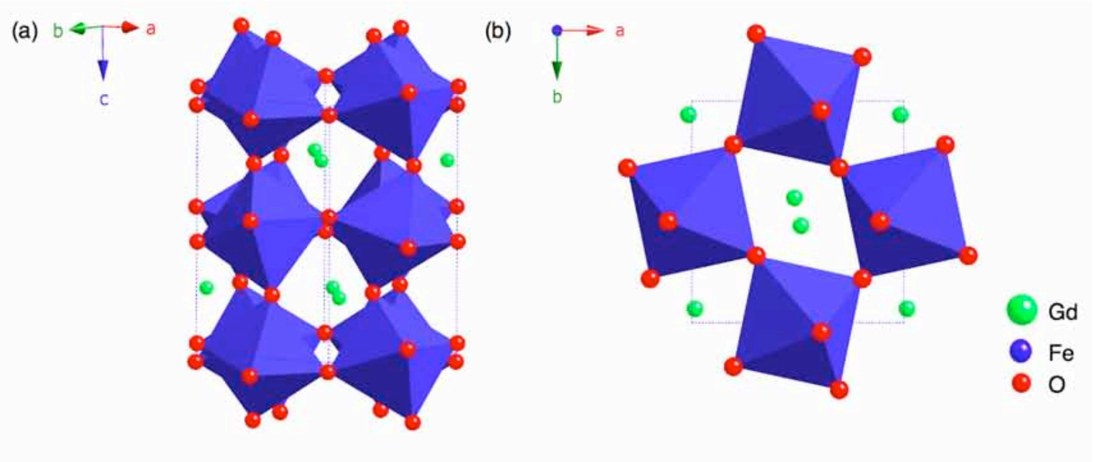

Figure 1.5: The crystal structure of $GdFeO_3$ displaying the most commonly encountered Glazer tilt, $a^-a^-b^+$, as viewed (a) across the ab plane and (b) down the c axis.

models, namely $a^+b^+c^-$, $a^+a^+c^-$, $a^+b^+b^-$, $a^+a^+a^-$, $a^0b^+c^-$ and $a^0b^+b^-$. Interestingly, the two tilts reported in the literature as being wrongly assigned by Glazer were amongst these six. Woodward suggested such discrepancies existed owing to octahedral distortions being an inherent geometric property of tilt systems and that slight distortions of the octahedra were always necessary to retain the overall connectivity of the octahedra. In turn for such structures it is extremely challenging to uniquely define a space group as the symmetry adopted by the unit cell depends upon the initial distortion of the octahedra. Woodward therefore concluded that it was not possible to rigorously assign space groups for the six problematic crystal systems and, in reality, compounds adopting such tilting mechanisms would favour the most symmetric configuration and space group. Therefore, the original space group assignment by Glazer for the tilts $a^+a^+c^-$ and $a^+a^+a^-$ was not necessarily incorrect, but rather extremely difficult to accurately and precisely assign.

1.4 Cation Substitutions

Since the discovery of $BaTiO_3$, perovskites have been a subject of significant interest and are studied extensively for their interesting and useful physical properties. They are currently one of the most heavily researched fields within solid-state chemistry.

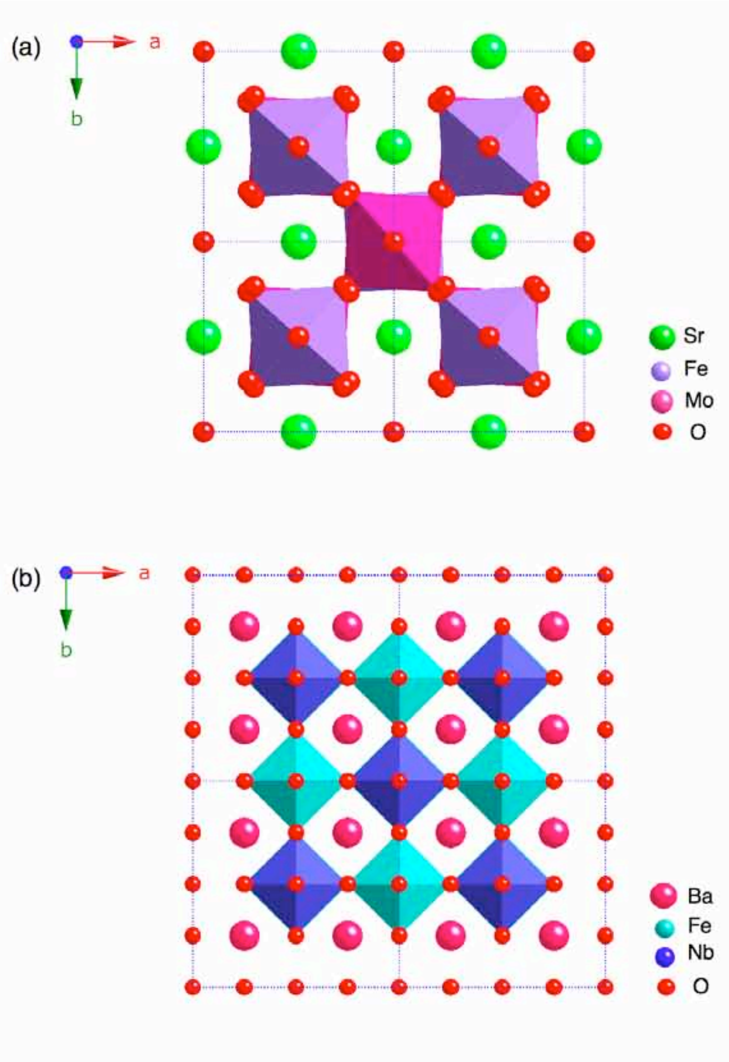

Figure 1.6: Two examples of double perovskites, $A_2BB'X_6$. In (a) Sr_2FeMoO_6 and (b) Ba_2FeNbO_6.

Perovskites are renowned for their compositional flexibility and ease of distortion, and hence the perovskite family is routinely extended by cation substitutions at either the A or B sites, leading to the formation of many useful solid-solutions; $A_{1-x}A'_xBX_3$ and $AB_{1-x}B'_xX_3$. When x = 0.5 perovskites of this nature are generally written as $AA'B_2X_6$ and $A_2BB'X_6$, commonly known as double or double-edge perovskites, two examples of which, namely Sr_2FeMoO_6 and Ba_2FeNbO_6, are shown in Figures 1.6(a) and (b) respectively.[22,23] By careful consideration of parameters such as the tolerance factor it is often possible to 'tune' solid-solutions to exhibit very specific physical properties such as ferroelectricity, piezoelectricity, superconductivity and ionic conductivity. Solid-solutions routinely undergo interesting first- or second-order phase transitions with corresponding shifts in lattice parameters and cation displacements. In some cases dramatic structural changes may occur resulting in a Morphotropic Phase Boundary (MPB). The term MPB, initially used by Jaffe *et al.*,[24] to described a phase boundary in lead zirconium titanate (PZT) (x = 0.48) where an abrupt change from rhombohedral to tetragonal symmetry was observed over an extremely small compositional range. This term is now routinely utilised to describe systems exhibiting similar behaviour. For example, exceptional piezoelectric responses, believed to be comparable to those exhibited by PZT, were recently identified in the 50:50 region, i.e., x = 0.5 of the $Na_{1-x}K_xNbO_3$ (KNN) phase diagram.[25,26] Such perovskites are, therefore, both a crucial and hugely attractive area of research within solid-state chemistry, with many potential applications to a variety of materials and devices.

Double perovskites are currently under extensive investigation owing, principally, to their magnetic and magnetoresistive properties.[27] B site substitutions in such perovskites are investigated more frequently as changes to the octahedral environment commonly contribute to the generation of useful properties. Many A site substitutions are also widely known and within this particular investigation work has been completed on a variety of A site substituted systems, namely $Na_{1-x}K_xNbO_3$ and $La_{1-x}Y_xScO_3$. A specific discussion of each can be found in Chapters 4 and 6 respectively. Ultimately, cation substitutions are driven by either specifically desired physical properties or potential applications of a particular material to certain devices. In many cases it is extremely challenging to accurately predict what effects will occur within a specific system, therefore simple trial and error methods are often necessary.

1.5 Cation Ordering

1.5.1 A site Ordering

Cation ordering across the A site occurs less often[28] and is typically only observed in anion deficient, double or triple-perovskites, for example $YBa_2Cu_3O_{7-x}$,[29,30] $LnBaFe_2O_{5+x}$[31-33] and $YBa_2Fe_3O_{8+x}$,[34] respectively. More

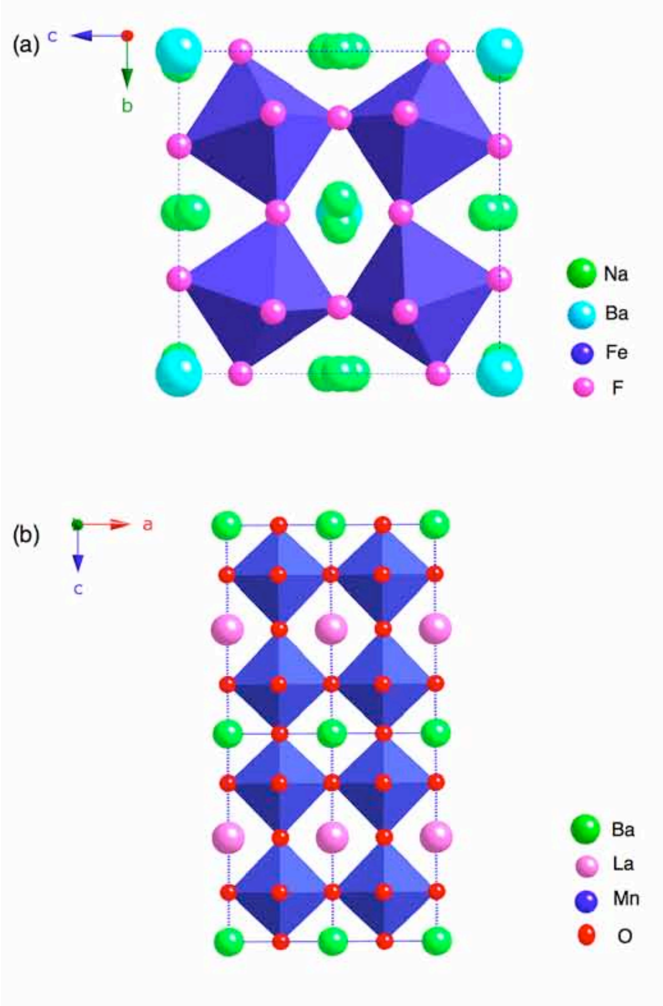

Figure 1.7: (a) An example of rock-salt ordering of the A-site cations in $Na_2BaFe_4F_{12}$,[38] and (b) an example of layered ordering of the A-site cations in $BaLaMn_2O_6$.[39,40]

recently, nonstoichiometric perovskites, $A_{1-x}BO_3$, have been shown to display layered cation ordering over the A site.[35-37] In many cases, to achieve ordering on the A site specific and often extreme experimental conditions such as high-pressure synthesis using diamond anvil cells are required to try and force the cations to order. Rock-salt ordering across the A site is exceptionally rare with only a single report of such behaviour in the literature, the A-site deficient $Na_2BaFe_4F_{12}$ shown in Figure 1.7(a).[38] Layered ordering, in contrast, occurs more readily on the A site, an example of which is $BaLaMn_2O_6$, illustrated in Figure 1.7(b).[39,40]

The anion environment plays a crucial role in the understanding of why rock-salt ordering is not favourable or often feasible across the A site.[41] When rock-salt ordering is exhibited across the B site in a system $A_2BB'X_6$ a mechanism is required to relieve stress and strain from the

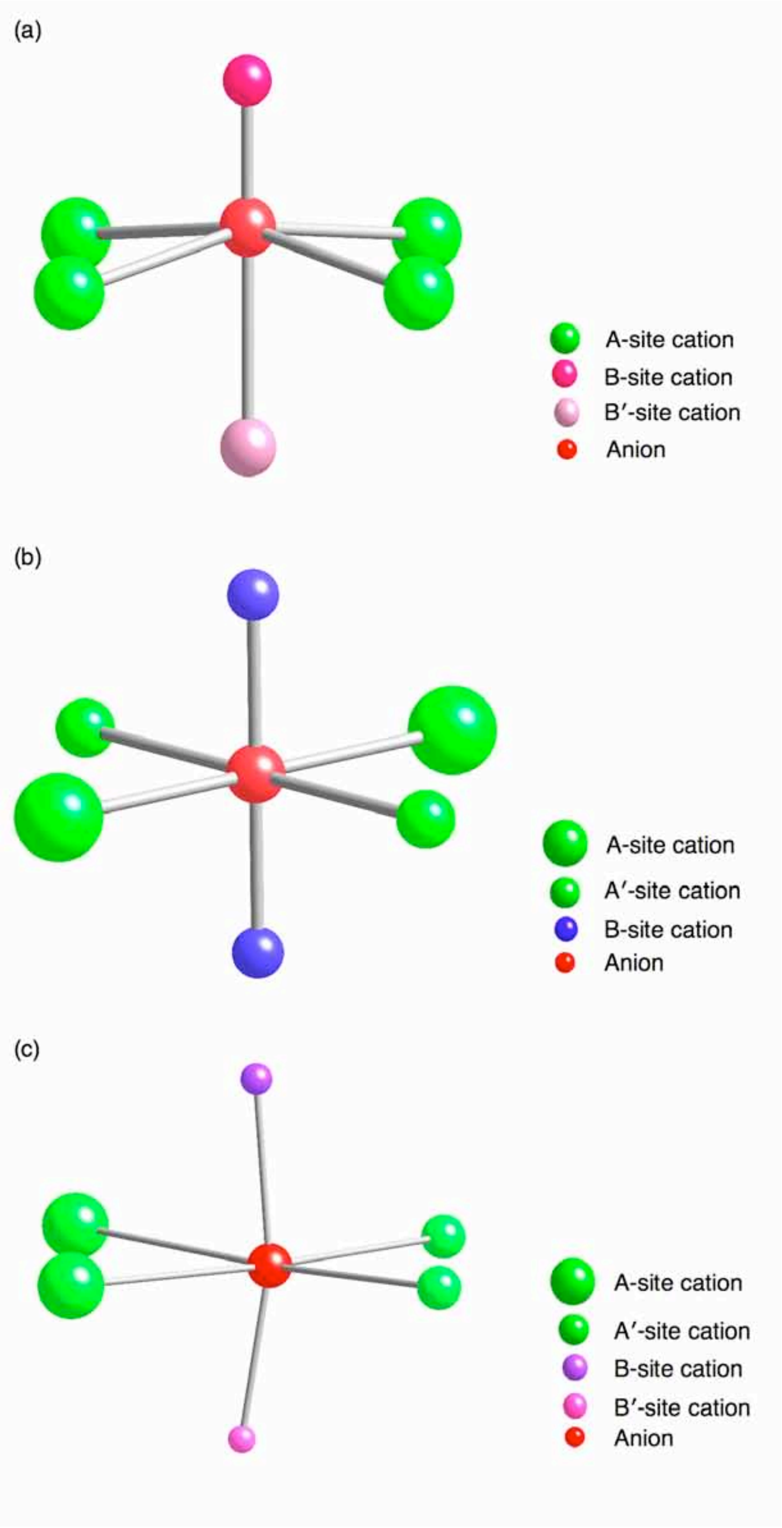

Figure 1.8: The anion environment for perovskites exhibiting: (a) rock salt ordering of the B-site cations, (b) rock salt ordering of the A-site cations and (c) layered ordering of the A-site cations.

structure, and therefore the anion moves towards the smaller of the two B-site cations, as shown in Figure 1.8(a). In a similar manner, if the position of the anion is considered in the system $AA'B_2X_6$ the anion is 'locked' in a plane coordinated to four A-site cations and two B-site cations (Figure 1.8(b)). As previously stated for cation ordering to occur there must be a significant mismatch in ionic radii and when a structure is as illustrated in Figure 1.8(b) there is no available space for movement or displacement of the anion to deal with such a mismatch. The anion is therefore held rigidly in a highly unstable formation. Rock-salt ordering across the A site is therefore not energetically feasible or favourable when there is a significant mismatch in ionic radii. Layered ordering is therefore highly favourable in such circumstances and is often adopted by many structures, as shown in Figure 1.8(c). In this case there is sufficient space for the anion to move when a significant difference in ionic radii is observed. Interestingly, layered ordering on the A site is not generally observed in stoichiometric perovskites in the absence of rock-salt ordering of B-site cations, as seen for example in $NaLaTi_2O_6$.[42] This does not exhibit long-range ordering of the Na^+ and La^{3+} cations as there is no octahedral site ordering.

1.5.2 B Site Ordering

In $A_2BB'X_6$-type perovskites the distribution of the B and B′ cations across the B site can be either random or regular. B-site cation ordering is highly desirable and, as a direct result, has been studied extensively within the perovskite literature.[43-47] It is well reported that octahedral-site cation ordering is particularly favourable when the stoichiometry is $A_2BB'X_6$ and there is a large difference in oxidation state and/or ionic radii of the B and B′ cations. If B is replaced by a cation of similar size there will be very little change to the size and shape of the already distorted octahedron. Such a small change produces no real effect on the stability of the structure, resulting in the B and B′ cations being randomly distributed over the B site. If, however, the deformation of the octahedron is very large after substitution the B-site cations will prefer to be in a certain

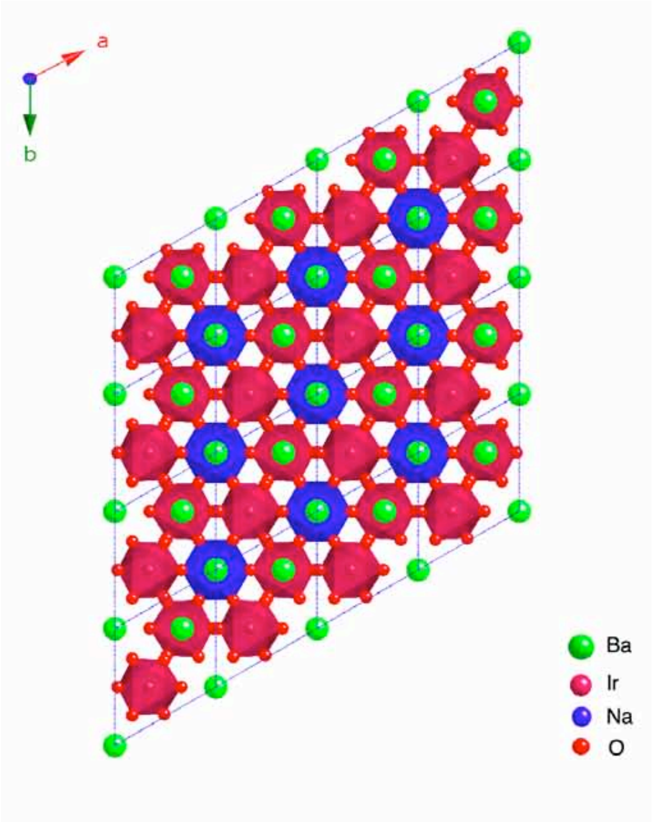

Figure 1.9: Example of a 2:1 ordered perovskite, Ba_3IrNaO_6.[49]

conformation so their arrangement can stabilise the perovskite structure, resulting in ordering of the cations. The extent of deformation exhibited by an octahedron depends upon both the difference in the ionic radii and the charges of the B and B′ cations. The polarisabilities of both B and B′ also play an integral role, as one may be more susceptible to deformation when under the action of the neighbouring ion. Therefore, all such factors must be taken into account when considering the potential for cation ordering across the B site. There are two major classifications for octahedral-site ordering; rock-salt and layered. The most commonly adopted within perovskite structures is rock-salt,[48] in which the cations B and B′ order into alternate octahedra. Octahedral-site ordering may occur for many different compositions, for example 2:1 ordered, $A_3B_2B'X_{12}$, and 3:1 ordered perovskites, $A_4B_3B'X_{12}$. Figure 1.9 illustrates Ba_3IrNaO_6, an example of a 2:1 ordered perovskite.[49]

Over many years there have been several attempts to devise a simple method for predicting whether perovskite-based systems will be ordered or disordered.[50-53] Liu *et al.*,[46] proposed an elementary set of equations to predict order or disorder within $A_2BB'X_6$ compounds. Their work began by defining two variables, X and Y, as shown in Equations 1.2 and 1.3 respectively,

$$X = \left(\left| \frac{Z_B}{r_B} - \frac{Z_{B'}}{r_{B'}} \right| \right) \tag{1.2}$$

$$Y = \left(\frac{100 \times |\Delta\alpha|}{N_A \times n_A} \right) , \tag{1.3}$$

where $\Delta\alpha$ is the difference in polarisabilities of the B and B′ cations; N_A and n_A are the principal quantum number and the number of electrons in the outer electron shells of the A atom respectively; Z_B / r_B and $Z_{B'} / r_{B'}$ are the ratios of the charges to the ionic radii of the B and B′ cations, respectively. When $X > 1.8$ the compound will be ordered, irrespective of the value of Y. However, if $X < 1.8$ the compound resides in a region between order and disorder and an additional parameter, Y_0 (Equation 1.4), is required to determine precisely where in the order-disorder phase diagram the compound lies.

$$Y_0 = -1.9X + 2.3 \tag{1.4}$$

Liu determined that an order-disorder transition region exists when $Y_0 = \pm 0.3$. Hence, if $Y > Y_0 + 0.3$ the compound will be ordered and if $Y < Y_0 - 0.3$ it will be disordered. In cases where $Y_0 - 0.3 < Y < Y_0 + 0.3$ the compound resides in the order-disorder transition region or is partially ordered. All methods of this type can be extremely useful as an aid to predicting whether ordering will occur however, in reality, factors such as temperature, cooling rate and particle size often affect whether a compound is ordered or disordered. It is virtually impossible to model such factors using simple equations; hence it is often extremely difficult for simple prediction systems to accurately match experimental results.

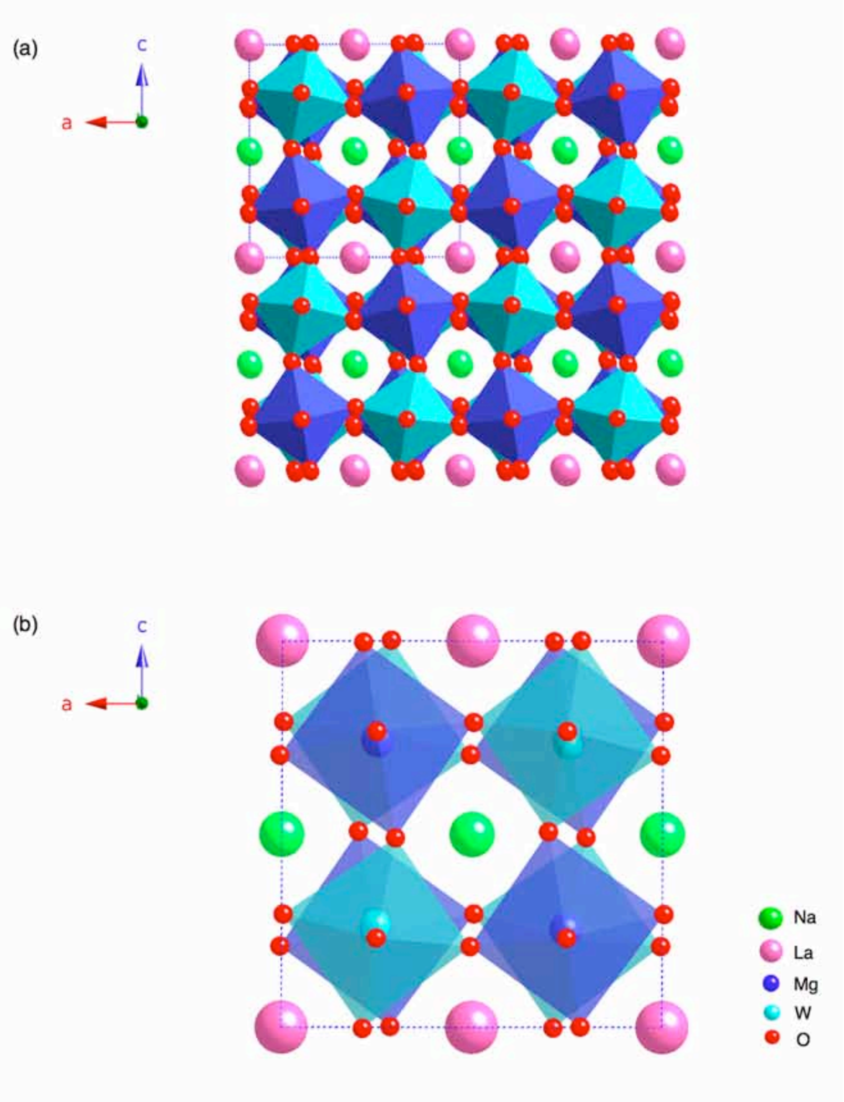

Figure 1.10: (a) The crystal structure of $NaLaMgWO_6$, a perovskite exhibiting simultaneous ordering of the A- and B-site cations. (b) An expansion of the unit cell in the $NaLaMgWO_6$ structure highlighting the simultaneous ordering observed.[54-56]

1.5.3 Simultaneous A and B Site Ordering

According to the literature only rarely can ordering be exhibited simultaneously across both the A and B sites. The first reported example of such behaviour was $NaLaMgWO_6$,[54-56] exhibiting rock-salt ordering of the Mg^{2+}/W^{6+} and layered ordering of the Na^{+}/La^{3+} ions, as illustrated in Figure 1.10. This compound is highly informative as it provides a valuable connection between B-site cation displacements and layered ordering, an area previously ignored within the perovskite literature.

Within the structure a Jahn-Teller distortion forces a displacement of the B′ cation which, in turn, stabilises layered ordering of the Na^+ and La^{3+} cations.[54] More recently such behaviour has also been reported for $NaLaScNbO_6$[41] and is believed to occur when the B′ cation is a d^0 transition metal in a high oxidation state. Subsequently, the following compounds have also been discovered to exhibit simultaneous ordering of the A- and B-site cations $KLaMgTeO_6$,[57] $NaLaMgTeO_6$,[57] $KLaMgWO_6$,[58] $NaLaCoWO_6$[59] and $NaLaNiWO_6$.[59] Now there is a better understanding of simultaneous ordering of the A- and B-site cations it is highly probable research will continue in this field. This will, presumably, lead to the development of methods for accurately predicting when simultaneous cation ordering will occur in such systems.

1.6 Layered Perovskites

Perovskites are currently one of the most heavily researched areas of solid-state chemistry owing to their extensive structural and compositional versatility. The basic perovskite unit, ABX_3, is routinely utilised as a structural 'building block' for a variety of diverse and interesting materials. In addition to the many solid-solutions and double perovskites previously discussed a variety of layered perovskite structures exist including Aurivillius, Ruddlesden-Popper and Dion-Jacobson phases, and Brownmillerites.

Perovskites possess both the ability and flexibility to exhibit various stacking mechanisms, producing a variety of layered perovskites. In recent years A_2BO_4-type oxides have received significant interest owing to the discovery of superconductivity within their structures.[60-62] Based upon the K_2NiF_4-type structure,[63,64] A_2BO_4 oxides form corner-sharing BO_6 sheets with rocksalt layers containing A-site cations lying between. An effective stacking system again requires the A- and B-site cations to be accurately matched to reduce the degree of tilting and rotation observed by the BO_6 octahedra. There are numerous stacking systems available with single, double or even triple perovskite layers separated by rock-salt or fluorite-type layers.

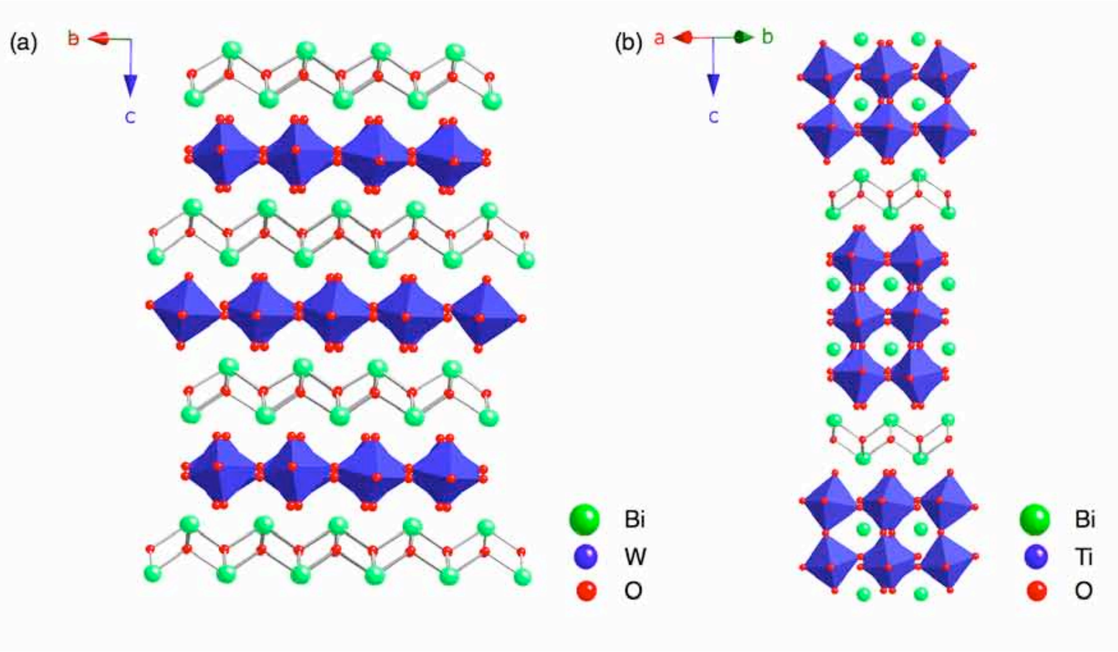

Figure 1.11: (a) Single-layer Aurivillius phase, Bi_2WO_6[67] and (b) 3-layer Aurivillius phase, $Bi_4Ti_3O_{12}$.[69]

1.6.1 Aurivillius Phases

Aurivillius phases are just one of many families of layered perovskites. First discovered over 50 years ago by B. Aurivillius[65,66] they exhibit a characteristic structure composed of $[A_{n-1}B_nO_{3n+1}]^{2-}$ perovskite-type blocks separated by $[Bi_2O_2]^{2+}$ fluorite-type layers, where A is a large 12-coordinate cation and B is a smaller 6-coordinate cation. An extensive family of Aurivillius phases exist and are classified according to the number of repeat perovskite layers, denoted by the integer *n*. Single-layer (Bi_2WO_6[67]), 2-layer ($SrBi_2Ta_2O_9$[68]), 3-layer ($Bi_4Ti_3O_{12}$[69]) 4-layer ($Bi_5Ti_3FeO_{15}$[70]) and mixed layer ($Bi_4Ti_3O_{12}$[71] mixed with $BaBi_2Nb_2O_9$[65]) Aurivillius phases are all widely known, two examples of which are shown in Figure 1.11.

1.6.2 Ruddlesden-Popper Phases

Work by Ruddlesden and Popper in 1957 led to the successful preparation of compositions such as Sr_2TiO_4, Ca_2MnO_4 and $SrLaAlO_4$,[72] regarded as the oxide derivatives of the well-known K_2NiF_4 structure. Successful determination of the structure $Sr_3Ti_2O_7$[73] a year later gave rise

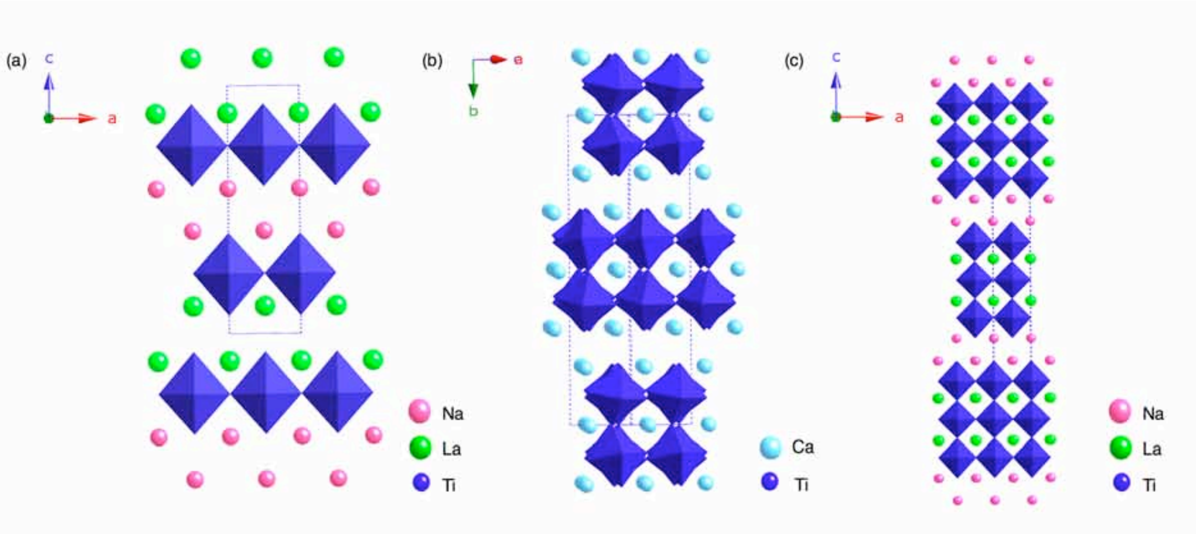

Figure 1.12: (a) 1-layer, $NaLaTiO_4$,[74] (b) 2-layer, $Ca_3Ti_2O_7$,[75] and (c) 3-layer, $Na_2La_2Ti_3O_{10}$,[76] Ruddlesden-Popper phases.

to a new family of layered perovskites now widely known as Ruddlesden-Popper phases, with general formula $M_2[A_{n-1}B_nO_{3n+1}]$. As expected with layered perovskites there are many 1-, 2- and 3-layer phases known, including $NaLaTiO_4$,[74] $Ca_3Ti_2O_7$[75] and $Na_2La_2Ti_3O_{10}$,[76] as shown in Figures 1.12(a), (b) and (c) respectively. Several Ruddlesden-Popper phases are known to possess ionic conduction capabilities, believed to occur through the interlayer region. A number have also been discovered to possess Colossal Magnetoresistance (CMR), thereby making such materials more desirable for use in devices. In recent years, several investigations have concentrated solely on 3-layer Ruddlesden-Popper phases with alkali metals in the interlayer and various lanthanides (Ln = La, Nd, Sm and Gd) on the A site within the perovskite blocks.[77] Such studies concluded that the lanthanide radius played a vital role in the ionic conductivity of a particular phase; a decrease in ionic size was accompanied by an increase in ionic conductivity. Trends in cation size are extremely important as they can often influence the physical properties exhibited by a particular perovskite or perovskite-based system.

The scope of interest for Ruddlesden-Popper phases has been extended by the possibility of proton conduction and many such studies are currently being undertaken.[78] Several Ruddlesden-Popper phases are well-known superconductors, for example the 1987 Nobel Prize in Physics

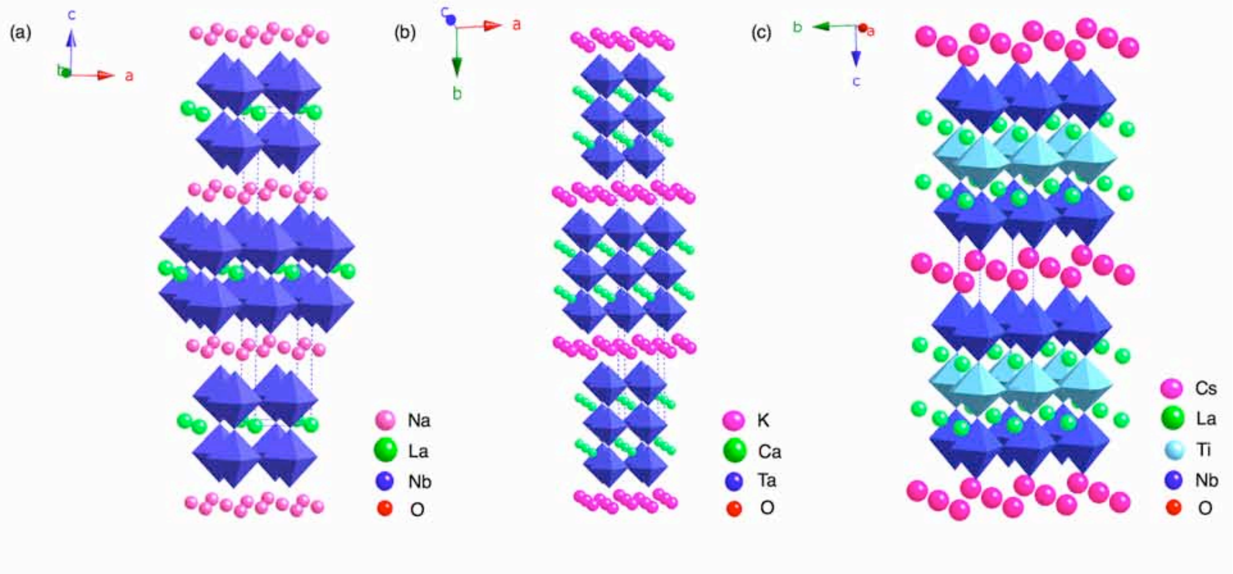

Figure 1.13: (a) 2-layer, $NaLaNb_2O_7$,[82] (b) 3-layer, $KCa_2Ta_3O_{10}$[83] and (c) $CsLa_2Ti_2NbO_{10}$ Dion-Jacobson phases.

was awarded to Bednorz and Müller for their discovery of superconductivity in ceramics materials, namely $(La,Ba)_2CuO_4$.[79] Many other additional phases have also been found to exhibit superconducting behaviour, including Sr_2RuO_4. Their practical application is, however, limited owing to the exceptionally low temperatures required to achieve such properties.

1.6.3 Dion-Jacobson Phases

One class of layered perovskites very closely related to Ruddlesden-Popper phases is the Dion-Jacobson family, general formula $A'[A_{n-1}B_nO_{3n+1}]$.[80,81] Structurally the two phases are extremely similar, with the only differences occurring in the composition of the interlayer. Ruddlesden-Popper phases have a double interlayer of cations whereas Dion-Jacobson phases possess only a single layer. Conventionally small alkali metals such as Li^+, Na^+ and K^+ are utilised in the interlayers of Ruddlesden-Popper phases. However, Dion-Jacobson phases are capable of accommodating larger cations such as Rb^+ and Cs^+, owing, predominantly, to the presence of a single interlayer. Commonly 3-layer Dion-Jacobson phases have compositions with divalent or trivalent cations on the A site of the perovskite block which, in turn, affects the valence of

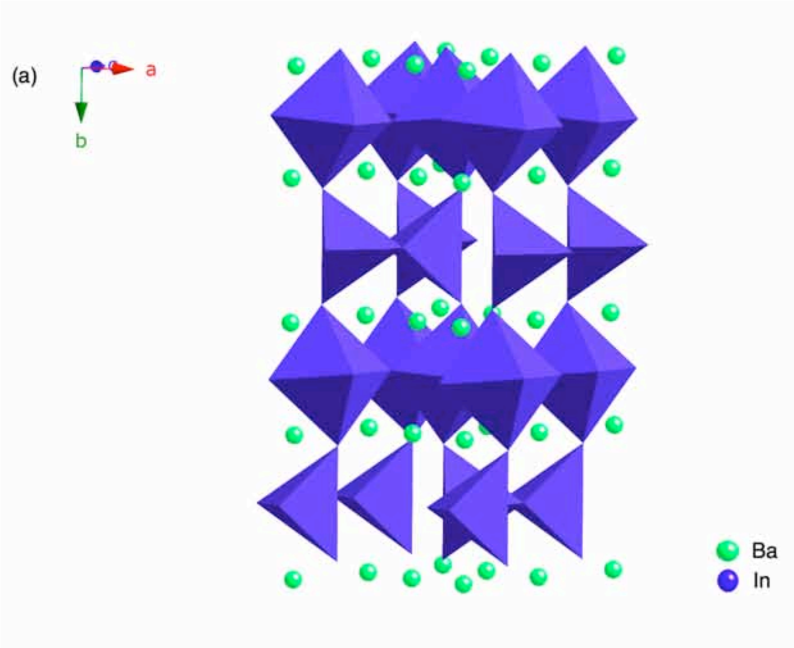

Figure 1.14: Example of the brownmillerite structure, $Ba_2In_2O_5$.[91]

the cation on the B site. For divalent cations the B site is usually fully occupied either by Nb^{5+} or Ta^{5+}. Trivalent cations however produce mixed valence on the B site. To date, there are no documented reports of single layer oxide Dion-Jacobson phases. Solely 2-layer ($NaLaNb_2O_7$[82]) and 3-layer ($KCa_2Ta_3O_{10}$[83]) oxide phases have been reported. Three examples of Dion-Jacobson phases are shown in Figures 1.13(a), (b) and (c) respectively. There are only very few known cases of Dion-Jacobson phases with greater than 3 layers.[84-87]

1.6.4 Brownmillerites

Brownmillerites are anion deficient derivatives of the perovskite structure, named after L. T. Brownmiller who first discovered the mineral $Ca_2[Fe,Al]_2O_5$.[88] The brownmillerite structure, shown in Figure 1.14, is composed of alternating layers of corner-sharing octahedra and distorted tetrahedra with oxygen vacancies in the ab plane.[89] Brownmillerites are studied extensively owing to their conduction capabilities.[90]

1.7 Physical Properties

Perovskites, or their derivatives, routinely possess enhanced physical properties such as ferro-, piezo- or pyroelectric behaviour, all of which are desired in a variety of materials and devices throughout solid-state chemistry. This is the principal reason perovskite-based materials are of such importance and significance.

1.7.1 Piezoelectricity

Piezoelectric ceramics respond to mechanical stress, becoming polarised and developing electrical charges on opposite crystal faces. The magnitude of the piezoelectric response observed depends upon both the crystal structure of the material and direction of the applied stress. Polarisation will, therefore, only occur when mechanical stress is applied in specific directions. The polarisation, P, and stress, σ, observed are related to the piezoelectric coefficient, d, by Equation 1.5. Conversely, the opposite is true, piezoelectrics can also develop a mechanical stress due to the application of an electric field.[91]

$$P = d\sigma \tag{1.5}$$

Potentially the most influential piezoelectric ceramic in materials science is $Pb[Zr_xTi_{1-x}]O_3$ (PZT).[24] Since its discovery in 1952 it has received considerable attention and is still heavily investigated. At varying compositions within the solid-solution different physical properties are exhibited. For example, it is known to be both ferroelectric ($x \geq 0.1$) and antiferroelectric ($x < 0.1$). To date, the largest dielectric responses were recorded when $x = 0.52$ at the MPB.[92-95]

1.7.2 Pyroelectricity[96]

Pyroelectric materials are closely related to ferroelectrics; however, the fundamental difference between the two is that the direction of the

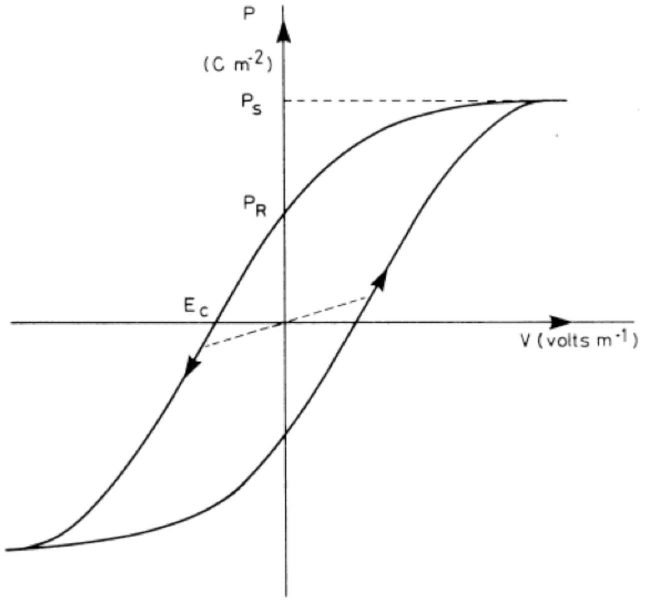

Figure 1.15: An example of a hysteresis loop of a ferroelectric material.[99]

saturation polarisation, P_S, cannot be reversed by application of an electric field. Temperature plays an integral role within pyroelectric materials, and only when the sample is heated will a change in P_S (Equation 1.6) be observed, as there will then be a change in the magnitude of the dipoles. The temperature dependence of P_S is given by

$$\Delta P_S = \pi \Delta T \tag{1.6}$$

where π is the pyroelectric coefficient.

Ferroelectric, piezoelectric and pyroelectric behaviour are closely related. By definition, ferroelectric materials are also pyroelectric and piezoelectric. In addition, pyroelectric materials are also piezoelectric. However, it must be noted that the reverse does not always hold, i.e., not all piezoelectric materials are pyroelectric.

1.7.3 Ferroelectricity

Ferroelectric behaviour was initially discovered in 1920 with the first ferroelectrically active material reported; Rochelle salt (potassium sodium tartrate), now known to rapidly lose all ferroelectric ability when its composition is slightly changed, thereby preventing any potential industrial application.[97] At that time ferroelectricity was considered a scientific curiosity and believed to be an order/disorder phenomenon associated with hydrogen bonding, and its true scientific importance had, at that stage, not been established. In 1945, $BaTiO_3$ was found to possess similar behaviour and, as a direct result, is now one of the most widely known and utilised ferroelectric materials. $BaTiO_3$ exhibits a significant displacement of the Ti^{4+} cation within the octahedron, resulting in long-range ordering of the dipoles. This type of displacement is routinely adopted by many perovskites. Of the several hundred ferroelectrics now known a large percentage are disordered perovskite structures displaying significant octahedral cation displacements.

To be ferroelectrically active a material must be non-centrosymmetric and exhibit spontaneous polarisation which may be reversed upon the application of an electric field. Polarisation is achieved by the presence of a net dipole moment, commonly the result of cation displacements. The temperature above which polarisation is lost is defined as the Curie temperature, T_C. When a potential difference is applied across a ferroelectric material the polarisation is increased until a saturation polarisation, P_S, is reached. Once the voltage has been removed a remnant polarisation, P_R, remains. To reduce the polarisation to zero a reverse field is required, known as a coercive field, E_C. The behaviour of a ferroelectric material under the application of a potential difference can be described by a hysteresis loop, as shown in Figure 1.15.[98] Ferroelectric materials are distinguished from ordinary dielectrics due to this behaviour, as common dielectrics do not possess the ability to retain large residual polarisations once the applied voltage has been removed. To be successfully utilised in commercial and industrial applications relatively high values of T_C are desired, i.e., close to room temperature. However, it is often extremely challenging to produce materials with adequate values, as many materials exhibit interesting ferroelectric properties at extremely low temperatures.

1.7.4 Applications of Perovskites

Currently, the largest commercial application of ferroelectrics is in capacitors using materials such as $BaTiO_3$ and PZT. In recent years there has been significant interest and research into finding potential 'green' replacements for PZT owing to toxicity issues regarding the presence and continued use of heavy metals such as lead. Therefore, a compound exhibiting piezoelectric responses equal to or superior to PZT needs to be discovered. Compounds containing heavy metal ions are renowned for producing exceptional piezoelectric and ferroelectric responses, but their use is limited owing to their toxic nature. Piezoelectrics have been routinely utilised as transducers to convert mechanical to electrical energy in a variety of diverse materials, for example they are applied as bimorphs in microphones, earphones and loudspeakers.[99] Pyroelectric materials are routinely used in infrared radiation detectors.[99] By far, materials exhibiting ferroelectric behaviour provide the greatest number of potential applications.

1.8 A Multidisciplinary Approach

The work presented within this thesis is the result of a multidisciplinary investigation combining two principal characterisation techniques within solid-state chemistry, namely powder diffraction and solid-state Nuclear Magnetic Resonance (NMR). When compared with X-ray and neutron powder diffraction, solid-state NMR is a relatively new technique with the first application of NMR to solids occurring in 1945 by Felix Bloch and Edward Mills Purcell.[100,101] This revolutionised chemistry. Bloch and Purcell later collected a Nobel Prize in physics (1952) for their contributions.

Powder diffraction and solid-state NMR are now recognised as being highly complementary to one another. Powder diffraction examines the long-range order of a material whereas solid-state NMR investigates and determines more local, short-range structural effects. Therefore, when used in combination they aid considerably in obtaining a better structural understanding and characterisation of a solid. Powder diffraction is principally used to identify the symmetry adopted within a structure. However, in some cases, this can be difficult to accurately determine using laboratory diffractometers owing to poor resolution. Hence, high-resolution data is often required, commonly synchrotron X-ray or neutron powder diffraction. The source utilised is often related to the material under investigation; for example, in some cases the sample may be too sensitive to be bombarded with neutrons and therefore high energy X-rays would be more favourable. Within this particular investigation a variety of dense ternary oxides have been investigated and for such materials neutron diffraction is often the only plausible option to successfully determine subtle structural effects such as phase transitions.

High-resolution solid-state NMR data has also been essential throughout this investigation. Lineshapes acquired in solution-state spectra are inherently narrower than those observed in the solid state owing principally to the presence of molecular motion when in solution. This motion averages any potential sources of broadening such as chemical shift anisotropies (CSA) or dipolar couplings.[102] In solids, however, there is usually no such averaging and therefore lines are often broadened. To obtain high-resolution spectra various experiments can be utilised to average the interactions that cause such broadenings and produce well resolved lineshapes. Specific details of these experiments can be found in Chapter 2. In many cases, solid-state NMR can provide additional information regarding the dynamics of a particular system and, in turn, provide essential structural information for often highly complex systems. Dynamics cannot be investigated easily using diffraction techniques and therefore solid-state NMR enables hugely important and significant additional information to be obtained for any system.

In addition, Density Functional Theory (DFT) calculations have been utilised routinely throughout this investigation. These calculations provide a direct link not only between experiment and theory but also between diffraction and NMR. Using DFT it is possible to calculate the NMR parameters for a particular structure and to do this an initial structural model is required, often provided by diffraction studies. DFT calculations are therefore a direct and convenient way of bridging the two techniques whilst also providing additional information often lost by experiment.

1.9 Thesis Overview

This thesis is concerned with the synthesis and structural characterisation of several perovskite systems using high-resolution powder diffraction, solid-state NMR and first-principles DFT calculations. Chapter 2 begins by introducing many of the basic principles of crystal symmetry and powder diffraction. The generation and practical implementation of both X-rays and neutrons to high-resolution powder diffraction experiments is also discussed. A basic description of the theory used in structural refinement is presented and the Rietveld method is introduced. The NMR phenomenon is also introduced within Chapter 2 and includes detailed considerations of the many interactions present during the course of an NMR experiment. In particular, a detailed description of the quadrupolar interaction and its effect upon NMR spectra is given. In addition, a detailed discussion regarding the practical implementation of first-principles calculations to periodic systems using DFT methods for the calculation of NMR parameters is given, and many of the basic methodologies relevant to the calculation of NMR parameters using first-principles DFT calculations are introduced.

Chapter 3 presents a detailed structural study of room temperature $NaNbO_3$. Particular focus is placed on the effect of different synthetic methods on the different phases of $NaNbO_3$ formed and their respective quantities. Conventional solid-state, molten salt and sol-gel techniques have been investigated and compared. A detailed discussion regarding the structural subtleties of the $NaNbO_3$ system is given and considerable emphasis is placed on the need for a multidisciplinary approach to achieve an accurate and complete structural conclusion. Both high-resolution X-ray and neutron powder diffraction data will be presented. In addition, ^{23}Na, ^{93}Nb and ^{17}O MAS NMR data and DFT calculations are presented, each of which highlights the importance of using a combined approach to characterise structurally complex compounds such as $NaNbO_3$.

Chapter 4 concentrates on the structural characterisation of several analogous $NaNbO_3$-based solid-solutions, namely $K_xNa_{1-x}NbO_3$, $Li_xNa_{1-x}NbO_3$ and $Na_{1-x}Sr_{x/2}\square_{x/2}NbO_3$. An understanding of the structure adopted after doping with the cations Na^+, Li^+ and Sr^{2+} is developed. The structural trends exhibited by each series are compared and the origin of the structural changes are discussed. Again, high-resolution X-ray and neutron powder diffraction techniques have been utilised to establish the structural subtleties exhibited by each system. The results obtained from each dataset will be presented in conjunction with the ^{23}Na MAS NMR data.

In Chapter 5 a low temperature structural study is presented using a sample of $NaNbO_3$ synthesised using a sol-gel approach. The same sample was initially characterised at room temperature in Chapter 3. Using high-resolution X-ray diffraction the structural changes observed as a function of temperature are discussed.

Chapter 6 presents a detailed structural study of $LaScO_3$, $YScO_3$ and the related solid-solution $La_{1-x}Y_xScO_3$ for compositions $x = 0.2$, 0.4, 0.6 and 0.8. High-resolution neutron diffraction data will be presented in conjunction with conventional and two-dimensional ^{45}Sc and ^{89}Y MAS NMR data and DFT calculations. The structural trends exhibited are presented and discussed, with possible reasoning as to why the observed changes occur.

Chapter 7 summarises the findings presented and suggests possible directions for future work.

Chapter 2

Experimental Techniques

2.1 Crystal Symmetry

2.1.1 Crystal Systems and Lattices[104,105]

Crystalline solids can be described by a periodic arrangement of atoms or ions in space. The simplest repeating portion of the structure, known as the asymmetric unit, yields the unit cell when translated, rotated or reflected. The unit cell can then be translated along all three dimensions to produce an infinite lattice, defined as an array of equivalent points in three dimensions. The lattice provides no information regarding the positional coordinates of any atoms; it simply displays the translational symmetry within a structure by locating equivalent positions. Increasing symmetry produces relationships between the various cell parameters that, in turn, leads to the definition of crystal classes. In total there are seven possible crystal systems (Figure 2.1) used to describe crystal structures, each governed by a minimum number of symmetry operations, as summarised in Table 2.1. As a direct consequence, a unit cell in each crystal system can be described using axes a, b and c, and angles α, β, and γ. Three-dimensional structures can also be described according to their lattice type, of which there are four possibilities; primitive (P), body centred (I), face centred (F) and side centred (C), illustrated in Figure 2.2. When combined with the seven crystal systems they give rise to the Bravais lattices, of which there are fourteen unique combinations.

2.1.2 Point Groups and Space Groups[104,105,106]

To fully describe a crystal structure more than simply the crystal system and lattice type are required. Crystals, owing to their infinite repeating structures, also possess some degree of space symmetry as opposed to solely point symmetry. There are 32 different point groups,

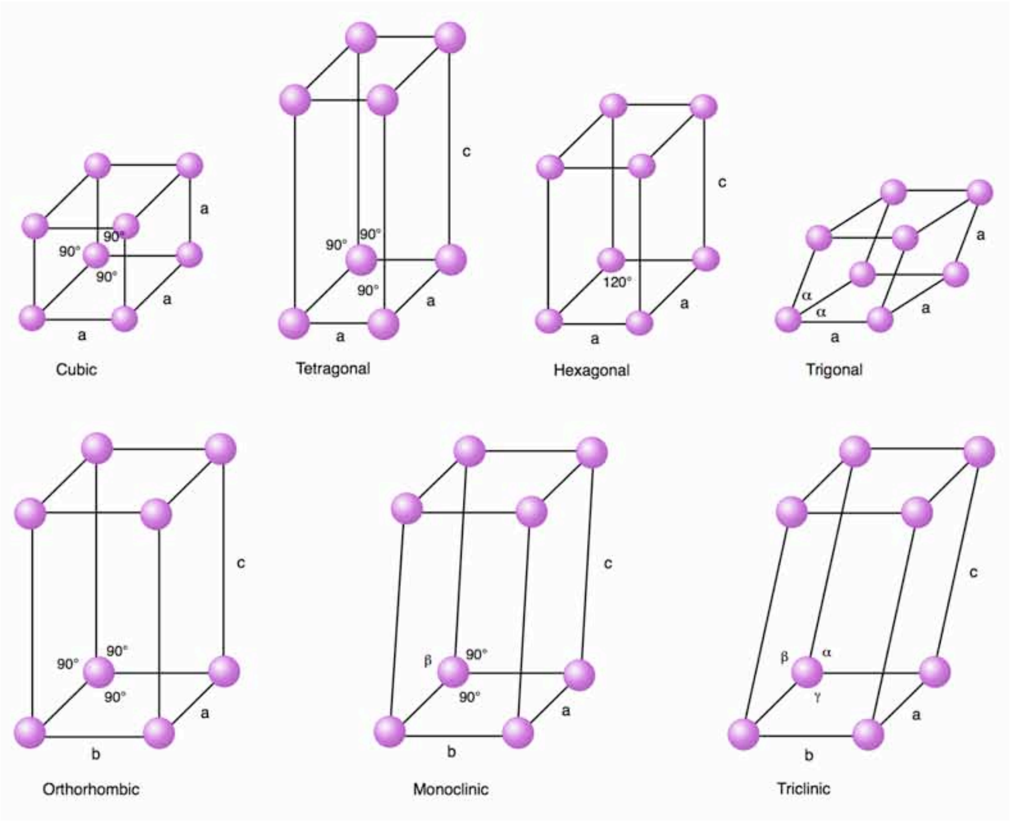

Figure 2.1: The seven crystal systems.

each of which provides information regarding the symmetry around a single point (rotations or mirror plane reflections). Point groups are therefore ideal for studying finite-sized molecules. In contrast, symmetry elements in the solid-state do not pass through a single point, instead they are regularly arranged as periodic solids. Space symmetry combines point symmetry elements with incremental translational steps giving rise to screw axes and glide planes. The symmetry of any system can then be characterised using a space group, a convenient and concise notation which utilises a set of pre-determined symbols to accurately summarise the symmetry elements exhibited. Space groups are extremely important as they provide key information regarding the crystal system, lattice type and elements of both the point and space symmetry exhibited by any one structure. In turn, they are routinely utilised throughout solid-state chemistry to describe all crystal structures. There are 230 space groups in total and the symmetry properties for each are well characterised. Details for each can be found in the International Tables for Crystallography, Volume A.[107]

Table 2.1: The seven crystal systems.[105]

Crystal Class	Symmetry Operation	Imposed Unit Cell Dimensions
Cubic	Four three-fold axes at 109.28° to each other	$a = b = c$ $\alpha = \beta = \gamma = 90°$
Tetragonal	One four-fold acis or one four-fold improper axis	$a = b \neq c$ $\alpha = \beta = \gamma = 90$
Hexagonal	One six-fold axis or one six-fold improper axis	$a = b = c$ $\alpha = \beta = 90°, \gamma = 120°$
Trigonal	One three-fold axis	$a = b = c$ $\alpha = \beta = \gamma \neq 90°$
Orthorhombic	Any combination of three mutually perpendicular two-fold axes or symmetry planes	$a \neq b \neq c$ $\alpha = \beta = \gamma = 90°$
Monoclinic	One two-fold axis or one symmetry plane	$a \neq b \neq c$ $\alpha = \gamma = 90°, \beta \neq 90°$
Triclinic	None	None

Space groups can be further classified into one of two categories; centrosymmetric or non-centrosymmetric. Structures that are non-centrosymmetric do not possess an inversion centre which often leads to many interesting physical properties, such as ferroelectricity. Solid-solutions are commonly synthesised, in which carefully selected cations are doped into the perovskite structure to try and force a structural transition to a non-centrosymmetric space group. In many cases, this is highly successful, enabling the physical properties exhibited by a particular perovskite to be 'tuned'. Perovskites in polar (non-centrosymmetric) space groups are therefore highly desirable as they commonly exhibit interesting physical properties that ultimately lead to many potential applications.

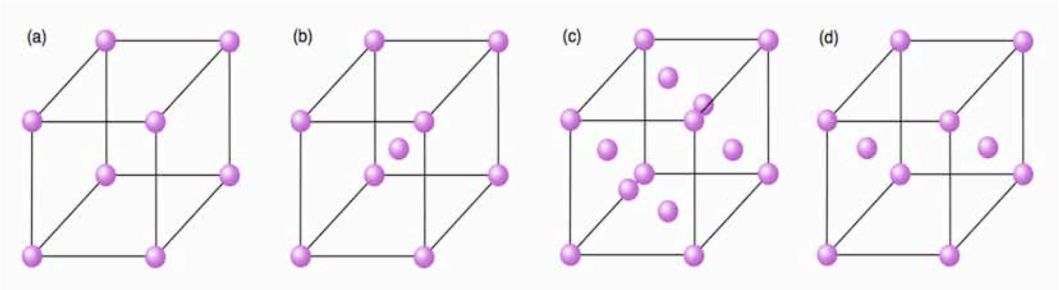

Figure 2.2: The four lattice types (a) primative, (b) body centred, (c) face centred and (d) side centred.

2.1.3 Miller Planes[108,109]

Bragg's Law, Equation 2.1, considers crystals as being composed of layers or planes of atoms, known as Miller planes, where adjacent planes are separated by an interplanar d-spacing, d_{hkl}. These planes are described by a set of integers known as Miller indices, commonly denoted as (*hkl*). Bragg's Law[110] governs diffraction, the physical process by which a beam of particles is refracted by a crystal and is given by

$$n\lambda = 2d_{hkl}\sin\theta \tag{2.1}$$

where n is an integer value, λ is the wavelength of the radiation used, d is the spacing between the lattice planes within a crystal and θ is the angle between the incident beam and the sample. Consider the path of two X-ray beams reflected from two adjacent planes within a crystal, as illustrated in Figure 2.3. The beam reflected from the lowest of the three planes travels an extra distance, XY + YZ. When this path length difference is an integer number of wavelengths constructive interference results and Bragg's Law is satisfied. Bragg's Law imposes extremely stringent conditions on the angles at which reflections may occur and if the angle of incidence is incorrect by even a few tenths of a degree cancellation of the reflected beams will occur. In reality diffraction patterns are plotted as a function of 2θ rather than θ as 2θ corresponds to the angle between the X-ray source and the detector, i.e., the path of incident and reflected X-rays. Bragg's Law is considered a highly simplistic model to describe how X-rays are reflected in reality. The

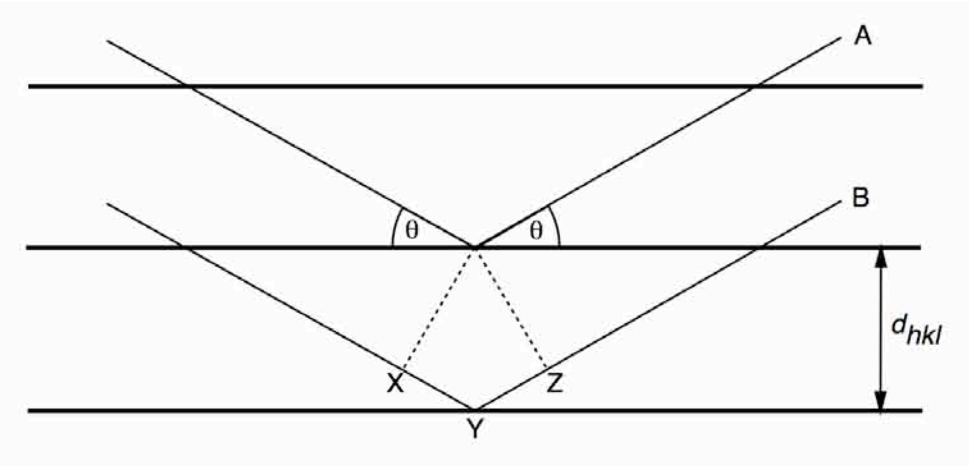

Figure 2.3: X-rays reflecting off adjacent planes.

'planes' described by Bragg are merely a concept rather than a physical reality. Crystal structures are large three-dimensional networks resulting from a regularly repeating unit cell, as previously discussed. Planes can be used to divide up the unit cell into various different orientations and it is this concept of planes that is utilised in the derivation of Bragg's Law. For extremely simple crystal structures the planes can correspond to layers of atoms however, in reality, this is generally not the case as atoms are commonly located on sites that do not correspond to such 'layers'.

2.1.4 The Reciprocal Lattice[111-114]

The reciprocal lattice is essential in the understanding of diffraction. To fully comprehend the concept of reciprocal space it first must be understood that diffraction patterns do not display the real-space reflections of a crystal. Instead, all diffraction patterns are functions that exist as a regular three-dimensional lattice known as the reciprocal lattice, defined with reference to a particular Bravais lattice. The reciprocal lattice is a vector perpendicular to the Miller planes and can be regarded as the Fourier transform of the real space or direct lattice of a crystal. The magnitude of this vector is the reciprocal of the interplanar distance and the reciprocal lattice parameters can be calculated from those of the crystal lattice in real space by $1/d_{hkl}$, where d_{hkl} is the spacing between the Miller planes.

2.2 Diffraction Techniques

The powder diffraction techniques utilised within this particular study can be separated into three main categories conventional (laboratory) X-ray diffraction, high-resolution synchrotron X-ray diffraction and high-resolution neutron diffraction.

2.2.1 X-rays

X-rays, electromagnetic radiation of wavelength ~1 Å, were initially discovered by Wilhelm C. Röntgen in 1895. The first description of X-ray diffraction (XRD) and subsequent diffraction pattern of a crystal followed seventeen years later by Max von Laue and Paul Knipping.[115] X-rays possess a wavelength comparable to interatomic distances making them suitable for the structural characterisation of many complex solids. In 1913 William H. Bragg and his son, William L. Bragg, devised a method and equation (Bragg's Law) to describe diffraction that revolutionised the technique and is now universally used as the basis for X-ray diffraction geometry, as previously discussed in section 2.1.3.

2.2.2 Generation of X-rays[108,116,117]

Laboratory X-rays are conventionally generated using an X-ray tube, where a beam of electrons (produced from a tungsten filament) is accelerated towards a metal target, commonly copper. As electrons penetrate the metal target they decelerate and generate radiation with a continuous range of wavelengths, known as Bremsstrahlung or 'white radiation'. The X-ray tube used to produce monochromatic radiation is evacuated and held under vacuum to avoid collision of the incident electrons and/or X-rays with air particles.

The accelerated incident electrons possess sufficient energy to ionize some of the 1s electrons in the copper and upon impact an electron is expelled from the inner shell and an electron of higher energy from an outer orbital, typically a 2p or 3p electron, drops down to occupy the

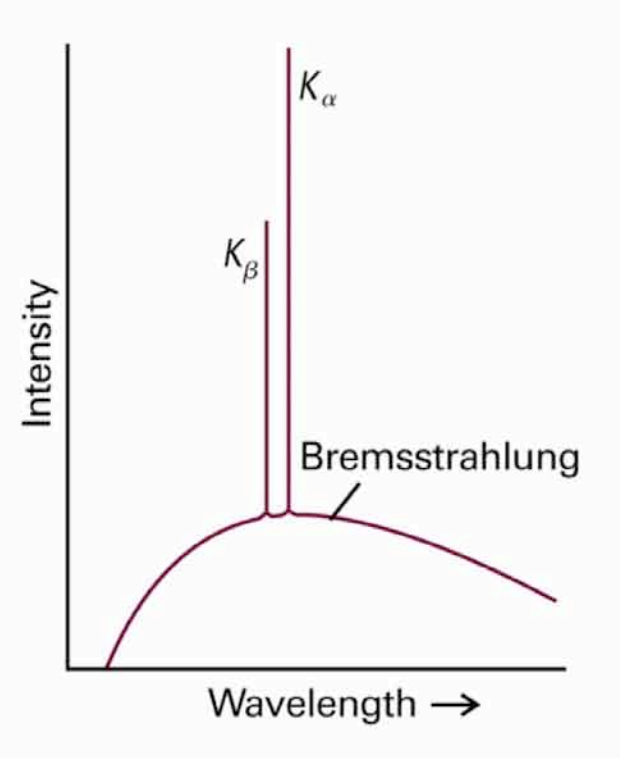

Figure 2.4: Bremsstrahlung radiation.[118]

vacant shell. Such electronic transitions result in the release of monochromatic X-rays and peaks corresponding to this radiation are superimposed onto the broad featureless Bremsstrahlung background, as shown in Figure 2.4. For copper the 2p → 1s transition, K_α, has a wavelength λ = 1.5418 Å whilst the 3p → 1s transition, K_β, has a wavelength λ = 1.3922 Å. The K_α transition occurs more frequently and is, in turn, more intense when compared with K_β transitions. As K_α radiation is more desirable for use in X-ray diffraction experiments, a method is required to accurately separate out the K_α and K_β radiation. Various metals filters, known as monochromators, can be utilised to successfully split the two; however their effectiveness is dependent upon the metal target initially used. For copper, Ni foil is extremely effective as a monochromator as it successfully absorbs the K_β radiation leaving a monochromatic beam of Cu K_α radiation.

The desirable K_α radiation is, in reality, a doublet composed of $K_{\alpha 1}$ = 1.54051 Å and $K_{\alpha 2}$ = 1.54433 Å. This is a consequence of spin multiplicity in the p shells , and therefore the 'K_α line' in the copper spectrum has two lines instead of one. Patterns obtained by X-ray diffraction using both $K_{\alpha 1}$ and $K_{\alpha 2}$ often appear broadened and poorly resolved. Therefore, to overcome this problem and improve resolution the weaker $K_{\alpha 2}$ beam can be removed from the incident radiation using an appropriate monochromator. Most modern diffractometers currently operate using monochromatic X-rays composed of solely Cu $K_{\alpha 1}$ radiation.

2.2.3 X-ray Scattering and Powder Diffraction

X-rays interact with electrons present in matter and, upon contact with an inorganic compound or crystal a beam of X-rays, will be scattered in various directions by the electron density. The scattering factor or form factor, f, of an atom is directly proportional to the atomic number, Z, or, more accurately, the number of electrons possessed by a particular atom. There is a fall off in scattering power for X-rays owing to the finite size of the electron cloud, highlighted in Figure 2.5 for Ca^{2+} and F^{-}. The scattering factor is also dependent on the scattering angle, $\sin\theta/\lambda$, also illustrated in Figure 2.5. Atoms such as oxygen and hydrogen scatter X-rays weakly therefore it is often extremely challenging to locate their position when much heavier elements are present. The more electrons an atom possesses the more intense the scattered X-rays will be. Compounds containing several elements of similar atomic number can be exceptionally difficult to characterise as each element will scatter the X-rays in essentially the same manner. The structure factor, F_{hkl}, is related to the scattered intensity in any diffraction pattern and the structure factor for a particular reflection can be defined as

$$F_{hkl} = \sum_{i=1}^{N} f_i \exp(2\pi i(hxi + kyi + lzi)) \tag{2.2}$$

where f_i is the scattering factor, hkl are the Miller indices of a particular plane and (xi, yi, zi) are the fractional coordinates of each of the atoms within the unit cell. The intensity of this reflection is given by

$$I_{hkl} = F_{hkl}^2 \quad . \tag{2.3}$$

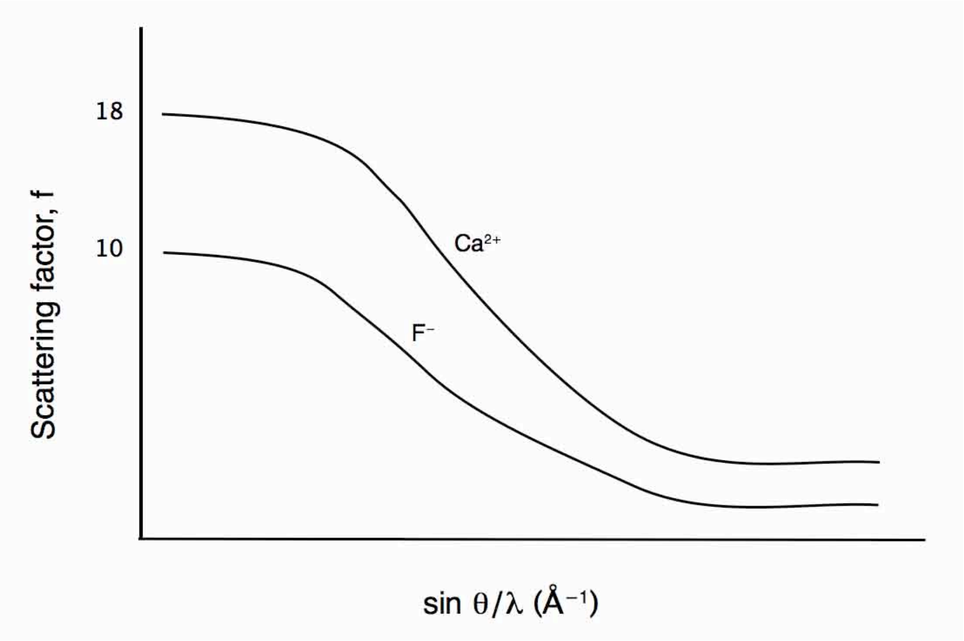

Figure 2.5: Fall off in scattering power for X-rays.

Polycrystalline samples are composed of millions of tiny crystallites, each with a different orientation. As a result, when an X-ray beam strikes a powdered sample it is diffracted as cones of radiation in all possible directions, as illustrated in Figure 2.6. Each cone is composed of a set of closely spaced dots, each of which represents diffraction from a single crystallite within the sample. When large numbers of crystallites are present the dots join together resulting in one continuous cone. To convert these 'cones' of radiation to a real space diffraction pattern a transformation from three to two-dimensional space is required, i.e., envisage taking a 'slice' through one particular cone from its point to its base, this is then represented in the diffraction pattern obtained. A highly diffracting (electron rich) atom with a very distinct location will produce an intense, narrow peak in the powder pattern. The converse is also true with broad peaks indicating weakly diffracting atoms. The powder pattern obtained is characteristic of the sample under analysis.

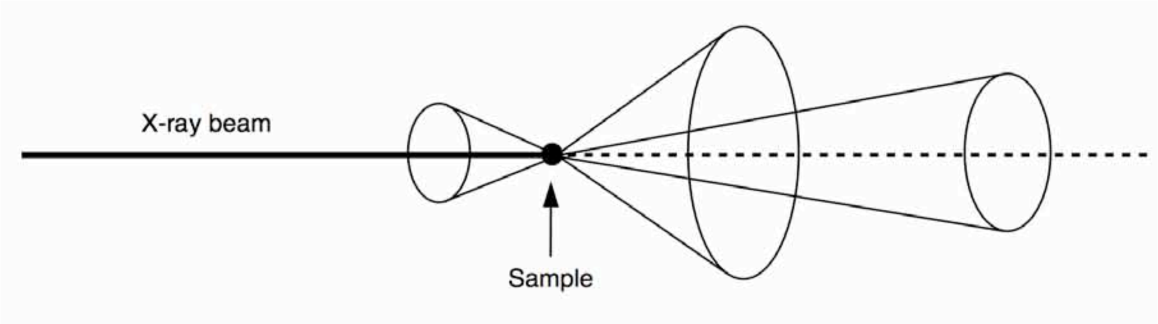

Figure 2.6: Cones of radiation produced in diffraction.

2.2.4 Conventional X-ray Diffraction

All "laboratory" powder diffraction (l-PXRD) experiments were completed on a Stoe STADI-P X-ray diffractometer equipped with a position-sensitive detector (PSD) and using Cu anodes with primary beam (Ge Crystal) monochromation, producing Cu $K_{\alpha 1}$ radiation ($\lambda = 1.54056$ Å). Samples were ground to a fine powder and mounted between two lightly greased Mylar film disks. Once prepared the film was mounted onto a sample disk. Diffraction patterns were initially collected from 5° to 70° (2θ angles) in steps of 0.02° using a continuous scan time of 12 s. Where necessary, higher quality patterns were obtained by increasing the scanning rate.

2.2.5 Generation of Synchrotron X-rays[115,116,119]

Synchrotron light is emitted when a beam of electrons travelling close to the speed of light is bent by a powerful magnetic field and the light produced spans the entire electromagnetic spectrum, producing X-rays, infrared and ultraviolet light. To date, there are approximately 50 operating synchrotrons in the world, the three biggest being the APS (USA), ESRF (France) and Spring-8 (Japan). Synchrotron radiation is currently of considerable use in the structural characterisation of many

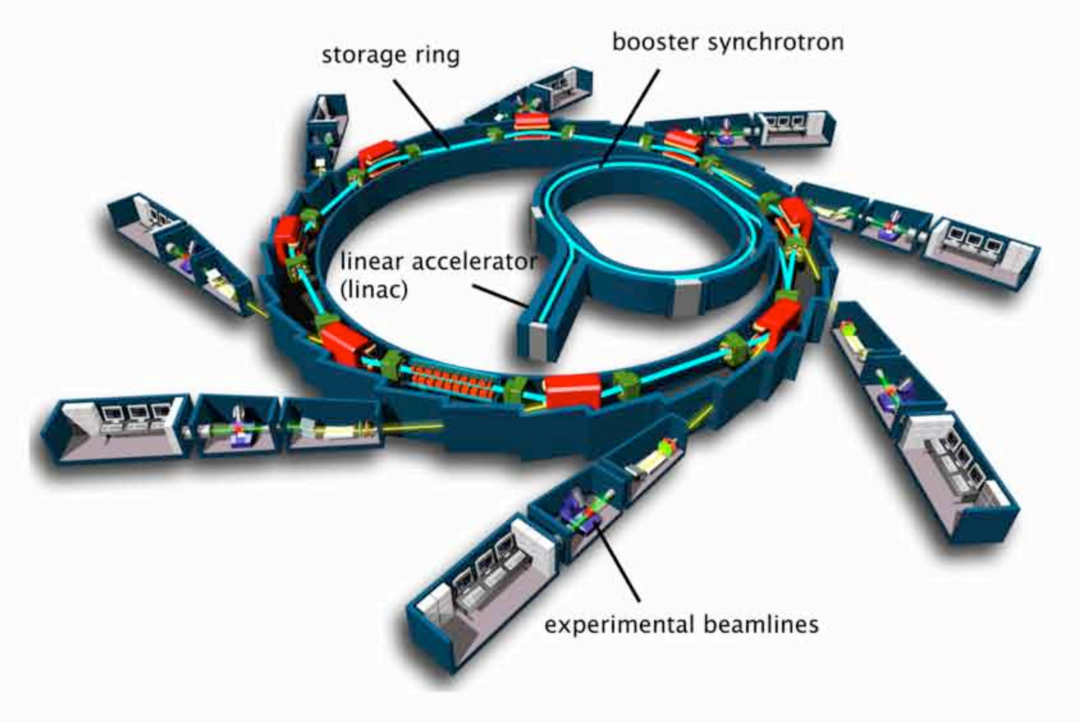

Figure 2.7: A schematic representation of a synchrotron facility.[120]

complex solids and is utilised across many disciplines, principally chemistry, physics and biology.

For example, at Diamond Synchrotron Light Source[121] electrons are produced in an electron gun and accelerated through a series of three particle accelerators namely the linear accelerator (linac), booster synchrotron and large storage ring, as shown in Figure 2.7. The electrons are initially accelerated to 100 MeV using the linear accelerator, after which they enter into the booster synchrotron where they follow a specially designed trajectory composed of both straight and semicircular curved sections. To drive the electrons round the bends within the booster synchrotron dipole bending magnets are utilised. When in the straight sections a radiofrequency (rf) voltage source is used to further accelerate the electrons until they reach an energy of 3 GeV. Once the correct energy is reached electrons are transferred into the third and final particle accelerator, the storage ring. In a similar manner to conventional X-ray sources the storage ring is held under vacuum to prevent interaction or collision of the electrons with air particles.

Electrons emit very intense beams of X-rays, infrared and ultraviolet light called synchrotron light as they travel round the storage ring. As this occurs the electrons become lighter and their path through the ring begins to change until they eventually hit a wall and are lost. To compensate for this loss the RF system in the booster ring provides each electron with a 'kick' each time they complete one cycle of the ring. This 'kick' replaces the energy lost in the previous cycle enabling them to then follow the correct path. The length of time the electrons remain in the storage ring is defined as the lifetime of the beam. When circulating in the ring the electrons collide with the few particles that remain in the vacuum and are then lost, thereby requiring new electrons to be added. Modern third generation synchrotron sources, such as Diamond Light Source Synchrotron,[121] function using a 'top-up' mode where the electron beam is topped up at regular intervals. This is a highly advantageous system as the beam is highly stable and the quality of beam produced remains high for longer periods of time.

The dimensions of the storage ring are dependent solely upon the research facility utilised. The work presented within this particular investigation used Diamond Light Source Synchrotron, Didcot, United Kingdom.[121] Diamond's storage ring has a circumference of 562 m and is composed of 24 straight sections that are angled together to form a closed loop. Inside the storage ring 48 large electromagnets or dipole magnets are utilised to curve the electron beam between adjacent straight sections. Beamlines are strategically placed at tangents to the ring to guide narrow beams of synchrotron light into the various experimental hutches. Each beamline is specifically designed for a particular type of experiment, for example high-resolution powder diffraction, small molecule diffraction and diffraction using extreme conditions (such as diamond anvil high pressure cells). Synchrotron X-rays are more intense than laboratory sources and offer a wide range of tunable wavelengths. Synchrotron sources are a highly desirable facility and, as a result, user time available is becoming increasingly limited.

2.2.6 Synchrotron X-ray Diffraction

All high-resolution X-ray diffraction data was collected using beamline I11 (high-resolution powder diffractometer) at Diamond Light Source Synchrotron (λ = 0.827267 Å), shown in Figure 2.8.[122-124] Within this particular study both room and low temperature diffraction experiments were completed using this facility. Room temperature samples were loaded into 0.5 mm or 0.7 mm glass capillaries and mounted on brass capillary spinners. The low temperature investigation was conducted using a PheniX cryostat (11 – 295 K) in which the sample was loaded into an aluminium capillary and mounted onto a flat brass plate that employed a continuous 'rocking' motion throughout data collection. Peaks resulting from the aluminium capillary were present in all low temperature diffraction patterns obtained and for ease of analysis these peaks were excluded from the data during Rietveld refinement. All data was automatically collected from 5° to 145° using the five multi-analysing crystal detectors (MACs), each composed of 9 Si (111) analysing crystals and 9 detectors. Typical collection times were between thirty minutes and one hour. Only data up to and including 70° was utilised and analysed using the General Structure Analysis System (GSAS) software package.[125]

2.2.7 Neutron Diffraction[126]

The neutron is an uncharged particle with spin 1/2 and mass 1.675 × 10^{-27} kg. Neutrons, unlike X-rays, are scattered by atomic nuclei, thereby making neutron diffraction isotope specific. This can be of considerable use when trying to distinguish between different isotopes of the same element, as each will scatter neutrons in a different manner. The scattering factor for neutrons is therefore not proportional to the number of electrons and, in turn, does not diminish with scattering angle, as shown in Figure 2.9. Neutrons are exceptionally effective in locating lighter elements, such as oxygen and hydrogen, when in the presence of much heavier elements such as bismuth and lead. Unlike X-rays neutrons possess spin, $I = 1/2$, therefore they have the ability to interact with any

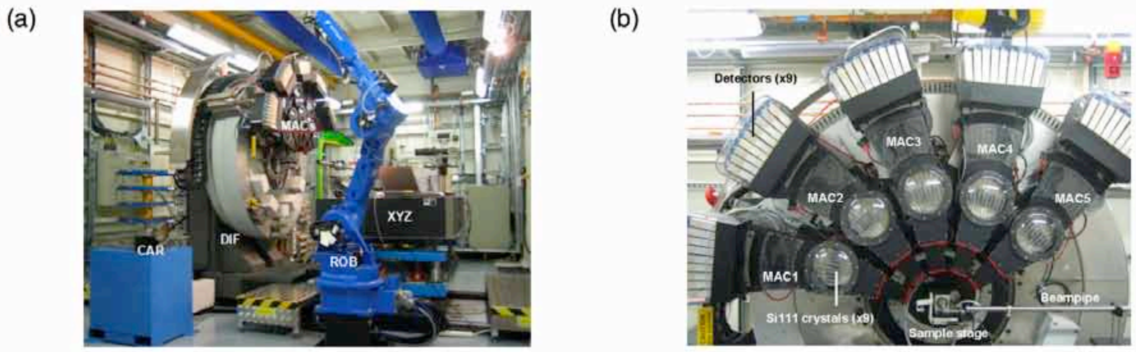

Figure 2.8: Beamline I11 at Diamond Light Source Synchrotron.[124]

magnetic species in a sample, making them an invaluable tool for solving complex magnetic structures. If magnetic centres of interest are present there will be additional interactions with the neutrons bombarding the sample, resulting in the appearance of extra peaks in the diffraction pattern obtained. However, there are many associated disadvantages of the technique, principally the high running and maintenance costs, the complexity of generating neutrons and the large sample quantities required (typically 5 g for powder diffraction). Furthermore, user time allocated at neutron sources is becoming increasingly limited and, in turn, highly competitive.

2.2.8 Generation of Neutrons[127,128]

Neutrons are generated from one of two sources, either a nuclear reactor or a spallation source. The first of these relies upon a series of controlled chain reactions of neutron-induced fission of a heavy nucleus, most commonly ^{235}U. In a spallation source a heavy metal target is bombarded by high energy protons (~50 MeV), generated using a linear particle accelerator. Modern spallation sources utilise a synchrotron in conjunction with the linear accelerator to produce higher energy protons (~800 MeV). During collision of the protons with the metal target enough energy is imparted to the target to produce spallation neutrons. However, the neutrons produced in each case are too high in energy and possess too short a wavelength to be utilised in diffraction experiments. Therefore, to

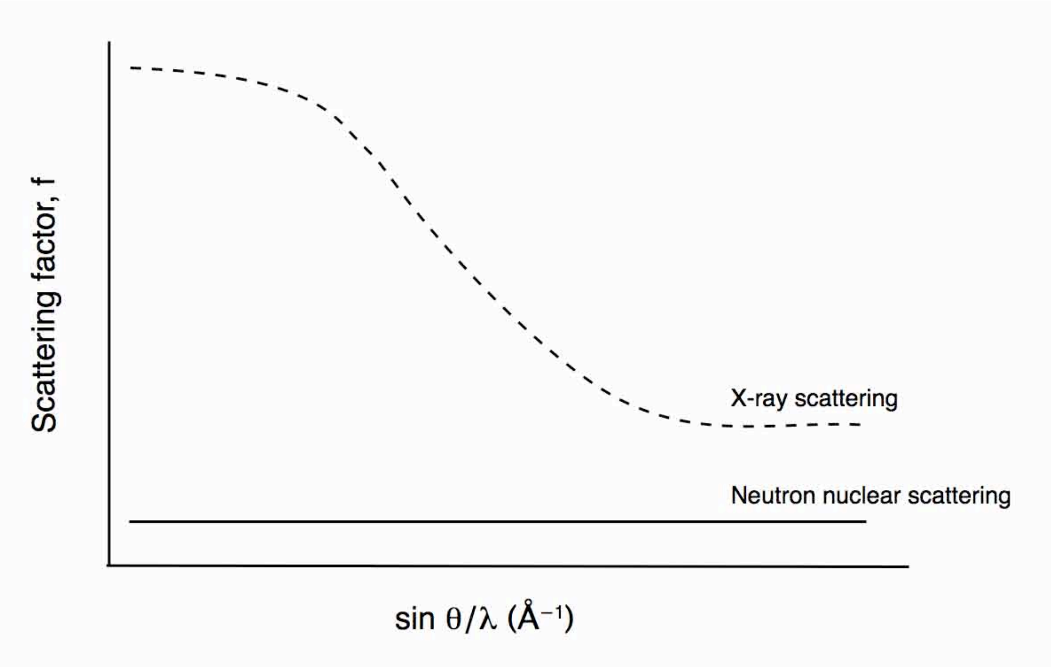

Figure 2.9: Schematic representation of the neutron scattering factor.

be used effectively the neutrons need to be slowed, i.e., reduce their frequency, using a moderator, the type of which varies depending upon the facility used. Once the neutrons have been slowed sufficiently to reduce their frequency the corresponding wavelength will be increased. There are, however, fundamental differences between the neutrons produced by a nuclear reactor and those from a spallation source. Neutrons from nuclear reactors need to be passed through a monochromator to reduce the neutrons incident on a sample to a single or 'fixed' wavelength. In this type of experiment the detector is then moved during data collection. An example of a fixed wavelength facility is the high-resolution D2B diffractometer (λ = 1.594 Å) at the Institut Laue-Langevin (ILL), Grenoble.[128] In contrast, neutrons from spallation sources arrive at an instrument in 'bunches'; hence neutrons possessing a variety of wavelengths are utilised and separated according to their different velocities. In such cases, fixed detector banks are used because each of the wavelengths will diffract off the *hkl* planes in the structure with different d-spacings. This technique is known as time-of-flight (TOF) neutron diffraction and one example of such a diffractometer is POLARIS at the ISIS neutron spallation source, United Kingdom.[129] Within this particular structural investigation solely TOF neutron diffraction experiments have been completed, specific details of which can be found in the following sections.

2.2.9 POLARIS[130-133]

POLARIS is a medium resolution TOF neutron powder diffractometer located at the ISIS neutron spallation source, Rutherford Appleton Laboratories, Didcot, United Kingdom. POLARIS consists of three fixed detector banks, backscattering (130-160°), 90 degrees (85-95°) and low angle (28-42°) composed of ^{3}He tube, ZnS scintillator and ^{3}He tube detectors respectively. The sample is conventionally held in a cylindrical vanadium can in a tank evacuated to pressures of ~0.1 mbar. Samples are held under vacuum principally to avoid collision of the incident and scattered neutrons with air. All experiments completed using POLARIS were under ambient reaction conditions with use of the sample changer. Once collected, all datasets were normalised using the GENIE program and converted into GSAS format for compatibility with the GSAS software.

2.2.10 High Resolution Powder Diffractometer (HRPD)[134,135]

HRPD is the high-resolution TOF neutron powder diffractometer situated at the ISIS neutron spallation source, Rutherford Appleton Laboratories, Didcot, United Kingdom.[129] To gain the required high-resolution HRPD possesses an extended flight path and is therefore located ~100 m from the ISIS target at the end of the neutron guide. HRPD is utilised principally in the study of complex materials exhibiting subtle structural variations such as phase transitions, hence extremely accurate and precise crystallographic data is required to characterise such changes. HRPD is currently the highest resolution neutron powder diffractometer of its type in the world and consists of three fixed detector banks, the backscattering (160-176°), 90 degree (87-93°) and low angle (28-32°) banks. Both the backscattering and 90 degree banks are composed of

ZnS scintillator detectors whilst the low angle bank uses ^{3}He tube detectors. The highest resolution data is acquired using the backscattering bank with a δd/d resolution of ~4 x 10^{-4} and can record out to d-spacings of up to 6 Å. The measurable d-spacing range can be extended to over 20 Å using the complementary detectors at 90 degrees and low angle; however, the resolution is considerably reduced. Samples are conventionally held in vanadium cans, the size of which varies depending upon sample quantity. All experiments were completed under ambient reaction conditions. Once collected, all datasets were normalised using the GENIE program and converted to the relevant GSAS format for compatibility with the GSAS software.

2.2.11 Comparison of Diffraction Techniques

Laboratory X-ray diffraction is typically only sufficient to determine phase purity owing to relatively low resolution and poor data quality. Synchrotron X-ray and neutron diffraction are superior techniques owing, fundamentally, to higher resolution. A comparison of data obtained from each of the three sources is shown in Figure 2.10 and highlights the considerable differences in peak definition and overall resolution. In particular, the signal-to-noise ratio is greatly improved in both the synchrotron XRD and neutron data when compared with the laboratory XRD data. Neutron diffraction is often essential in the structural characterisation of dense ternary oxides as location of the oxygen atoms within such structures is extremely challenging and requires well-resolved, precise crystallographic data. Neutron diffraction is also known to enhance superstructure peaks within such solids; hence it is possible to identify any superstructure characteristics exhibited. Within this particular investigation neutron diffraction was of considerable use as it enabled the key identification of subtle structural discrepancies otherwise unseen using high-resolution X-ray methods.

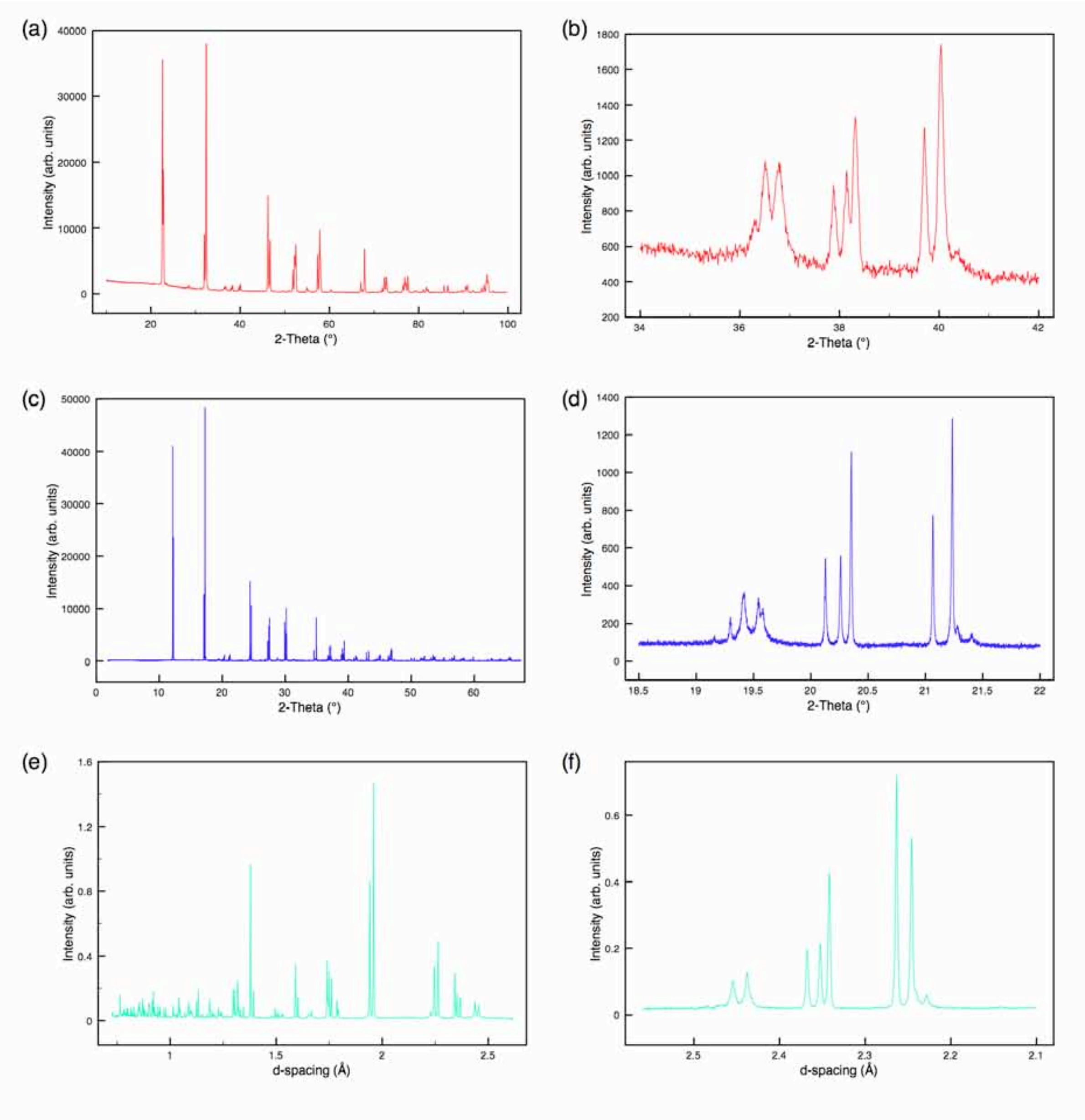

Figure 2.10: Comparison of Rietveld profiles for commercial $NaNbO_3$ (Aldrich) obtained from (a) conventional "laboratory" XRD, (c) synchrotron XRD and (e) neutron powder diffraction. (b, d, f) show corresponding expansions of the 'superstructure' peaks, highlighting the differences observed in resolution between the three techniques.

2.3 Rietveld Analysis[136]

The use of powder diffraction techniques in the determination of crystal structures is extremely challenging. However, it is one of the most common uses of powder data and the procedure adopted to complete such structural investigations is that of the Rietveld method, originally proposed by Hugo Rietveld.[137-139] To use this particular technique some prior knowledge of the structural model is required, enabling the refinement process to be simplified considerably.

Polycrystalline samples routinely generate a considerable number of peaks within any powder diffraction pattern, the majority of which occur at low d-spacings. Owing to the quantity of peaks generated they often overlap with one another making it virtually impossible to accurately identify and fit each individual peak. The Rietveld method provides an accurate solution to such a problem by attempting to fit a structural model to the pattern as a whole, thereby avoiding the problem of indexing and fitting each peak separately. The method adopted within this particular type of refinement is a least squares minimisation, in which model parameters for a theoretical structure are refined until a reasonable degree of fit is achieved with the experimental powder pattern. The theoretical model utilised is commonly obtained from the Inorganic Crystal Structure Database.[140] Structural refinement involves the adjustment of factors such as the background coefficients, detector zero point, instrumental parameters, lattice parameters, profile coefficients, isotropic and anisotropic thermal factors and atomic positional coordinates. During any structural refinement the residual, S_y, (as detailed by Equation 2.4, where the parameter y_{oi} corresponds to the observed intensity and y_{ci} is the calculated intensity) is minimised using a least squares method.

$$S_y = \sum_i \frac{1}{y_i}(y_{oi} - y_{ci})^2 \tag{2.4}$$

When S_y is a minimum the 'best' possible fit between the calculated and experimental patterns is achieved. However, this does not take into consideration the chemical accuracy of the model. To determine the quality of fit obtained R-factors such as the R-profile, R_p, and R-weighted profile, R_{wp}, are utilised, given by Equations 2.5 and 2.6 respectively. Profile weighting is hugely important within the Rietveld method as it attempts to fit all peaks in the pattern equally, with no preference given to peaks of higher intensity. Therefore, to prevent peaks of greater intensity dominating any refinement the parameter $1/y_i$ is used. This enables peaks of weaker intensity to be fitted with the same preference as peaks exhibiting the greatest intensity in any diffraction pattern.

$$R_p = \frac{\sum_i |y_{oi} - y_{ci}|}{\sum_i y_{oi}} \tag{2.5}$$

$$R_{wp} = \left[\frac{\sum_i \frac{1}{y_i}(y_{oi} - y_{ci})}{\sum_i \frac{1}{y_i}(y_{oi})^2} \right]^{\frac{1}{2}} \tag{2.6}$$

$$\chi^2 = \frac{\sum_i \frac{1}{y_i}(y_{oi} - y_{ci})^2}{N - P + C} \tag{2.7}$$

An additional parameter used to establish the quality of a fit is given by χ^2, Equation 2.7, where N is the number of observations, P is the number of refined parameters and C is the number of constraints. This parameter is particularly useful as it indicates the 'goodness' of fit. When χ^2 is equal to one this is indicative of a perfect fit. Therefore, to determine the quality of Rietveld fit the closeness of χ^2 to one is measured. All structural refinements were completed using GSAS.

2.4 Basic Principles of NMR

Nuclear Magnetic Resonance (NMR) is a hugely powerful technique and is widely used in the study and characterisation of complex structures. Almost all stable elements in the periodic table possess active nuclei and therefore NMR is routinely utilised, both in solution and in the solid state.

2.4.1 Nuclear Magnetism

Nuclei possess an intrinsic spin angular momentum, **I**, with a corresponding spin quantum number, I, related to the composition of the nucleus. I may be zero or any positive integer or half-integer value. The magnitude of the spin angular momentum is given by

$$|\mathbf{I}| = \hbar\left[\mathrm{I}(\mathrm{I}+1)\right]^{1/2} \quad . \tag{2.8}$$

The projection of this angular momentum vector onto the z-axis is given by $I_z = m_I\hbar$, where m_I is the magnetic quantum number with values ranging from −I to +I, resulting in 2I + 1 states degenerate in energy. The circulating charge creates a magnetic dipole moment, **μ**, given by

$$\boldsymbol{\mu} = \gamma\mathbf{I} \quad , \tag{2.9}$$

where γ is the gyromagnetic ratio of the nucleus. The orientation of **μ** is either parallel (if γ is positive) or anti-parallel (if γ is negative) to **I**. In the absence of an external magnetic field all 2I + 1 orientations of I are degenerate in energy and orientated at random. Upon application of a strong magnetic field, B_0, the axis of quantization is defined and the nuclear spins align themselves relative to B_0. Upon doing so the degeneracy of the 2I + 1 is lifted, as shown in Figure 2.11 for spin I = 1/2, 1 and 3/2 nuclei. When the field is applied along the z-axis the energy is given by

$$E = -\mu_Z B_0 \quad , \tag{2.10}$$

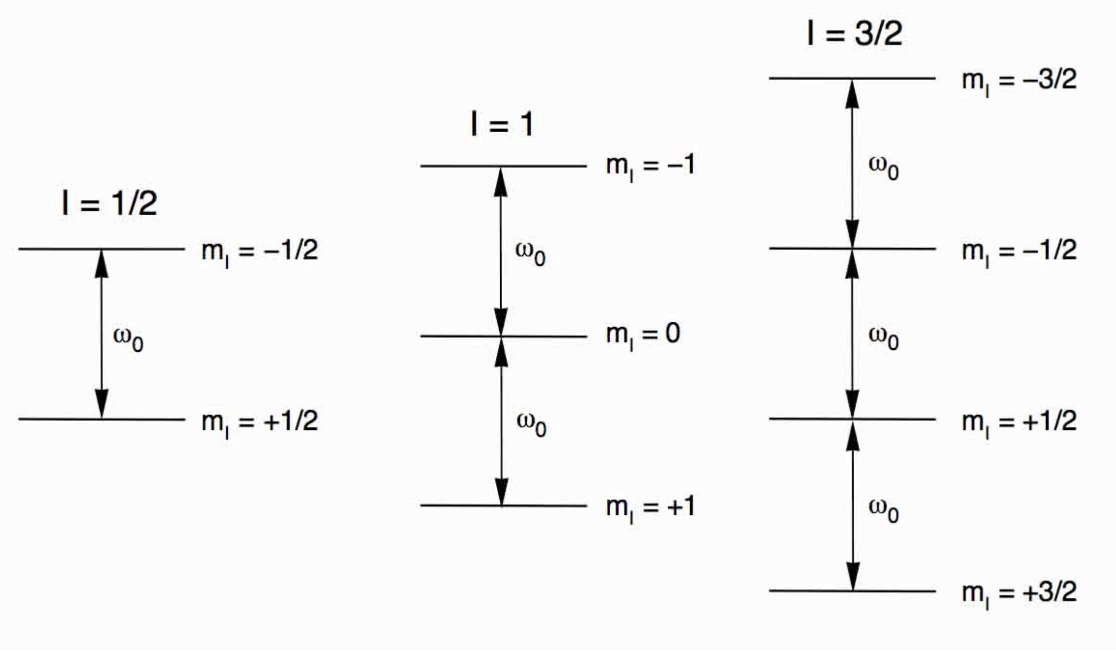

Figure 2.11: The effect of the Zeeman interaction upon the nuclear energy levels for spin (a) I = 1/2, (b) I = 1 and (c) I = 3/2 nuclei.

where μ_Z is the projection of the magnetic dipole moment onto the z-axis and B_0 is the applied magnetic field in this direction. This is known as the Zeeman interaction. In a macroscopic sample at thermal equilibrium there will be a very slight excess of spins in the lower energy level which gives rise to a net or bulk magnetization vector, $\mathbf{M_0}$. In NMR the spectroscopic selection rule for an observable transition is $\Delta m_I = \pm 1$ and the frequency of any such transition is therefore given by

$$\omega_0 = \frac{\Delta E}{\hbar} = -\gamma B_0 \quad , \tag{2.11}$$

where ω_0 is the Larmor frequency with units of rad s^{-1}.

2.4.2 The Vector Model

Although spin must be treated quantum mechanically, it is possible to treat the ensemble of spins in a macroscopic sample in a classical way. The 'vector model' was first proposed by Bloch and is now routinely utilised as a geometrical interpretation of the basic principles involved in NMR.[141] Modern spectrometers commonly employ pulsed NMR methods in which short pulses of intense linearly oscillating radiofrequency (rf) radiation is applied to a sample. The frequency of this radiation, ω_{rf}, is close to the resonance frequency, ω_0. The applied pulse, with strength B_1 and duration τ_p, interacts with the nuclear spins in a sample, exciting all resonances simultaneously, thereby affecting the orientation of the bulk magnetization vector, $\mathbf{M_0}$, as shown in Figure 2.12. Pulsed NMR methods are highly advantageous over previous continuous wave (CW) methods as the experiment can be repeated more rapidly which, in turn, improves signal-to-noise which can be limiting in NMR spectroscopy owing to the low Boltzmann population differences. The interaction of a pulse with a sample is extremely difficult to visualise in the laboratory frame and so a 'rotating frame' is utilised. This is a frame of reference which itself is rotating about the z-axis at a frequency ω_{rf}. In this frame, the bulk magnetization vector precesses around the magnetic field at a frequency Ω, with an effective magnetic field, B_0^{eff}, along the z-axis.

$$\Omega = \omega_0 - \omega_{rf} \tag{2.12}$$

$$B_0^{eff} = \frac{\Omega}{\gamma} = -B_0 - \frac{\omega_{rf}}{\gamma} \quad . \tag{2.13}$$

In the rotating frame a pulse can be described as a static field, B_1, applied perpendicular to B_0. If applied along x the bulk magnetization vector, $\mathbf{M_0}$, nutates into the xy plane. Once the pulse is removed $\mathbf{M_0}$ undergoes free precession at a frequency $\Omega = \omega_0 - \omega_{rf}$, as shown in Figure 2.12. The angle through which the magnetization nutates during the pulse is defined as the 'flip angle', β,

$$\beta = \omega_1 \tau_p \quad , \tag{2.14}$$

where $\omega_1 = -\gamma B_1$ and τ_p is the duration of the pulse. Flip angles commonly utilised in NMR experiments are $\beta = 90°$, where the magnetization is placed in the xy plane, and $\beta = 180°$, where the magnetization is inverted to lie along the −z-axis.

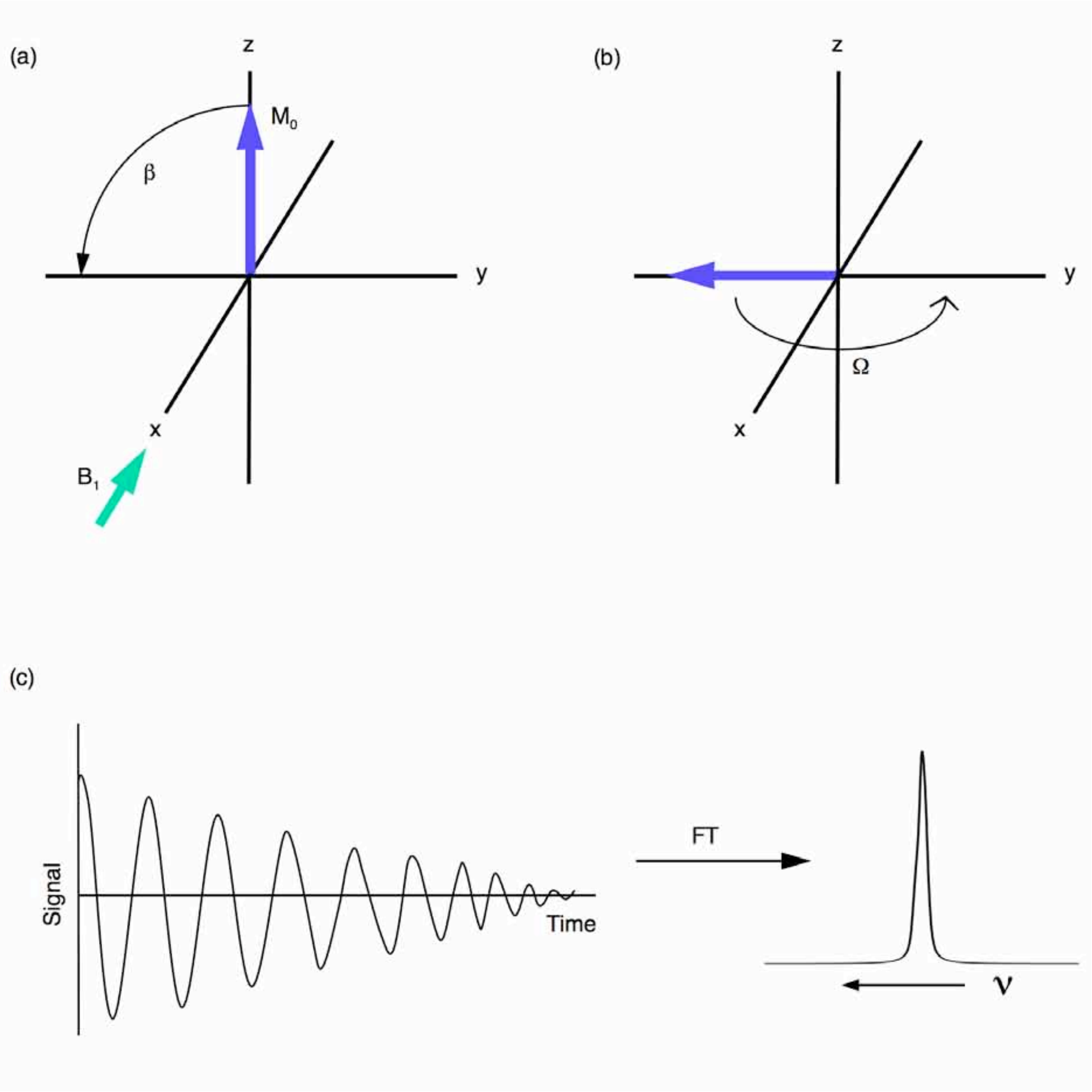

Figure 2.12: (a) Vector model representation of the effect of a pulse applied along the x axis of the rotating frame on the bulk magnetization vector M_0. (b) After nutation into the yx plane the vector undergoes free precession at frequency Ω. (c) A schematic representation of an FID and corresponding spectrum post Fourier transformation and phasing.

2.4.3 Relaxation

Various relaxation effects, returning the system to equilibrium, dampen the precession of the magnetization around the z-axis. Transverse or spin-spin relaxation, characterised by a time constant T_2, is defined as the loss of magnetization from the xy plane and occurs through interaction between the spins. Longitudinal or spin-lattice relaxation, with time constant T_1, describes the return of the z component of the magnetization to equilibrium. Values of T_1 are sample dependent and, in some cases, are extremely long. For example, in solids ^{89}Y (I = 1/2) has typical T_1 values on the order of hundreds to thousands of seconds. As a result, this determines the rate at which experiments can be repeated. The damped precession of $\mathbf{M}_0$ is known as the free induction decay (FID) and is the signal detected when an induced voltage is detected in the receiver coil. The FID is a time-domain signal and to convert to a frequency-based spectrum Fourier Transformation (FT) is required.[142,143]

2.4.4 Fourier Transformation

The FID obtained is the sum of many different oscillating waves, each with a different frequency, amplitude and phase. This signal is commonly detected using a technique known as quadrature detection[144] which enables simultaneous measurement of both the x and y components of the FID. For each resonance observed in the spectrum two signals are acquired, one a cosine and the other a sine function of the offset frequency Ω, decaying at a rate of $1/T_2$ (owing to transverse relaxation effects). These signals are the real and imaginary parts of a complex time-domain signal, s(t), given by[145,146]

$$s(t) = \left[\cos\Omega t + i\sin\Omega t\right]\exp(-t/T_2) \tag{2.15}$$

$$s(t) = \exp(i\Omega t)\exp(-t/T_2) \quad t \geq 0 \tag{2.16}$$

$$s(t) = 0 \quad t < 0 \ . \tag{2.17}$$

The signal is then converted to a frequency-domain spectrum $S(\omega)$ by Fourier transformation

$$S(\omega) = \int_0^\infty s(t)e^{-i\omega t}dt \ . \tag{2.18}$$

The frequency-domain function, S(ω), is composed of both real and imaginary parts, given by Equations 2.20 and 2.21, respectively. The real part corresponds to an absorptive Lorentzian lineshape and the imaginary part the corresponding dispersive Lorentzian.

$$S(\omega) = A(\Delta\omega) - iD(\Delta\omega) \tag{2.19}$$

$$A(\Delta\omega) = \frac{1/T_2}{(1/T_2)^2 + (\Delta\omega)^2} \tag{2.20}$$

$$D(\Delta\omega) = \frac{\Delta\omega}{(1/T_2)^2 + (\Delta\omega)^2} \quad . \tag{2.21}$$

Spectral lineshapes, in reality, are neither purely real or imaginary. They instead possess an arbitrary phase composed of both the real and imaginary parts and to obtain absorption-phase lineshapes a process known as 'phasing' is required post Fourier transformation. This is achieved by taking linear combinations of the real and imaginary parts of the spectrum until the desired lineshape is achieved. A schematic representation of an FID and corresponding spectrum, post Fourier transformation and phasing, are shown in Figure 2.12(c).

2.4.5 Density Operator Formalism

Macroscopic samples are known to contain large numbers of nuclear spin systems, each of which may be described quantum mechanically by a wavefunction, Ψ(t). Each wavefunction may be expanded as a linear combination of the elements of an orthogonal basis set $|i\rangle$:

$$\Psi(t) = \sum_i c_i(t)|i\rangle \quad , \tag{2.22}$$

where $c_i(t)$ are time-dependent coefficients. A more compact approach involves using a density operator, σ(t), whose matrix representation is termed the density matrix.[147] The elements of this matrix, $\sigma_{i,j}(t)$, are the products of the expansion coefficients of the wavefunction Ψ(t), i.e.,

$$\sigma_{i,j}(t) = \langle i|\sigma(t)|j\rangle$$

$$= \overline{c_i(t)c_j(t)^*} \quad , \qquad (2.23)$$

where the overbar and * denote an ensemble average and complex conjugate, respectively. The density operator formalism,[147] when compared with the classical vector model description, is a more rigorous and compact quantum mechanical approach to describe the ensemble of spins during the course of an NMR experiment. For a spin $I > 1/2$ nucleus quantum mechanical behaviour is a more convenient description.

2.4.6 Coherence

Consider an ensemble of non-interacting spins. Each spin, with wavefunction $\Psi(t)$, can be described as a superposition of the states $|\alpha\rangle$ and $|\beta\rangle$. The contributions to these states, described by coefficients $c_\alpha(t)$ and $c_\beta(t)$, possess both a time and phase dependence. At $t = 0$, the complex superposition coefficients $c_\alpha(t)$ and $c_\beta(t)$ have phases ϕ_α and ϕ_β, respectively and $\Psi(t)$ is given by,

$$\Psi(t) = c_\alpha(t)e^{i\phi_\alpha}|\alpha\rangle + c_\beta(t)e^{i\phi_\beta}|\beta\rangle \quad . \qquad (2.24)$$

The matrix representation of the density operator, $\sigma(t)$, for the system therefore takes the following form

$$\sigma(t) = \begin{pmatrix} c_\alpha c_\alpha^* & c_\alpha c_\beta^* e^{i(\phi_\alpha - \phi_\beta)} \\ c_\beta c_\alpha^* e^{i(\phi_\beta - \phi_\alpha)} & c_\beta c_\beta^* \end{pmatrix} \quad . \qquad (2.25)$$

The diagonal elements $c_\alpha c_\alpha^*$ and $c_\beta c_\beta^*$ are equal to $|c_\alpha^2|$ and $|c_\beta^2|$ respectively, thus, they refer to the populations of the $|\alpha\rangle$ and $|\beta\rangle$ spin states. If the relative phases of each of the spins are the same then the off-diagonal elements $c_\alpha c_\beta^* e^{i(\phi_\alpha - \phi_\beta)}$ and $c_\beta c_\alpha^* e^{i(\phi_\beta - \phi_\alpha)}$ will have non-zero magnitude. In such cases there is said to be phase coherence between the spins. The converse is also true, if each spin exhibits a random phase difference, then the off-diagonal elements in the density matrix will, on average, sum to zero and in such cases no coherence exists in the ensemble. Consider the density matrix for a single spin I = 3/2 nucleus where the chosen basis set is the set of eigenstates of the Zeeman Hamiltonian, i.e., m_I = 3/2, 1/2, −1/2, −3/2. The density matrix is of the form

$$\sigma(t) = \begin{pmatrix} \sigma_{1,1}(t) & \sigma_{1,2}(t) & \sigma_{1,3}(t) & \sigma_{1,4}(t) \\ \sigma_{2,1}(t) & \sigma_{2,2}(t) & \sigma_{2,3}(t) & \sigma_{2,4}(t) \\ \sigma_{3,1}(t) & \sigma_{3,2}(t) & \sigma_{3,3}(t) & \sigma_{3,4}(t) \\ \sigma_{4,1}(t) & \sigma_{4,2}(t) & \sigma_{4,3}(t) & \sigma_{4,4}(t) \end{pmatrix}, \qquad (2.26)$$

where the elements $\sigma_{i,i\pm1}(t)$ represent coherences with $\Delta m_I = \pm1$, commonly denoted as coherence order $p = \pm1$. It is these coherences which are directly observable in an NMR experiment. However, by convention only $p = -1$ coherences are detected when quadrature detection[144] is utilised. The elements $\sigma_{i,i\pm2}(t)$ and $\sigma_{i,i\pm3}(t)$ represent multiple-quantum coherences, i.e., those with coherence orders of $p = \pm2$ and ±3 respectively. Although these are not directly observable they are utilised in many important NMR experiments.

2.5 NMR Interactions

There are many important interactions in NMR, the most dominant of which is usually the Zeeman interaction. These interactions, including the Zeeman interaction, can be described by a Hamiltonian, H, given in general form by,

$$H = I \cdot R \cdot X \qquad (2.27)$$

$$H = (I_x \, I_y \, I_z) \begin{pmatrix} R_{xx} & R_{xy} & R_{xz} \\ R_{yx} & R_{yy} & R_{yz} \\ R_{zx} & R_{zy} & R_{zz} \end{pmatrix} \begin{pmatrix} X_x \\ X_y \\ X_z \end{pmatrix}, \qquad (2.28)$$

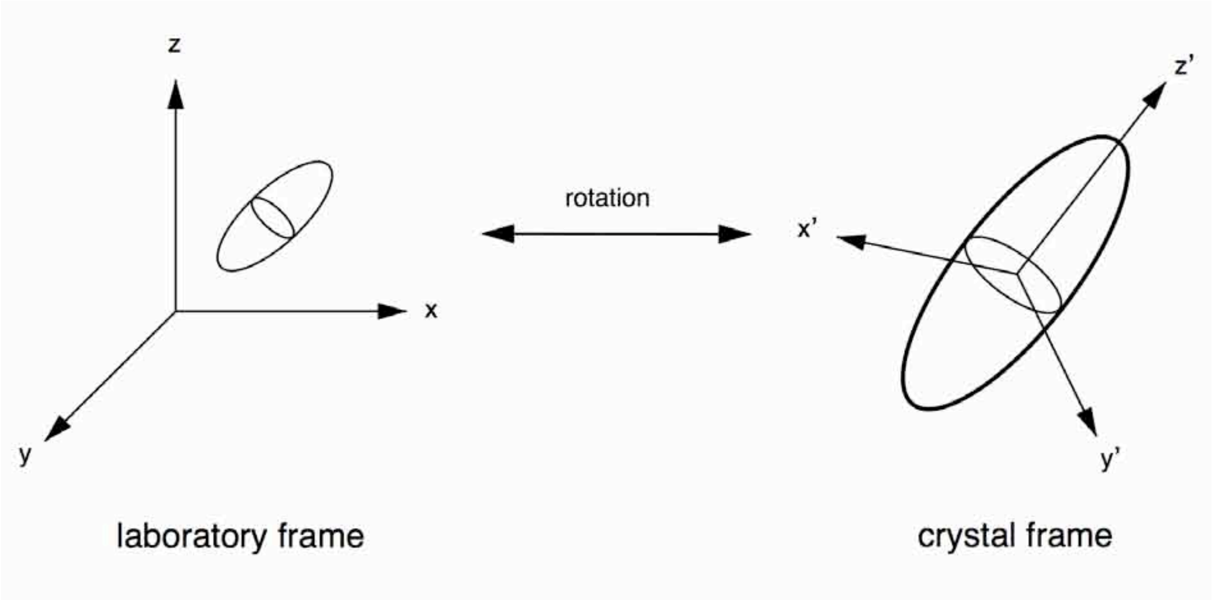

Figure 2.13: Schematic representation of the transformation of a tensor between the laboratory frame and the PAS.

where I is the spin angular momentum operator, R is a second-rank Cartesian tensor defining the interaction and X represents either a second spin operator or a magnetic field. Hence the total Hamiltonian, H, for any nucleus may be expressed as the sum of the individual Hamiltonian contributions for the Zeeman interaction, H_Z, the applied radiofrequency pulse, H_{rf}, dipolar, H_D, chemical shielding, H_{CS}, scalar, H_J, and quadrupolar, H_Q, interactions given by,

$$H = H_Z + H_{rf} + H_D + H_{CS} + H_J + H_Q \quad . \tag{2.29}$$

It is convenient to describe an interaction within a frame, defined by the magnitude and shape of the interaction itself. This is known as the Principal Axis System, or PAS, a frame where the second-rank tensor defining the interaction is defined such that all off-diagonal elements are zero. A schematic representation of the PAS is shown in Figure 2.13. To convert between the laboratory frame and the PAS a rotation is required, thereby highlighting the angular dependence of many of the interactions.

2.5.1 Chemical Shift Anisotropy (CSA)

The field experienced by a nuclear spin, in reality, is not the applied magnetic field, B_0. In a magnetic field, the electrons around a nucleus circulate and, in turn, generate a small magnetic field, B′, which either opposes or augments the applied field. Consequently, this changes the field experienced by the nucleus and perturbs the Larmor frequency

$$\omega' = -\gamma B_0(1-\sigma) \ , \tag{2.30}$$

where σ is a shielding parameter. In reality, the shielding is orientation dependent and is described by a second-rank tensor, $\boldsymbol{\sigma}$. The Hamiltonian describing the chemical shielding, H_{CS}, is given by

$$H_{CS} = \mathbf{I} \cdot \boldsymbol{\sigma} \cdot \gamma \mathbf{B_0} \ . \tag{2.31}$$

When B_0 is defined to be along the z-axis the secular approximation may be applied and the Hamiltonian becomes

$$H_{CS} = \gamma B_0 \sigma_{zz} I_z \ . \tag{2.32}$$

More usually the shielding tensor is expressed in the PAS. In this frame the tensor can be represented by an ellipsoid, as illustrated in Figure 2.14, and is defined by three parameters, the isotropic shielding, σ_{iso}, the shielding anisotropy, $\Delta\sigma_{CS}$, and the asymmetry, η_{CS}, given by

$$\sigma_{iso} = \frac{1}{3}(\sigma_{11} + \sigma_{22} + \sigma_{33}) \tag{2.33}$$

$$\Delta\sigma_{CS} = (\sigma_{33} - \sigma_{iso}) \tag{2.34}$$

$$\eta_{CS} = \frac{(\sigma_{11} - \sigma_{22})}{(\sigma_{33} - \sigma_{iso})} \ , \ 0 < \eta_{CS} < 1 \tag{2.35}$$

where σ_{11}, σ_{22} and σ_{33} are the three principal components of the tensor. To convert from the PAS to the laboratory frame a rotation is necessary,

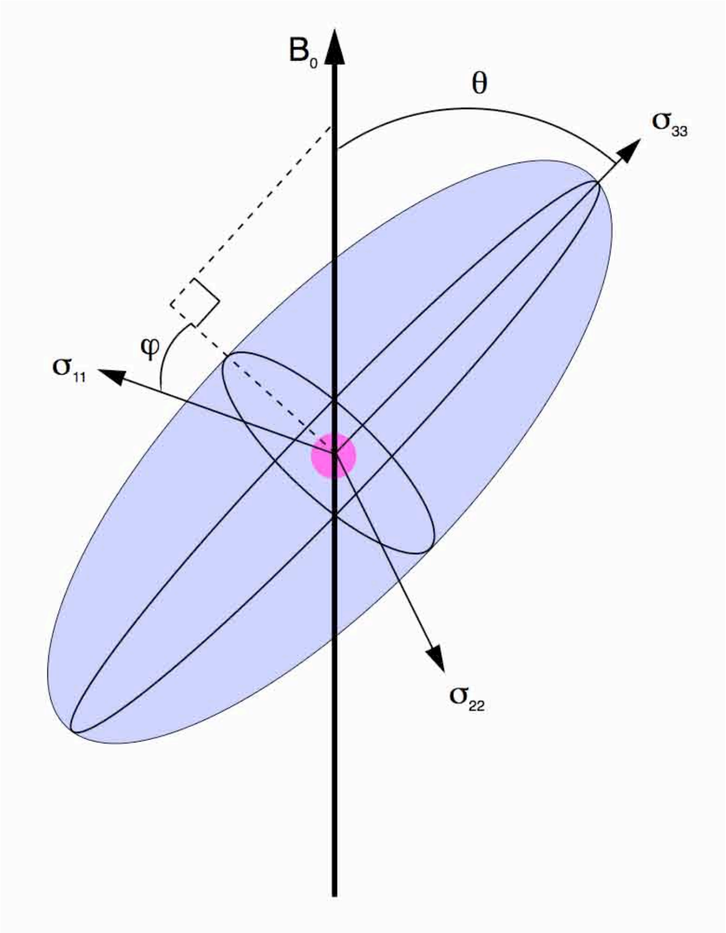

Figure 2.14: A schematic representation of the shielding tensor in the PAS, where σ_{11}, σ_{22} and σ_{33} are the three principal components of the tensor. The angles θ and ϕ are the angles defining the orientation of the tensor relative to the magnetic field B_0.

revealing the angular dependence of the chemical shielding. This is highlighted in the σ_{zz} component[148] of the shielding tensor, given by

$$\sigma_{zz} = \sigma_{iso} + \frac{\Delta\sigma_{CS}}{2}\left[(3\cos^2\theta - 1) + \eta_{CS}(\sin^2\theta\cos 2\varphi)\right] \ . \qquad (2.36)$$

For different orientations of the shielding tensor PAS, a different chemical shift is observed. In solution the chemical shielding is averaged solely to its isotropic value, shown in Equation 2.33, by rapid molecular tumbling and, as a result, lineshapes are inherently sharp and narrow. Solids, however, are often densely packed and therefore do not usually exhibit such molecular motion, hence they display the full extent of the CSA, producing extremely broad spectra. Powders are composed of millions of tiny crystallites, each with a different orientation with respect to B_0, hence

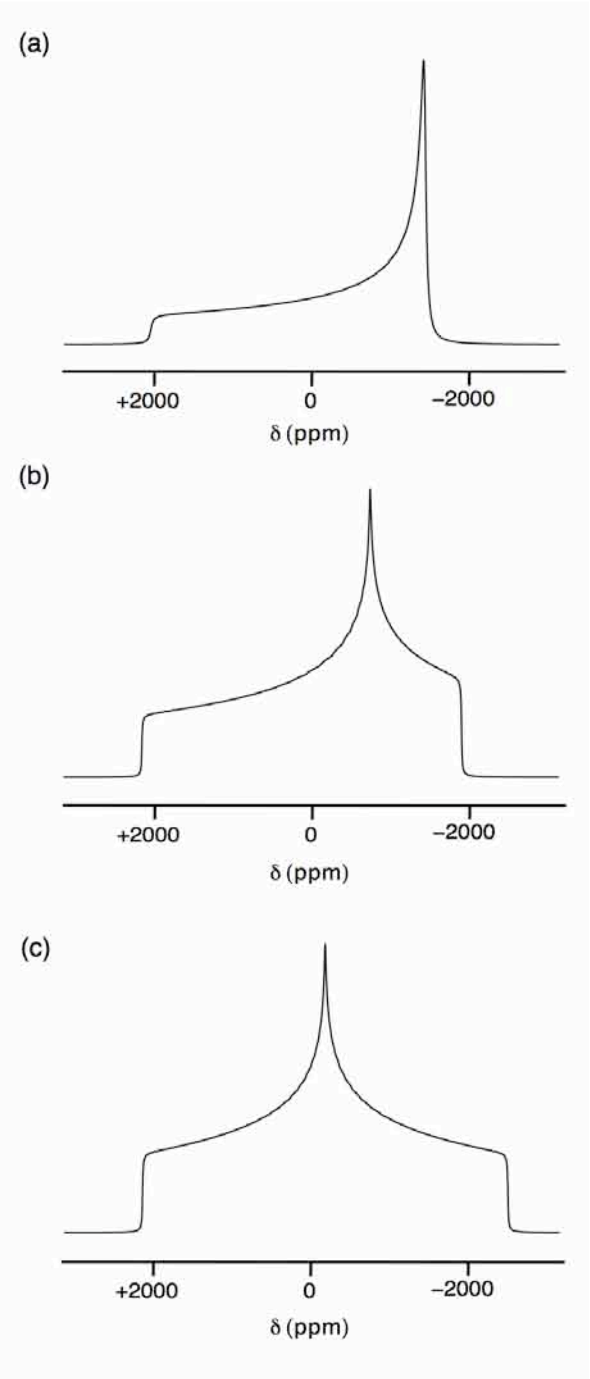

Figure 2.15: Simulated CSA lineshapes for a spin I = 1/2 nucleus with $\Delta\sigma_{CS}$ = 2000 ppm and asymmetry, η_{CS}, (a) 0, (b) 0.5 and (c) 1.

shifts from all possible orientations will be observed resulting in broad ‘powder-pattern’ lineshapes. Powdered CSA lineshapes simulated with η_{CS} = 0, 0.5 and 1 are shown in Figures 2.15(a), (b) and (c), respectively. The lineshapes simulated highlight how the shape of the powder-pattern line observed varies depending upon η_{CS}. Specific details are given in the figure caption.

The shielding is an inconvenient measure of the chemical shift and therefore a deshielding parameter, δ, is used, defined by

$$\delta = 10^{6}\left(\frac{\omega - \omega_{\mathrm{ref}}}{\omega_{\mathrm{ref}}}\right) \tag{2.37}$$

where ω and ω_{ref} are the resonance frequencies of the nucleus of interest and a standard or reference.[149] The chemical shift of a nucleus is a property that reflects the environment the nucleus experiences. It therefore provides valuable information regarding the electron distribution around the nucleus. The chemical shift is dimensionless and quoted in parts per million (ppm).

2.5.2 Dipolar Coupling

The nuclear magnetic dipole moments of nuclei produce small localised magnetic fields that, in turn, interact with dipole moments of nearby nuclei. This through space interaction, referred to as dipolar coupling, is orientationally dependent, as the effect of the localised field from one spin to another depends upon the relative position of the two spins. This interaction is averaged to zero in solution by rapid molecular tumbling. In solids, however, the dipolar interaction produces an associated broadening of the observed spectrum. In the laboratory frame the dipolar Hamiltonian, H_D, between two spins I and S contains many orientationally dependent terms, and therefore a truncated form is usually used. Hence, for two homonuclear spins (I = S), separated by an internuclear distance r_{IS}, a truncated version of the dipolar Hamiltonian after the secular approximation is given by[150]

$$H_{D}^{IS} = \omega_{D}\left[3I_{z}S_{z} - \mathbf{I}\,.\,\mathbf{S}\right] , \tag{2.38}$$

where ω_D is the dipolar splitting parameter, given by

$$\omega_{D} = \omega_{D}^{PAS}\left(\frac{3\cos^{2}\theta - 1}{2}\right) \tag{2.39}$$

with[151,152]

$$\omega_D^{PAS} = \frac{-\mu_0}{4\pi}\frac{\gamma_I\gamma_S\hbar}{r_{IS}^3} \tag{2.40}$$

where r_{IS} is the internuclear distance between two spins I and S. It must be noted that the dipolar tensor is always axially symmetric, with $\eta_D = 0$. For two heteronuclear spins ($I \neq S$) further truncation of the Hamiltonian is required, reducing it to[153]

$$H_D = \omega_D\left[2I_zS_z\right] \; . \tag{2.41}$$

Consider two isolated heteronuclear spin 1/2 nuclei I and S. A schematic representation of the energy levels for such a system is given in Figure 2.16(a). The effect of the heteronuclear dipolar coupling on the spectrum is to split each single transition into a doublet separated by $2\omega_D$, also shown in Figure 2.16(a). The dipolar interaction, in a similar manner to the CSA, is orientationally dependent, therefore the dipolar splitting observed depends upon the angle between the internuclear vector and the magnetic field. The variation of this angle produces an associated effect on the dipolar splitting also observed. In powdered or polycrystalline samples an average over all possible orientations is observed, resulting in a 'Pake doublet' lineshape, an example of which is shown in Figure 2.16(a). For two homonuclear spins I = S only two possible transitions are allowed, these are shown in Figure 2.16(b). The effect of homonuclear dipolar coupling on a spectrum is to split the single transition into a doublet, separated by $3\omega_D$, as shown in Figure 2.16(b). Powdered samples therefore result in a Pake doublet lineshape with a maximum splitting of $3\omega_D$, also shown in Figure 2.16(b).

In reality it is extremely rare to find two isolated spins, and hence there are many dipolar couplings involved between numerous spins. As a direct consequence of these interactions lineshapes typically exhibit an associated Gaussian broadening. Spectral lineshapes displaying different degrees of Gaussian broadening simulated to highlight the effect of such broadening on the observed lineshapes are shown in Figure 2.17. The

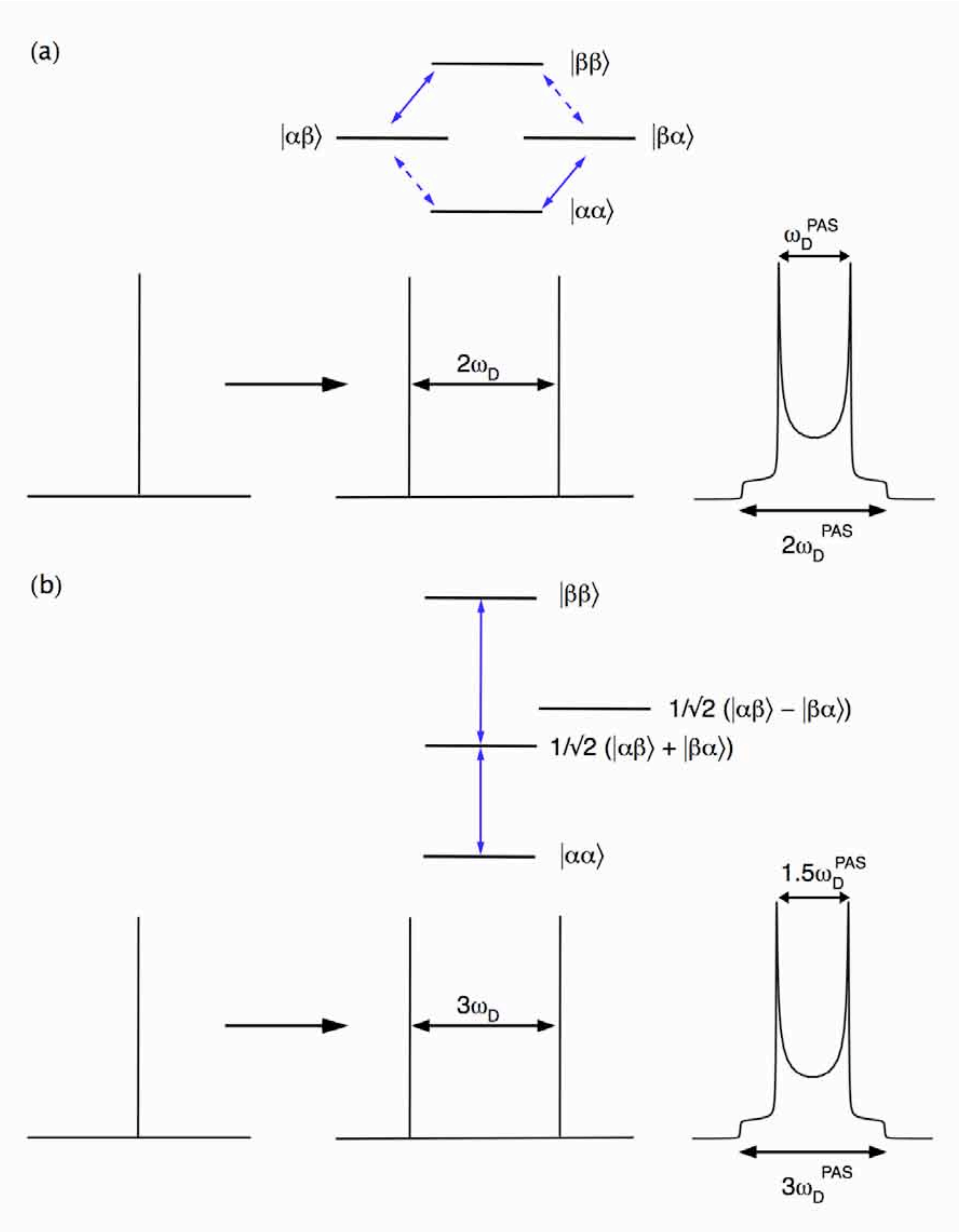

Figure 2.16: **Schematic energy level diagrams for (a) two heteronuclear dipolar coupled I ≠ S = 1/2 nuclei and (b) two homonuclear dipolar coupled I = 1/2 nuclei. In each case, the single transition is split into a doublet by $2\omega_D$ and $3\omega_D$ in (a) and (b), respectively for a single orientation. For a powdered sample an average over all possible orientations is observed, resulting in a Pake doublet powder pattern lineshape.**

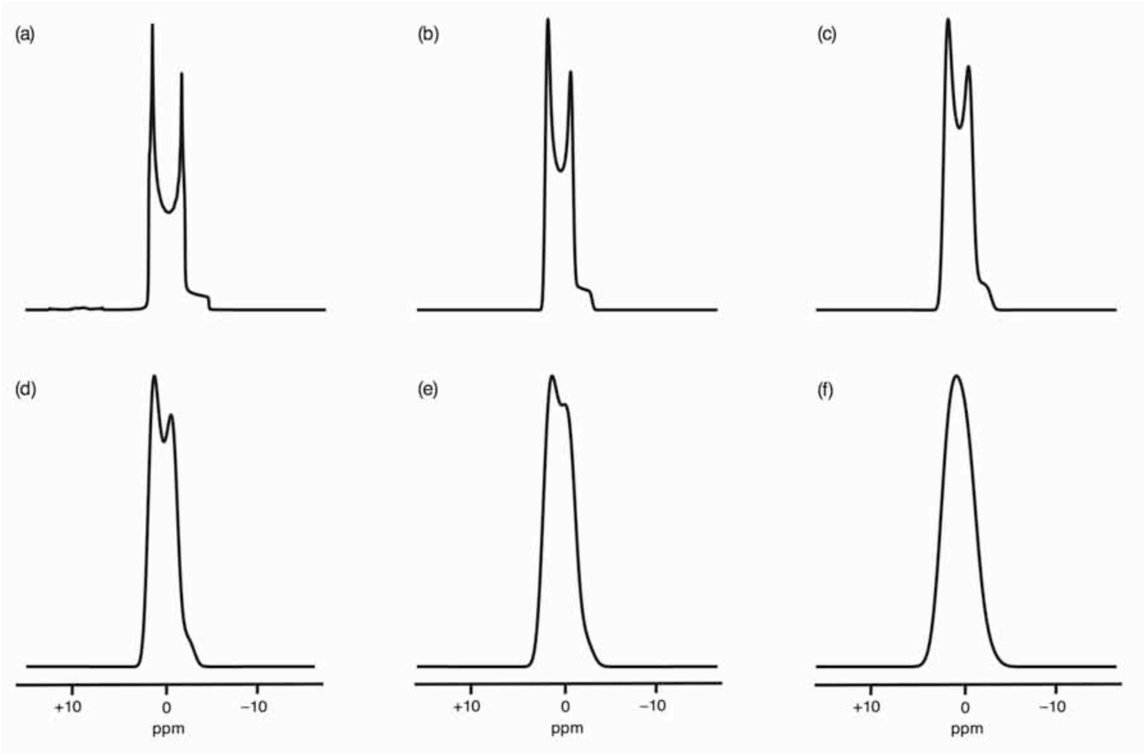

Figure 2.17: Second-order broadened quadrupolar (I = 3/2) lineshapes (see section 2.8 regarding quadrupolar interactions) simulated with C_Q = 2 MHz, $\eta_Q = 0$, $\omega_0/2\pi$ = 158.75 MHz and linebroadening of (a) 100, (b) 200, (c) 300, (d) 400, (e) 500 and (f) 600 Hz.

broadening exhibited can often lead to the loss of distinct features in the lineshape. For example in Figure 2.17(a) a distinct set of 'horns' are displayed which begin to diminish (Figures (b-e)) as the extent of Gaussian broadening is increased. The distinct features are then fully removed when the broadening is dominant, as illustrated in Figure 2.17(f). This type of broadening often hinders the extraction of any structurally relevant information. Hence, a method for removing such sources of broadening is highly desirable.

2.5.3 Scalar Couplings

In solids the scalar or J-coupling is usually the smallest of the contributions to the total Hamiltonian. In solution, high-resolution spectra commonly exhibit complex splitting patterns as a direct result of scalar couplings. For two J-coupled spins I and S the Hamiltonian[154] is given by

$$H_J = 2\pi\,\mathbf{J}\,.\,\mathbf{I}\,.\,\mathbf{S}\;, \tag{2.42}$$

where **J** is a second-rank tensor defining the interaction. When B_0 is defined to be along the z-axis the secular approximation may be applied and the Hamiltonian becomes

$$H_J = 2\pi J I_z S_z\;. \tag{2.43}$$

where J is the isotropic J-coupling or scalar coupling and is equal to the average of the diagonal elements of the J-coupling tensor. Scalar couplings are a through-bond interaction mediated by the electrons within the chemical bond. J-couplings are often present in solid-state NMR spectra; however, they are commonly only on the order of a few tens of hertz, and are therefore usually dominated by larger anisotropic interactions such as CSA and dipolar couplings. Despite this, the coupling is often utilised for the successful transfer of magnetization from one spin to another.

2.6 Magic-Angle Spinning

Magic-angle spinning (MAS) is a method for suppressing anisotropic interactions such as CSA and dipolar couplings by the introduction of artificial motion upon a solid.[155-157] The technique involves rapid rotation of the sample about an axis orientated at an angle of 54.736° relative to the external magnetic field, B_0, as illustrated in Figure 2.18(a).

Both CSA and dipolar interactions possess an orientation dependence proportional to $3\cos^2\theta - 1$, as shown in Equations 2.36 and 2.39 respectively. When $\theta = 54.736°$ the interaction is removed. However, for a powdered solid all crystallites must be orientated at θ simultaneously to remove the interaction. This is, in reality, not feasible and a method capable of imposing an average orientation on the whole sample is required. Magic-angle spinning achieves this by fast rotation of the sample around an angle where $3\cos^2\theta - 1$ is reduced to zero. MAS is

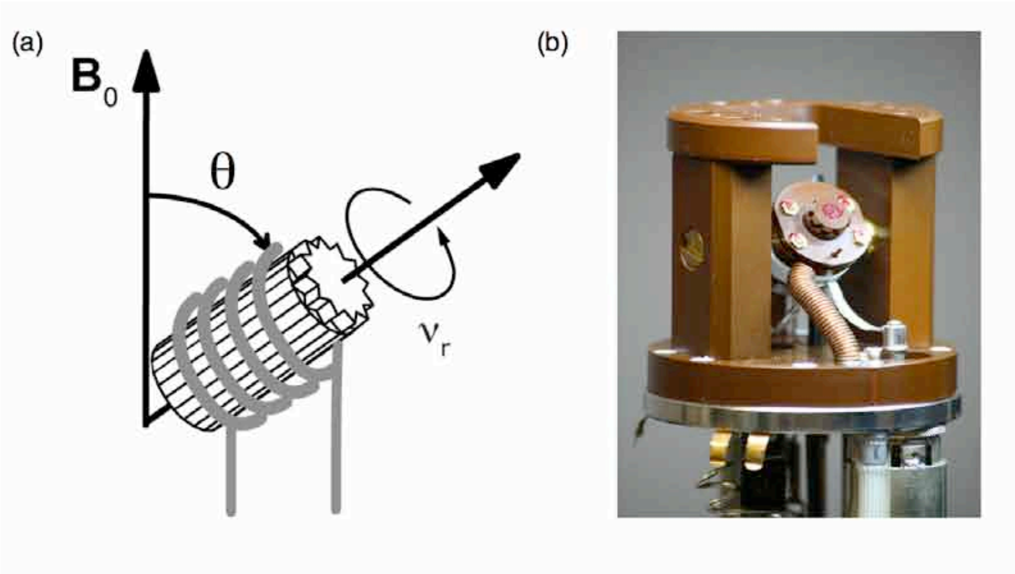

Figure 2.18: (a) Schematic representation of a rotor at the magic angle of θ = 54.736° and (b) picture of an MAS probe showing the stator block containing the coil inclined at the magic angle.

therefore a successful method for averaging many of the anisotropic interactions within solid-state NMR to their isotropic value. To successfully suppress the interactions the spinning rate must usually be equal to or greater than the anisotropy of the interaction being removed. MAS rates of up to 30 kHz are routinely possible, and with considerable advances in probe design, faster MAS rates of up to 65 kHz are now feasible commercially. If the spinning rate is insufficient to suppress the interaction the lineshape breaks up into an envelope of spinning sidebands separated from the centreband by the spinning speed, as shown in Figure 2.19. As the rate of spinning changes the centreband position remains unchanged. Broad sideband patterns severely hinder the extraction of important structural data, and hence fast spinning rates are desirable. Both CSA and several heteronuclear dipolar couplings are typically of the order of a few kilohertz, and hence they can be averaged relatively easily by MAS.[158] In contrast, homonuclear dipolar couplings can only be removed when very fast MAS rates are utilised as the spinning rate needs to be greater than the homonuclear dipolar coupling linewidth, e.g., ^{1}H – ^{1}H dipolar couplings can often be 80 - 100 kHz. It is challenging to routinely use such speeds and therefore alternative methods capable of removing homonuclear dipolar couplings are more

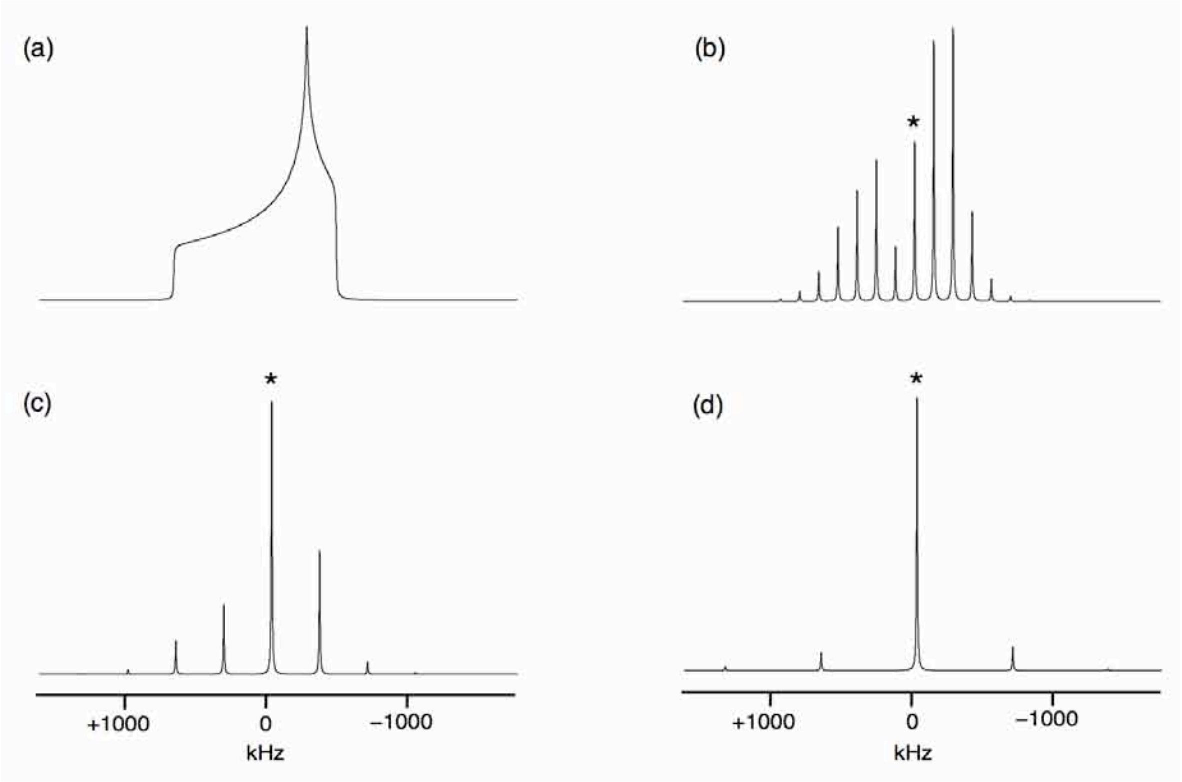

Figure 2.19: Simulated I = 1/2 lineshapes with $\Delta\sigma_{CS}$ = 300 ppm, η_{CS} = 0.3 at MAS rates of (a) 0 kHz, (b) 2 kHz, (c) 5 kHz and (d) 10 kHz. The isotopic centreband is marked with *.

commonly used, such as decoupling (see later section). Magic-angle spinning significantly improves the resolution of a spectrum, thereby making it feasible to accurately determine the number of distinct sites in addition to their respective chemical shifts and relative populations.

2.7 Dipolar Decoupling

At moderate MAS frequencies the heteronuclear dipolar coupling interaction is not fully removed, resulting in large homogeneous broadenings. Hence, very fast MAS rates are required to successfully remove the effects of such couplings. An alternative method for removing the dipolar couplings is a technique known as heteronuclear dipolar decoupling.[159,160] This is a hugely powerful method involving continuous irradiation of the spin not under observation during acquisition of the FID. Decoupling can be applied either static or under MAS, and when utilised under MAS further narrowing of the lineshape is commonly

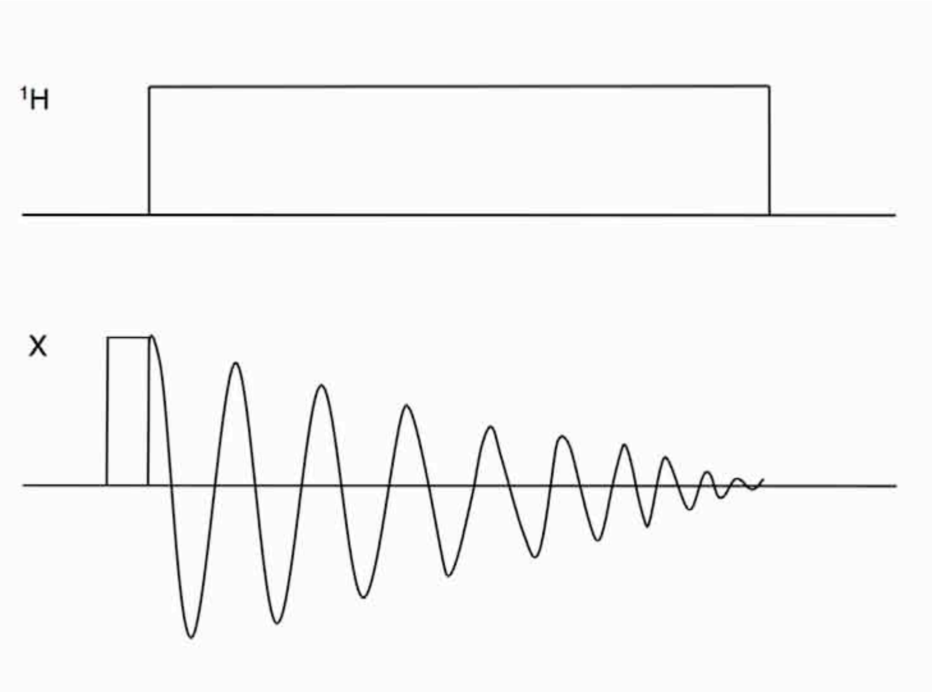

Figure 2.20: A schematic representation of a continuous wave (CW) pulse sequence used for ^1H decoupling of an X nucleus FID.

observed. Different schemes for decoupling exist, the simplest of which is continuous wave (CW) decoupling.[161] Consider two dipolar-coupled ^1H and ^{13}C spins where the ^{13}C spins are to be observed. The method consists of applying continuous irradiation of very high power, commonly 100-1000 watts, at the frequency of the proton resonance. The required pulse sequence for the ^{13}C nuclei is then applied and the ^{13}C FID is acquired whilst the ^1H is irradiated with high power rf pulses. This method of decoupling is relatively easy to implement and an example of the sequence used for CW decoupling is shown in Figure 2.20. It must be noted that this type of decoupling requires very high rf powers for effective decoupling. Alternatively, other decoupling pulse sequences may be used such as Two Pulse Phase Modulated (TPPM) which, in contrast to CW methods, incorporates phase modulation of the rf to achieve more efficient decoupling.[162]

As described previously, homonuclear dipolar couplings can only be removed when the MAS rate is greater than the homonuclear dipolar linewidth. Where this is not possible the effects of homonuclear dipolar couplings may be removed by homonuclear decoupling. Unlike heteronuclear decoupling, it is not possible to pulse and acquire simultaneously on two identical spins. Therefore, a 'windowed' approach is required in which pulses are applied to remove the dipolar interaction and points of the FID are collected in small windows between each of the pulses applied. This type of sequence is technically challenging to implement.

2.8 Quadrupolar Interactions

2.8.1 Introduction

The periodic table is dominated by quadrupolar nuclei, with approximately 75% of the NMR-active species possessing a spin quantum number greater than 1/2. Quadrupolar interactions are therefore a relatively common occurrence in NMR.

Quadrupolar nuclei possess a nuclear electric quadrupole moment, eQ, that interacts with the electric field gradient (EFG), generated at the nucleus by other atoms present in the sample.[163] This interaction, known as the quadrupolar interaction, is extremely strong and, in turn, produces an inhomogeneous broadening, commonly of the order of megahertz, in the solid-state NMR spectra of quadrupolar nuclei. The quadrupolar interaction is orientationally dependent and in its PAS it may be described by three principal components; V_{xx}, V_{yy} and V_{zz}. The magnitude of the EFG is given by eQ = V_{zz} and the shape of its cross-section can be represented by an asymmetry parameter, η_Q (Equation 2.45). The magnitude of the quadrupolar interaction is given, in Hz, by the quadrupolar coupling constant, C_Q,[163]

$$C_Q = \frac{eQV_{zz}}{h} = \frac{e^2qQ}{h} \qquad (2.44)$$

$$\eta_Q = \frac{V_{xx} - V_{yy}}{V_{zz}} \qquad 0 < \eta_Q < 1 \ . \qquad (2.45)$$

As stated previously, the total Hamiltonian, H, for a particular nucleus depends upon many contributions. The quadrupolar interaction is often very large but, in many cases, remains smaller than the more dominant Zeeman interaction. The Hamiltonian describing the quadrupolar interaction is given by[164]

$$H_Q = \frac{eQ}{2I(2I-1)\hbar} \mathbf{I} \cdot \mathbf{V} \cdot \mathbf{I} \tag{2.46}$$

$$H_Q = \frac{eQ}{2I(2I-1)\hbar} (I_x\, I_y\, I_z) \begin{pmatrix} V_{xx} & V_{xy} & V_{xz} \\ V_{yx} & V_{yy} & V_{yz} \\ V_{zx} & V_{zy} & V_{zz} \end{pmatrix} \begin{pmatrix} I_x \\ I_y \\ I_z \end{pmatrix} . \tag{2.47}$$

Hence, the total Hamiltonian for a quadrupolar nucleus, neglecting for the moment contributions from smaller interactions such as chemical shift anisotropy, dipolar and scalar couplings, may be expressed as the sum of the individual Hamiltonians for the Zeeman and quadrupolar interactions, given by

$$H = H_Z + H_Q \ . \tag{2.48}$$

In the PAS the quadrupolar tensor, **V**, is diagonal and the Hamiltonian is given by[164]

$$H_Q = \frac{3e^2qQ}{4I(2I-1)\hbar} \left[I_z^2 - \frac{1}{3} I(I+1) + \frac{\eta_Q}{3} (I_x^2 - I_y^2) \right] . \tag{2.49}$$

2.8.2 First-Order Quadrupolar Interactions

The effect of the quadrupolar interaction may be described as a perturbation of the Zeeman energy levels and can therefore be described using perturbation theory.[165] The quadrupolar interaction perturbs all energy levels and, to a first-order approximation, splits the original degenerate transitions at ω_0 into 2I transitions, equally spaced by $2\omega_Q$. In Figure 2.21 the Zeeman energy levels for spin I = 1 and I = 3/2 nuclei are shown, displaying two and three degenerate transitions at ω_0, respectively.

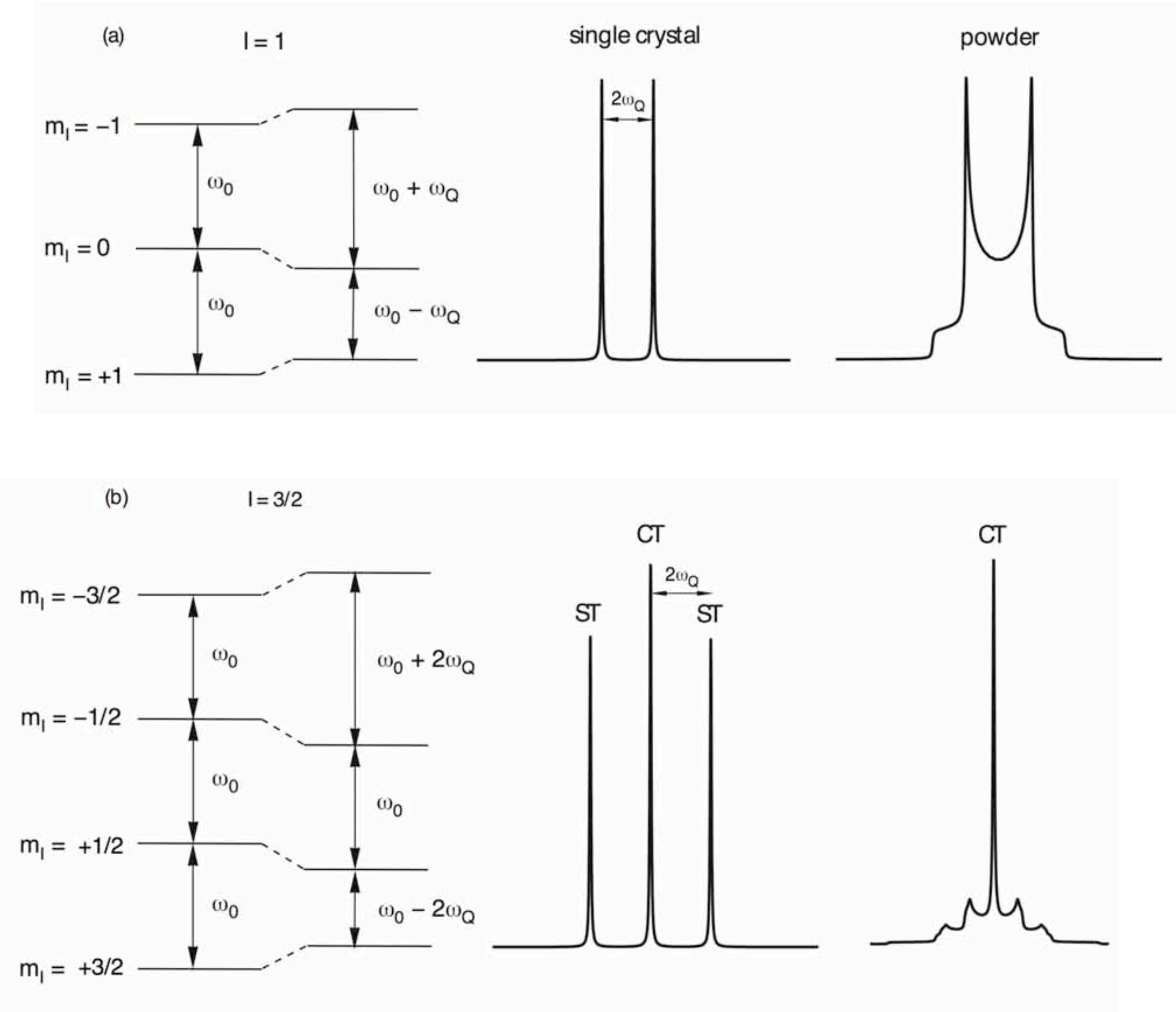

Figure 2.21: First-order perturbation of the Zeeman energy levels by the quadrupolar interaction for systems with (a) I = 1 and (b) I = 3/2. Also shown are resulting spectra for each spin system with 2I non-degenerate transitions separated by $2\omega_Q$, and corresponding spectra for a powder distribution of crystallites. In each case the central transition and satellite transitions are marked by CT and ST, respectively.

Also shown is the effect of the quadrupolar interaction, to a first-order approximation, on the energy levels. The quadrupolar splitting parameter, ω_Q, is given by

$$\omega_Q = \frac{(\omega_Q^{PAS})}{2}(3\cos^2\theta - 1 + \eta_Q(\sin^2\theta\cos\phi)) \tag{2.50}$$

with

$$\omega_Q^{PAS} = \frac{3\pi C_Q}{2I(2I-1)} \quad , \tag{2.51}$$

given in rad s^{-1}, where the angles θ and ϕ define the orientation of the PAS of the EFG with respect to the external magnetic field.

For I = 3/2 nuclei, all energy levels are perturbed by the first-order quadrupolar interaction. However, for single-quantum transitions only the frequency of the central transition (m_I = +1/2 ↔ −1/2) remains unchanged at ω_0. The frequency of the outer transitions, termed satellite transitions with m_I = ±1/2 ↔ ±3/2, is now dependent upon the quadrupolar splitting parameter, ω_Q. This highlights a vital distinction between quadrupolar nuclei with integer and half-integer spins. For nuclei with half-integer spin quantum numbers the central transition is not affected to first-order by the quadrupolar interaction, producing a sharp peak in the centre of the spectrum. No such transition exists in the case of integer spins, and hence all transitions exhibit a perturbation by the quadrupolar interaction. These differences are highlighted in Figure 2.21.

Polycrystalline samples are composed of millions of tiny crystallites, each with a different orientation with respect to B_0, and hence in a similar manner to the CSA they commonly exhibit broad 'powder pattern' lineshapes, as a direct result of the orientational dependence of ω_Q. The width of each lineshape is directly proportional to C_Q therefore a measure of the linewidth can give a good indication as to the magnitude of the quadrupolar interaction. Examples of powdered lineshapes for spin I = 1 nuclei have been simulated with varying η_Q values and are shown in Figure 2.22.

2.8.3 Removal of First-Order Effects

For static samples substantial inhomogeneous broadening is exhibited for quadrupolar nuclei owing to the quadrupolar interaction. Therefore, a method for removing this interaction and obtaining high-resolution spectra is highly desirable. Examination of the first-order

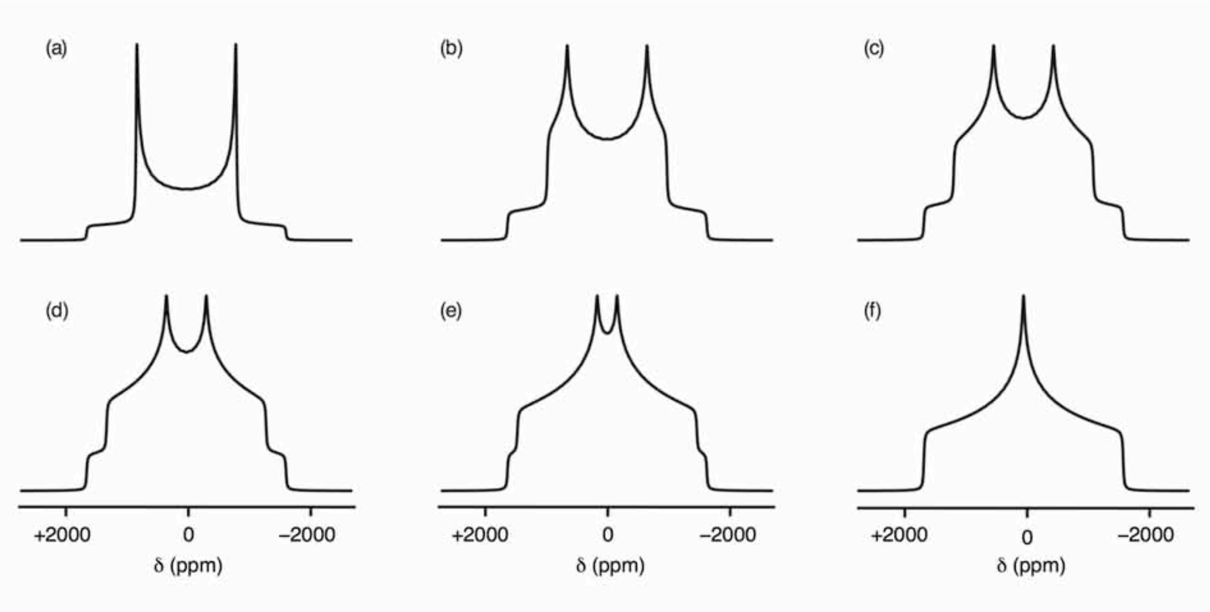

Figure 2.22: Powdered spin I = 1 lineshapes simulated under static conditions with C_Q = 2 MHz and η_Q = 0, 0.2, 0.4, 0.6, 0.8 and 1 in (a-f) respectively.

quadrupolar interaction (Equation 2.50) reveals an angular dependence similar to that previously identified for the chemical shift anisotropy and dipolar couplings, $3\cos^2\theta - 1$. Therefore, under MAS the quadrupolar interaction should be removed to first order. As previously described in section 2.6 MAS is only effective when the MAS rate is similar or greater than the anisotropy of the interaction attempting to be removed. Quadrupolar interactions are commonly many megahertz in magnitude and therefore fast MAS rates would be required to fully remove the interaction. For integer spins, if the MAS rate is too slow the spectrum will be broken up into a series of spinning sidebands. For half-integer spins under MAS only the satellite transitions are affected, the central transition is not broadened to first-order.

2.8.4 Second-Order Quadrupolar Interactions

When the quadrupolar interaction is relatively small a first-order approximation is sufficient to describe the effect upon the spectrum. However, in reality, for many solids this interaction is very large and a first-order perturbation approximation is no longer sufficient. When this

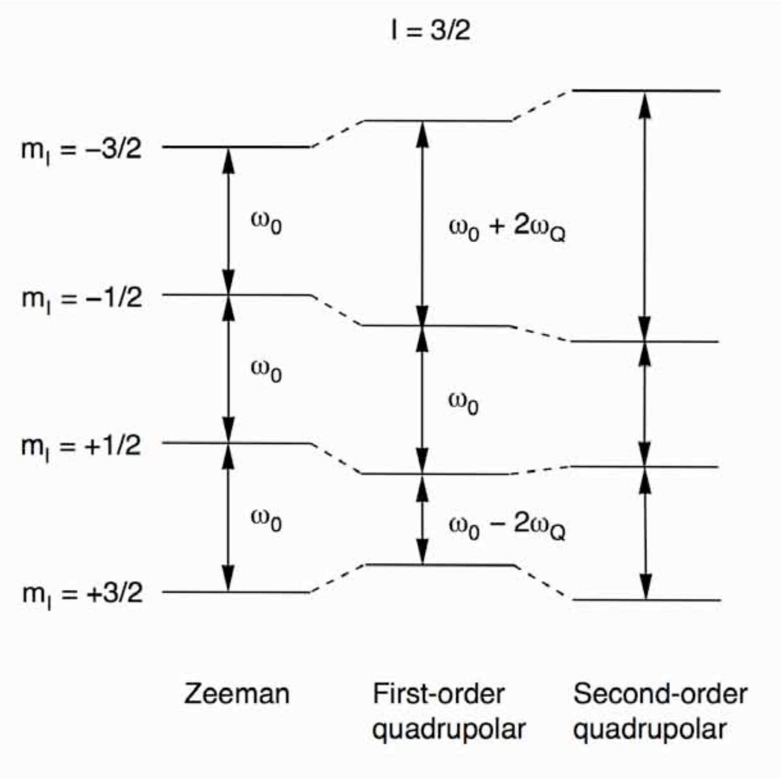

Figure 2.23: Perturbation of the Zeeman energy levels arising from the quadrupolar interaction to a first- and second-order approximation for a I = 3/2 system. Although not broadened by the first-order quaderupolar interaction, the central-transition is broadened by the second-order quadrupolar interaction.

is the case second-order terms are required to describe the perturbation of the Zeeman energy levels by the quadrupolar interaction. The four energy levels for a spin I = 3/2 nucleus are shown in Figure 2.23 under the effect of the Zeeman interaction, the first-order quadrupolar interaction and the second-order quadrupolar interaction. Both the central (CT) and satellite transitions (ST) are affected by the second-order quadrupolar interaction. The second-order perturbation to a transition frequency $m_I \leftrightarrow -m_I$ as defined, under MAS with $\eta_Q = 0$, is given by

$$E^2_{|m_I\rangle} - E^2_{|-m_I\rangle} = \frac{(\omega_Q^{PAS})^2}{\omega_0}[A^0(I,m_I) + A^2(I,m_I)d^2_{00}(\theta)d^2_{00}(\chi)$$

$$+A^4(I,m_I)d^4_{00}(\theta)d^4_{00}(\chi)] \qquad (2.52)$$

where $A^n(I,m_I)$ are spin and energy level dependent coefficients, θ is the angle between the rotor axis and the applied field (i.e., 54.736°) and

$d^1_{mm}(\alpha)$ are Wigner reduced rotation matrix elements.[166] It can be seen that the second-order interaction is composed of three distinct terms: an isotropic shift (proportional to $A^0(I, m_I)$), a second-rank anisotropic term (proportional to $A^2(I, m_I)d^2_{00}(\theta)d^2_{00}(\chi)$) and a fourth-rank anisotropic term (proportional to $A^4(I, m_I)d^4_{00}(\theta)d^4_{00}(\chi)$). The spin-dependent coefficients $A^n(I, m_I)$ are listed in Table 2.2 for half-integer spins.

For a spin I = 3/2 nucleus (again with $\eta_Q = 0$) Equation 2.52 may be expressed more simply as

$$E^2_{|1/2\rangle} - E^2_{|-1/2\rangle} = \frac{(\omega_Q^{PAS})^2}{\omega_0}\left[-\frac{2}{5} - \frac{8}{7}d^2_{00}(\theta)d^2_{00}(\chi) + \frac{54}{35}d^4_{00}(\theta)d^4_{00}(\chi)\right] \quad (2.53)$$

where

$$d^2_{00}(\theta) = \frac{1}{2}(3\cos^2\theta - 1) \quad (2.54)$$

$$d^4_{00}(\theta) = \frac{1}{8}(35\cos^4\theta - 30\cos^2\theta + 3) \ . \quad (2.55)$$

The second-rank element, $d^2_{00}(\theta)$, has the same orientational dependence as the chemical shift anisotropy, dipolar and scalar couplings, and hence this broadening may be removed under MAS. The fourth-rank element, however, possesses a much more complex orientational dependence. This term is averaged to zero only when θ = 30.56° or 70.12°. Hence, it is not feasible for conventional MAS to remove completely the anisotropic second-order quadrupolar broadening.

As shown previously, the central transition of a half-integer quadrupolar nucleus was not broadened, to a first-order approximation, by the quadrupolar interaction. This transition does, however, experience a second-order broadening. To illustrate the effect of this broadening on NMR spectra of half-integer nuclei, second-order broadened central transition powder pattern lineshapes have been simulated under MAS for a spin I = 3/2 nucleus with varying η_Q values, as shown in Figure 2.24. The central transition, previously unaffected to first order, now exhibits a complex 'powder pattern' lineshape that is shifted from the centre of the spectrum. The magnitude of the second-order quadrupolar interaction is

Table 2.2: Coefficients for zero-, second- and fourth-rank terms in Equation 2.50 for half-integer spin nuclei.

I	m_I	$A^0(I,m_I)$	$A^2(I,m_I)$	$A^4(I,m_I)$
I = 3/2	1/2	−2/5	−8/7	54/35
	3/2	6/5	0	−6/5
I = 5/2	1/2	−16/15	−64/21	144/35
	3/2	−4/5	−40/7	228/35
	5/2	20/3	40/21	−60/7
I = 7/2	1/2	−30/15	−120/21	270/35
	3/2	−54/15	−96/7	606/35
	5/2	30/15	−240/21	330/35
	7/2	294/15	168/21	−966/35
I = 9/2	1/2	−48/15	−192/21	432/35
	3/2	−108/15	−168/7	1092/35
	5/2	−60/15	−600/21	1140/35
	7/2	168/15	−336/21	168/35
	9/2	648/15	432/21	−2332/35

proportional to $(\omega_Q^{PAS})^2/\omega_0$, and so it is considerably smaller than the first-order quadrupolar interaction, proportional to ω_Q^{PAS}. The position of the NMR resonance for a quadrupolar nucleus is the sum of the isotropic chemical shift, δ_{iso}, and the isotropic quadrupolar shift, δ_Q.

2.8.5 Removal of Second-Order Quadrupolar Broadening

Second-order quadrupolar broadening of NMR spectra often hinders the extraction of important information regarding the number of crystallographically distinct sites or the relative populations of different sites within a sample as it cannot be removed by MAS. Hence, a technique capable of removing such broadenings and achieving high-resolution spectra for quadrupolar nuclei exhibiting such effects is required. For example, two-dimensional techniques such as double

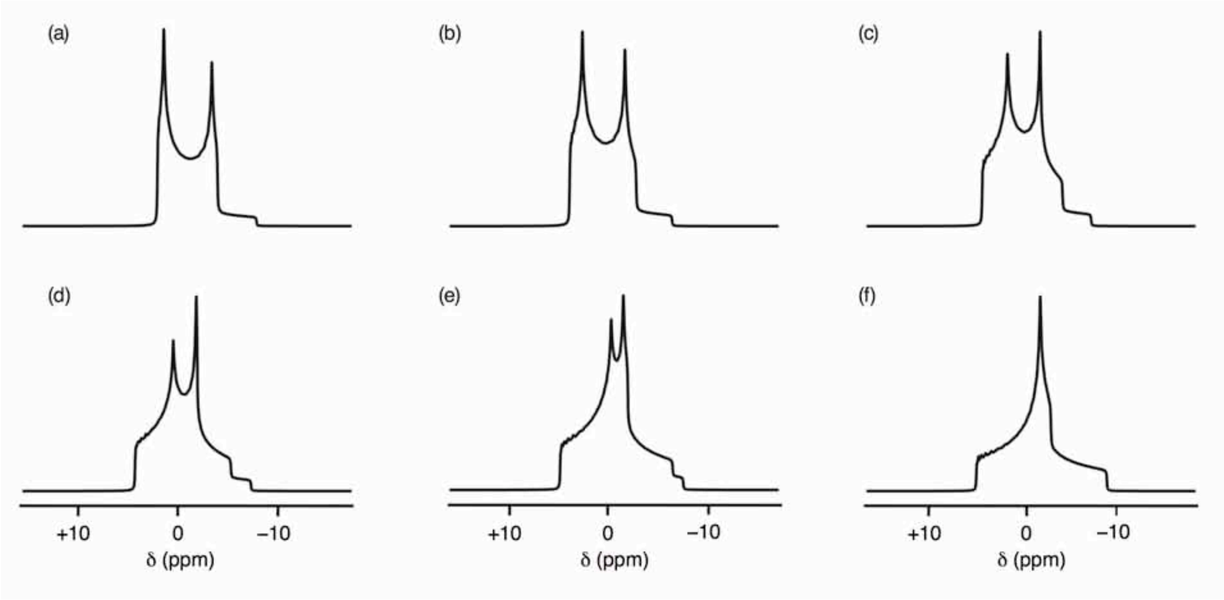

Figure 2.24: Second-order broadened central-transition MAS powder lineshapes for a I = 3/2 system simulated with C_Q = 2 MHz, $\omega_0/2\pi$ = 158.75 MHz and asymmetry, η_Q, of (a) 0, (b) 0.2, (c) 0.4, (d) 0.6, (e) 0.8 and (f) 1.

rotation[167,168] (DOR), dynamic-angle spinning[169,170] (DAS) or multiple-quantum (MQ) MAS may be utilised.[171]

2.8.6 Double Rotation (DOR)

One possible method for obtaining high-resolution NMR spectra for quadrupolar nuclei is the double rotation (DOR) technique.[167,168] In Equation 2.53 it was shown that the second- and fourth-rank anisotropic quadrupolar broadenings possessed different angular dependencies; hence, to remove both interactions simultaneously, rotation of the sample would need to occur around two different angles. DOR achieves high-resolution spectra by spinning the sample, by means of a double rotor, simultaneously at two different angles, one being the magic angle, θ, which averages the second-rank anisotropic broadening contribution, whilst the other angle (θ_R = 30.56° or 70.12°) averages the fourth-rank terms to zero. A schematic representation of the apparatus used in DOR is shown in Figure 2.25. Furthermore, the use of the magic angle removes any additional CSA or dipolar interactions from the spectrum. However, it must be noted that DOR, despite producing high-resolution spectra, is

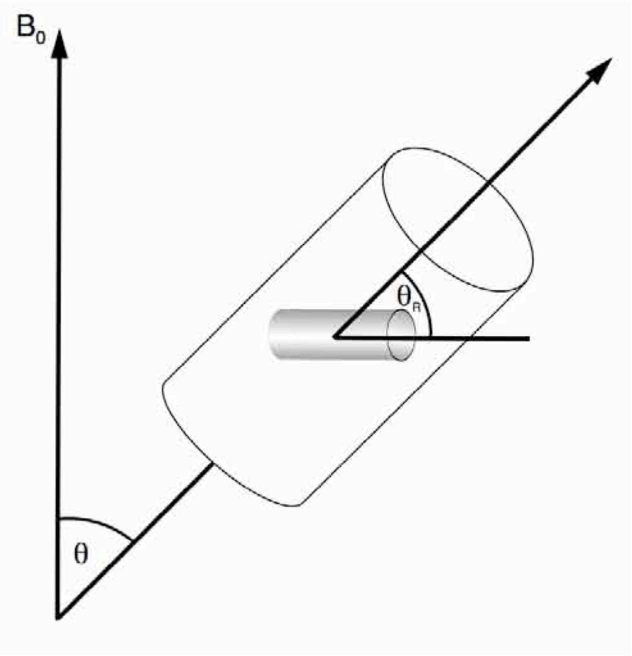

Figure 2.25: Schematic representation of the DOR experiment. Shown are two rotors, one spinning inside the other. The outer rotor spins about an axis inclined at 54.736° to the applied magnetic field, B_0, whilst the inner rotor spins about an axis inclined at 30.65° (or 70.12°) relative to the outer rotor.

an extremely specialist technique and its practical application is limited owing to technical restrictions on the spinning speed of the outer rotor. The mechanical complexity of the technique leads to the requirement of expensive hardware different to that utilised for conventional MAS.

2.9 Multiple-Quantum Magic-Angle Spinning (MQMAS)

2.9.1 Introduction

Owing to the technical demands and complex practical implementation of methods such as DOR, alternative methods for the acquisition of high-resolution spectra have been developed in recent years. In 1995, Frydman and Harwood[171] suggested a method for removing second-order quadrupolar broadening which utilises the hardware conventionally used for MAS. The experiment, now termed multiple-quantum magic-angle spinning (MQMAS), is a two-dimensional technique which correlates multiple- and single-quantum coherences under MAS. The coherences exploited in MQMAS are the symmetric m_I

↔ $-m_I$ coherences, i.e., triple-quantum (+3/2 ↔ −3/2), five-quantum (+5/2 ↔ −5/2) etc. Note that these coherences cannot be directly observed. Owing to the ease of its implementation the development of MQMAS has resulted in renewed interest in high-resolution NMR in a wide range of quadrupolar nuclei.

2.9.2 The MQMAS Experiment

The original MQMAS experiment used two pulses to excite multiple-quantum coherences.[171] However, it has subsequently been shown that single-pulse excitation[172,173] is a more efficient method to excite such coherences for nuclei with half-integer spin, as shown in Figure 2.26.[174-176] In MQMAS experiments multiple-quantum coherences are first excited using a high power rf pulse, and these then evolve during a time period t_1. The pulse utilised needs to be sufficiently high in power to efficiently excite multiple-quantum coherences. To select the desired coherence changes and ensure that no unwanted coherences are carried forward for the remainder of the pulse sequence a process known as phase cycling is required. Additional details regarding phase cycling can be found in Appendix I. The experiment is conducted under MAS and therefore it may be assumed that the second-rank second-order anisotropic broadening is averaged to zero throughout the experiment. Hence, the only anisotropy that arises during t_1 is due to the fourth-rank term. At the end of t_1 a second rf pulse is applied which converts the remaining multiple-quantum coherence to observable single-quantum coherences. A two-dimensional time domain dataset is obtained, displaying the evolution of single- and multiple-quantum coherences in the t_2 and t_1 dimensions respectively.

The key feature of the MQMAS technique is its ability to refocus fourth-rank anisotropic broadenings whilst retaining isotropic shifts. The second-order perturbation to the frequency of the central transition of a spin I = 3/2 nucleus under MAS conditions was shown earlier in Equation

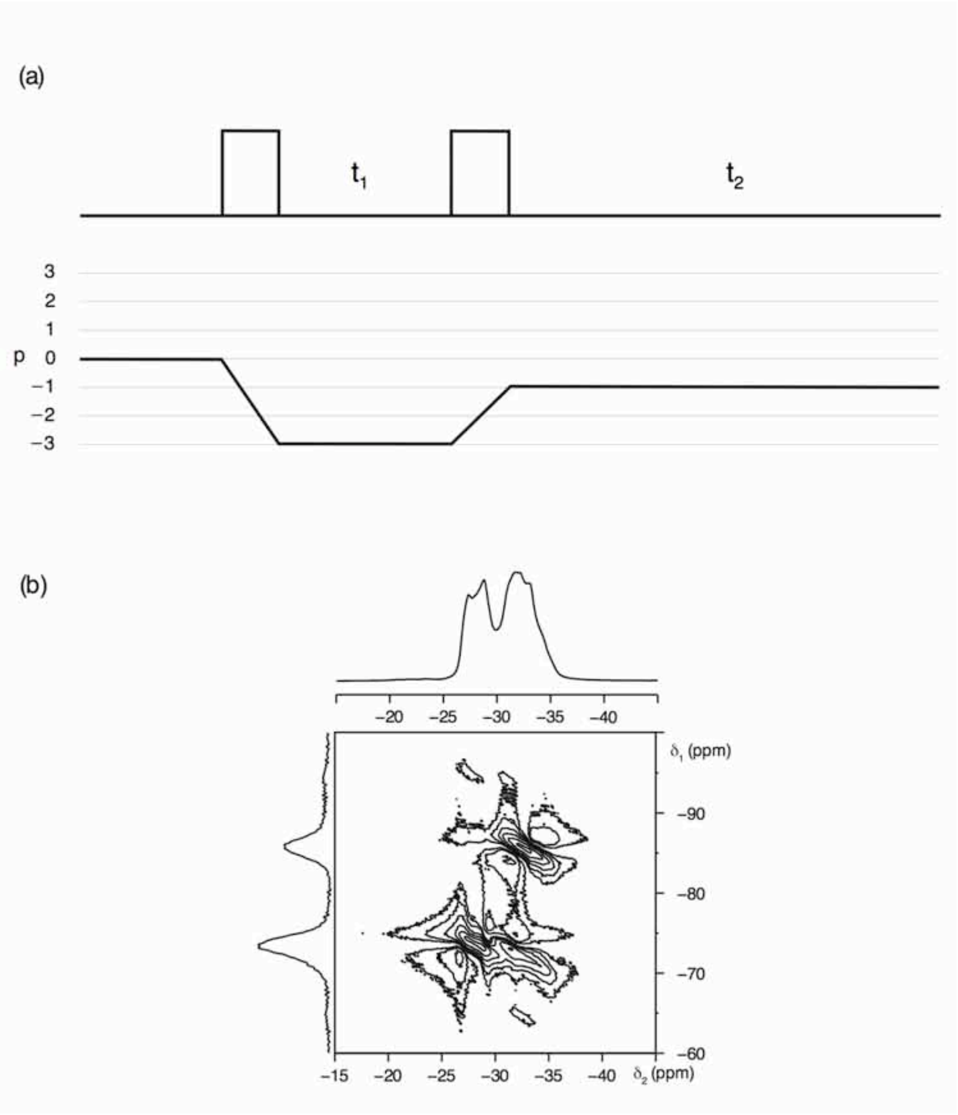

Figure 2.26: (a) Pulse sequence and coherence transfer pathway diagram for the two-pulse MQMAS NMR experiment adapted from that of Frydman and Harwood.[171] (b) Conventional ^{97}Rb MAS (14.1 T) NMR spectrum and triple-quantum MAS NMR spectrum of RbNO$_3$, recorded using the pulse sequence shown in (a). The spectrum is the result of averaging 96 transients with a recycle interval of 0.25 s for each of the 512 increments of 60.0 μs. The MAS rate was 12.5 kHz.

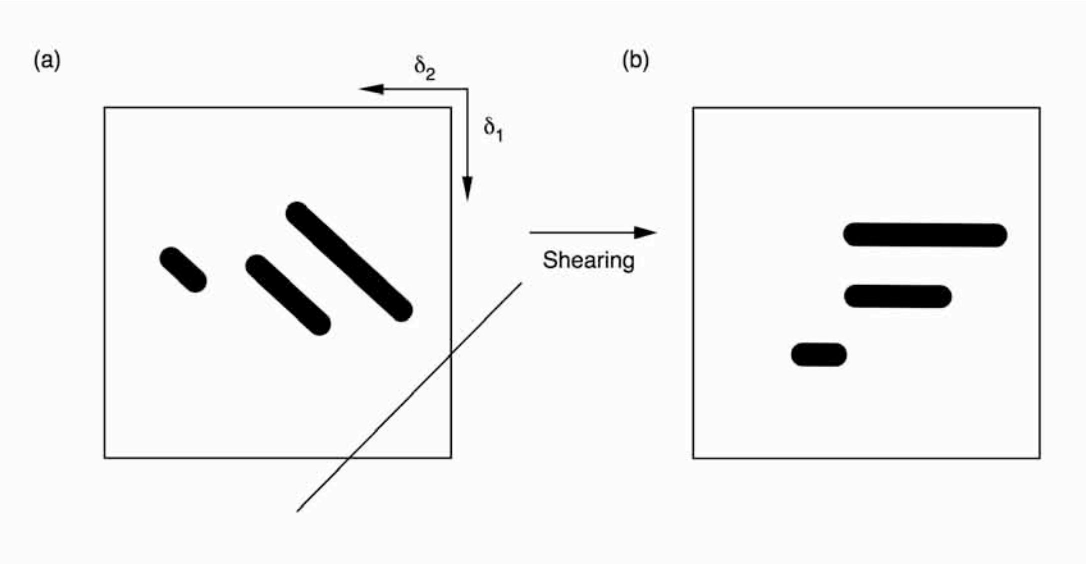

Figure 2.27: Schematic representation of a spectrum resulting from an MQMAS experiment. Shown in (a) are a series of ridges aligned along a gradient equal to the MQMAS ratio, R. To obtain an isotropic projection a projection orthogonal to the ridges is obtained, as shown in (a). This isotropic projection is free from quadrupolar broadening but retains the isotropic shifts. Shown in (b) is the spectrum post shearing, exhibiting a series of ridges parallel to δ_2. An isotropic spectrum is then obtained from a projection onto δ_1.

2.53. A similar expression may be obtained for the frequency of the triple-quantum transition for a I = 3/2 nucleus under MAS, given for $\eta_Q = 0$ by

$$E^2_{|3/2\rangle} - E^2_{|-3/2\rangle} = \frac{6}{5} - \frac{6}{5} d^4_{00}(\theta) d^4_{00}(\chi) \quad . \tag{2.56}$$

It can be seen from equations 2.53 and 2.56 that the ratio of the coefficients in the single- and triple-quantum expressions is different for the isotropic and anisotropic fourth-rank terms, i.e., $A^0(I,3/2)/A^0(I,1/2)$ and $A^4(I,3/2)/A^4(I,1/2)$. Using this property it is possible to refocus the anisotropic terms and retain solely the isotropic shifts to produce a high-resolution spectrum. It must be noted that the ratio of the coefficients of the anisotropic fourth-rank terms under single- and multiple-quantum coherences, $A^4(I,m_I)/A^4(I,1/2)$, is different for each spin system and coherence order. It is this value, termed the MQMAS ratio, R, that determines the point during t_2 at which the anisotropic broadening will be refocused. In addition, this value also determines the gradient along